YOKOHAMA NATIONAL UNIVERSITY

Doctoral Dissertation

Investigation of effects of wind barriers on the aerodynamic performance of the box girders

遮風壁が箱桁の空力安定性に及ぼす影響調査

Author:

Anousit VILAIVONG

Supervisors and Advisors:

Prof. Hiroshi KATSUCHI

Assoc. Prof. Hiroshi TAMURA

Assist. Prof. Jiaqi WANG

Assist. Prof. Kensho HIRAO

Graduate School of Urban Innovation
September 2024

Abstract

This research aims to experimentally investigate the effects of various wind barrier parameters, including hole schemes, porosity ratios, heights, installation method, and vertical Vortex-Induced Vibration (VIV) countermeasures, on the aerodynamic performance and wind speed reduction for vehicle driving enhancement of a bridge featuring a bluff box girder with a side ratio *B/D* of 3.44 (thick girder) and 4.98 (thin girder), where *B* is the width and *D* is the depth of the girder. The investigation was conducted through wind tunnel experiments, including an aerodynamic force coefficient test, two-degree-of-freedom free vibration test, and wind velocity measurement.

The results show that mean and maximum wind speeds are relatively higher for the thin girder compared to the thick girder, indicating that girders with larger side ratios are more susceptible to vehicle driving safety concerns. This finding suggests that strategic placement of wind barriers only at the mid-span of varying girder depth bridges can help limit the cost and time for wind barrier installation while minimizing their effects on the aerodynamic performance of bridges. In the presence of wind barriers, the wind speeds over the driving areas of both girders, particularly at the windward lanes, are significantly reduced, improving the stability of vehicles traveling on the bridge. Additionally, wind barriers transform the flow pattern from reattached to detached in the thin girder, while maintaining the detached flow pattern in the thick girder.

Although wind barriers effectively reduce wind speeds, they adversely affect the aerodynamic performance of the bridge by increasing the drag coefficient and the amplitude of vertical VIV, decreasing the critical wind velocity for torsional flutter, albeit with the benefit of reducing the torsional VIV amplitude. The proposed countermeasures successfully reduce the vertical VIV amplitude in the thick girder with increased onset wind velocity that substantially improves traffic regulation during strong crosswinds. Conversely, similar countermeasures fail to reduce the VIV amplitude in the thin girder.

Among the various wind barrier parameters, the porosity ratio is crucial due to its dual role in minimizing bridge instability and enhancing vehicle driving safety on both girders. Higher porosity ratios reduced the vertical VIV amplitude and increased the critical wind velocity for torsional flutter, although at the cost of diminished shielding efficiency compared to lower porosity ratios. Conversely, the orientation of the hole schemes has a negligible effect on the aerodynamic performance of the thick girder. Furthermore, the partial installation of wind barriers above the handrail proves practical, especially for bridges with limited installation space.

Given the dependency of the bridge's aerodynamic performance on the configuration of the bridge girders and wind barriers, and the challenges encountered in stabilizing vertical VIV in the thin girder with a side ratio of 4.98, this research further elucidates the mechanism of vertical VIV of a bluff box girder with a side ratio of 5.00 and its attachment with fairing serving as a stabilizing countermeasure. The study also proposes a new triangular bar member wind barrier for stabilizing such vibrations. Wind tunnel tests, including a one-degree-of-freedom free vibration test, pressure distribution measurement, and flow visualization using Particle Image Velocimetry (PIV) analysis, were conducted.

The results indicate that reattached flow on the top and bottom surfaces of the girder, characterized by a recirculation zone, results in mean pressure recovery and large pressure fluctuation at the trailing-edge zone might be responsible for vertical VIV. The fairing attachment alters the flow by shifting the reattachment at the trailing edge zone of the primary recirculation to the leading edge of the girder possibly contributing to vertical VIV.

In the presence of wind barriers, the newly proposed triangular bar member wind barrier effectively reduces the vertical VIV amplitude compared to other wind barriers. This reduction is possibly attributed to the aerodynamic triangular shape of the bar members, which accelerates the flow, leading to a homogeneous flow that eliminates the recirculation zone on the top side of the girder. This elimination results in the most rapid mean pressure recovery and the smallest pressure fluctuation on the top side. Besides, this wind barrier shows a minimal effect on promoting shear layer separation and intensifying flow recirculation on the bottom side of the girder compared to other wind barriers, which helps limit pressure reduction and pressure fluctuation amplification. Importantly, this triangular wind barrier significantly reduces the spanwise correlation coefficient of sectional fluctuating lift force lower than other wind barrier cases implying a more scattered and less synchronized flow structure along the spanwise direction of the girder

For rectangular bar member wind barriers, although they modify the flow on the top side of the girder to detach, increasing mean pressure and reducing pressure fluctuation on this side, they strongly promote the shear layer promotion and substantially intensify the recirculation zone on the bottom side of the girder, resulting in increased mean pressure reduction and amplified pressure fluctuation which might potentially contribute to amplified VIV amplitude.

Additionally, flow controlled by fairing on the upstream side of the girder accelerates the flow on the top side of the girder for some wind barriers leading flow to homogenous flow and it also minimizes the effect of wind barriers in the separation promotion and recirculation amplification on the bottom side of the girder. These suggest the primary reasons for better VIV stabilization compared to no fairing scenario.

In conclusion, the aerodynamic performance of the bridge is significantly affected by the configuration of the bridge and wind barriers. The findings of this research not only demonstrate the effectiveness of various wind barrier parameters in reducing wind speed for vehicle driving safety but also provide insights into the stabilization and destabilization mechanisms of vertical VIV in bluff girders. These findings offer valuable information for the design of wind barriers, benefiting both bridge stability and vehicle driving safety.

Acknowledgments

I am profoundly grateful to many people whose support and guidance have been instrumental in the successful completion of my doctoral thesis. Writing this thesis has been one of the most significant academic challenges I have faced, not least because it involved adjusting to life and academic culture in Japan. The support I received throughout this period was vital not only to my academic success but also to my personal growth and well-being.

Firstly, I extend my heartfelt thanks to my supervisor, Professor Hiroshi Katsuchi. His kind guidance and support were invaluable, both academically and in helping me navigate my new life in Japan. His patience and dedication profoundly influenced my personal and professional growth, and I am incredibly grateful for his mentorship.

I also appreciate the support of Associate Professor Hiroshi Tamura and Assistant Professor Kensho Hirao. Their engaging questions and helpful feedback encouraged me to think more critically and helped improve my research significantly. Their insights were essential in shaping my thesis.

I am also indebted to Assistant Professor Jiaqi Wang, who was consistently supportive throughout my research process. His involvement in various experiments and his insightful suggestions greatly enhanced the quality of my work. His commitment to excellence has been truly inspiring.

I am also grateful to the Japanese People, the Government of Japan, and the Japan International Cooperation Agency (JICA) for their generous financial support through scholarships, including the MEXT scholarship, and their hospitality. Their support made my studies and stay in Japan comfortable and rewarding.

Lastly, I must thank my family for their endless support and encouragement. Their love and belief in me were my motivation throughout this journey, and their sacrifices did not go unnoticed. They were always there for me, despite the distance, reminding me of my goals and aspirations.

I would also like to extend my sincere thanks to my colleagues and friends. Their camaraderie and teamwork have made the long hours in the lab much more enjoyable. Your support and friendship have been invaluable throughout this journey.

To everyone who supported me in any way during this journey, I am sincerely grateful. Thank you for all the guidance and encouragement.

Table of Contents

CHAPTER 1 Introduction 1
1.1 Background 1
1.2 Objectives 3
1.3 Structure 3
References 4
CHAPTER 2 Theoretical background and literature review 5
2.1 Wind-induced accidents and their measures 5
2.2 Basic principles of bluff body aerodynamics 7
2.2.1 Flow separation and vortex shedding 7
2.2.2 Pressure distribution and aerodynamic force coefficients on a bluff body 8
2.3 Fundamental aerodynamic responses of long-span bridges 9
2.3.1 Vortex-induced vibrations 9
2.3.2 Galloping 11
2.3.3 Torsional flutter 12
2.4 Wind tunnel test 13
2.4.1 Introduction to wind tunnels 13
2.4.2 Basic scaling laws and similarity requirements 14
2.4.3 Principles of Particle Image Velocimetry (PIV) 15
2.5 Effects of side ratios of the bluff body on wind flow and aeroelastic instabilities 17
2.6 Past research on the effects of wind barriers on vehicle driving stability and aerodynamic performance of bridges 18
References 21
CHAPTER 3 Methodology 24
3.1 Introduction 24
3.2 Outline of wind tunnel 24
3.3 Aerodynamic force coefficient measurement 25
3.4 Free vibration tests 26
3.5 Wind velocity measurement 28
3.6 Pressure measurement on the stationary sectional model 29
3.7 Flow visualization 31
CHAPTER 4 Effects of wind barriers on the aerodynamic performance and wind flow field of bluff box girders with different side ratios 32
4.1 Introduction 32

4.2 Sectional and wind barrier models 32
4.2.1 Sectional models 32
4.2.2 Wind barrier models 33
4.3 Aerodynamic force coefficients of the thick girder 35
4.3.1 Effects of hole schemes and porosities 36
4.3.2 Effects of installation method 37
4.3.3 Effects of countermeasures 38
4.4 Aerodynamic responses of bluff box girders with different side ratios 40
4.4.1 Effects of hole schemes 41
4.4.2 Effects of porosities 42
4.4.3 Effects of installation methods 44
4.4.4 Countermeasures to stabilize VIV 46
4.5 Wind flow field above the bluff box girders with different side ratios 51
4.5.1 Flow patterns above the bluff box girders and their alteration by wind barriers 51
4.5.2 Mean turbulence intensity above the bluff box girders and its alteration by wind barriers 54
4.5.3 Efficacy of wind barriers in wind speed reduction 58
4.6 Concluding remarks 61
References 62
CHAPTER 5 Mechanism of vertical vortex-induced vibration of a bluff box girder 64
5.1 Introduction 64
5.2 Sectional and wind barrier models 65
5.2.1 Sectional models 65
5.2.2 Wind barrier models 65
5.3 Vertical aerodynamic responses of the girder 67
5.3.1 Effect of porosity ratios and heights 68
5.3.2 Effect of countermeasures 68
5.4 Interplay between pressure distribution and mean wind flow field corresponding to VIV amplitude 70
5.4.1 Interplay between pressure distribution and mean wind flow field of the girder without wind barriers 71
5.4.2 Interplay between pressure distribution and mean wind flow field of the girder with wind barriers 72
5.5 Spanwise correlation coefficient of sectional fluctuating lift force 77
5.6 Effect of fairing attachment 78
5.6.1 Effect of fairing attachment without wind barriers 78

5.6.2 Effect of fairing attachment with wind barriers....79
5.7 Concluding remarks....81
CHAPTER 6 Conclusions....84
6.1 Conclusions....84
6.2 Future topics87 Appendix 1 Flow patterns above the bluff box girders and their alteration by wind barriers....88
Appendix 2 Vertical aerodynamic response of the girder (*B/D* = 5.00) with fairing attachment and wind barriers....90
Appendix 3 Pressure distribution of the girder (*B/D* = 5.00) with fairing attachment and wind barriers....91
Appendix 4 Wind flow structure around the girder (*B/D* = 5.00) via Proper Orthogonal Decomposition (POD) analysis....92
A4.1 Bare deck case (BD)....92
A4.2 25-H wind barrier (Top side)....93
A4.3 50-H-3.0m wind barrier (Top side)....95
A4.4 50-T wind barrier (Top side)....96
A4.5 50-H-2.5m wind barrier (Top side)....97
A4.6 50-H-DS wind barrier (Top side)....99
A4.7 50-H+F wind barrier (Top side)....100
A4.8 25-H wind barrier (Bottom side)....102
A4.9 50-H-3.0m wind barrier (Bottom side)....103
A4.10 50-T wind barrier (Bottom side)....105
A4.11 50-H-2.5m wind barrier (Bottom side)....106
A4.12 50-H-DS wind barrier (Bottom side)....108
A4.13 50-H+F wind barrier (Bottom side)....109

List of Figures

CHAPTER 1 Introduction 1

Figure 1.1 Wind-induced traffic accidents (Zhang et al., 2020) 2

Figure 1.2 Wind barrier installed on the handrail with on-site wind speed measurement (Yang et al., 2022) 2

CHAPTER 2 Theoretical background and literature review 5

Figure 2.1 Flow separation and vortex shedding (Simiu and Yeo, 2019) 7

Figure 2.2 Flow and vortex shedding around a rectangular cylinder (Re = 200) (Simiu and Yeo, 2019) 7

Figure 2.3 Lift and drag on an arbitrary bluff body (Simiu and Yeo, 2019) 8

Figure 2.4 Frequency of vortex shedding as a function of wind velocity (Simiu and Yeo, 2019) 10

Figure 2.5 Strouhal number *St* for rectangular cylinders as a function of side ratio *B/D* and for bridge decks (Simiu and Miyata, 2006) 17

Figure 2.8 Vertical aerodynamic characteristics versus side ratio of one and two box girders (Saito and Sakata, 1999) 18

CHAPTER 3 Methodology 24

Figure 3.1 Closed-circuit wind tunnel 24

Figure 3.2 Open-circuit wind tunnel 25

Figure 3.3 Details of aerodynamic force coefficient measurement 26

Figure 3.4 A sectional model in a wind tunnel for aerodynamic force coefficient measurement 26

Figure 3.5 A sectional model with wind barriers for free vibration test 27

Figure 3.6 Support system for free vibration test 27

Figure 3.7 A sectional model with “X” hotwire anemometer 28

Figure 3.8 Wind measurement points (unit: mm; scale: 1/100) 39

Figure 3.9 Sectional models with pressure tap points (unit: mm; scale: 1/100) 30

Figure 3.10 Pressure measurement sections (unit: mm; scale: 1/100) 30

Figure 3.11 Pressure measurement in open-circuit wind tunnel 30

Figure 3.12 Test setup of flow visualization 31

CHAPTER 4 Effects of wind barriers on the aerodynamic performance and wind flow field of bluff box girders with different side ratios 32

Figure 4.1 Sectional models (unit: mm; scale: 1/100) 33

Figure 4.2 Details of wind barrier models (unit: mm; scale: 1/100) 35

Figure 4.3 Aerodynamic force coefficients and galloping criterion of thick girder with different hole scheme wind barriers.....37
Figure 4.4 Aerodynamic force coefficients and galloping criterion of thick girder with installation method of wind barriers.....38
Figure 4.5 Aerodynamic force coefficients and galloping criterion of thick girder with countermeasures.....39
Figure 4.6 Aerodynamic responses of thick girder (BD of 3.44) with different hole scheme wind barriers (α = 0°).....41
Figure 4.7 Aerodynamic responses of thick girder (BD of 3.44) with different hole scheme wind barriers (α = +3°).....41
Figure 4.8 Vertical aerodynamic response of thick girder (BD of 3.44) with different porosity wind barriers.....43
Figure 4.9 Vertical aerodynamic response of thin girder (BD of 4.98) with different porosity wind barriers.....43
Figure 4.10 Torsional aerodynamic response of thick girder (BD of 3.44) with different porosity wind barriers.....44
Figure 4.11 Torsional aerodynamic response of thin girder (BD of 4.98) with different porosity wind barriers.....44
Figure 4.12 Vertical aerodynamic response of thick girder (BD of 3.44) with different installation methods.....45
Figure 4.13 Vertical aerodynamic response of thin girder (BD of 4.98) with different installation methods.....45
Figure 4.14 Torsional aerodynamic response of thick girder (BD of 3.44) with different installation methods.....46
Figure 4.15 Torsional aerodynamic response of thin girder (BD of 4.98) with different installation methods.....46
Figure 4.16 Vertical aerodynamic response of thick girder (BD of 3.44) with different bar arrangements.....47
Figure 4.17 Vertical aerodynamic response of thin girder (BD of 4.98) with different heights and bar arrangements.....47
Figure 4.18 Torsional aerodynamic response of thick girder (BD of 3.44) with different heights and bar arrangements.....48
Figure 4.19 Torsional aerodynamic response of thin girder (BD of 4.98) with different heights and bar arrangements.....48
Figure 4.20 Vertical aerodynamic response of thick girder (BD of 3.44) with wind barriers combined with flaps.....50
Figure 4.21 Vertical aerodynamic response of thin girder (BD of 4.98) with wind barriers combined with flaps.....50
Figure 4.22 Torsional aerodynamic response of thick girder (BD of 3.44) with wind barriers combined with flaps.....50

Figure 4.23 Torsional aerodynamic response of thin girder (BD of 4.98) with wind barriers combined with flaps 51
Figure 4.24 Wind velocity vector distribution of bare deck cases 53
Figure 4.25 Turbulence intensity distribution of bare deck cases 53
Figure 4.26 Wind velocity vector distribution of the standard wind barrier (50-H-3.0m) 53
Figure 4.27 Turbulence intensity distribution of the standard wind barrier (50-H-3.0m) 53
Figure 4.28 Peak vertical VIV amplitude of both girders 54
Figure 4.29 Mean turbulence intensity of thick girder (BD of 3.44) with wind barriers .56
Figure 4.30 Mean turbulence intensity of thin girder (BD of 4.98) with wind barriers ... 57
Figure 4.31 Mean wind velocity profile above both girders with different wind barriers 59
Figure 4.32 Maximum wind velocity profile above both girders with different wind barriers 60
CHAPTER 5 Mechanism of vertical vortex-induced vibration of a bluff box girder 64
Figure 5.1 Sectional models (unit: mm; scale: 1/100) 65
Figure 5.2 Details of wind barrier models (unit: mm; scale: 1/100) 66
Figure 5.3Vertical aerodynamic response of the girder with basic parameter wind barriers 68
Figure 5.4 Vertical aerodynamic response of the girder with countermeasures 69
Figure 5.5 Peak vertical VIV amplitude of both bluff and streamlined girders 70
Figure 5.6 Description of pressure distribution 71
Figure 5.7 Mean and fluctuating pressure coefficient distribution of the bluff girder (BD) and its fairing attachment (BD+FR) 72
Figure 5.8 Mean flow field of the bluff girder (BD) 72
Figure 5.9 Mean and fluctuating pressure coefficient distribution of the bluff girder (BD) with wind barriers 74
Figure 5.10 Mean wind flow field of the bluff girder (BD) 74
Figure 5.11 Mean wind flow field of the bluff girder (BD) with 25-H 74
Figure 5.12 Mean wind flow field of the bluff girder (BD) with 50-H-3.0m 74
Figure 5.13 Mean wind flow field of the bluff girder (BD) with 50-T 75
Figure 5.14 Mean and fluctuating pressure coefficient distribution of the bluff girder (BD) with countermeasures 76
Figure 5.15 Mean wind flow field of the bluff girder (BD) with 50-H-2.5m 76
Figure 5.16 Mean wind flow field of the bluff girder (BD) with 50-H-DS 76
Figure 5.17 Mean wind flow field of the bluff girder (BD) with 50-H+F 77
Figure 5.18 Spanwise correlation coefficient of the bluff girder (BD) with wind barriers 78

Figure 5.19 Mean and fluctuating pressure coefficient distribution of the bluff girder without fairing (BD) and with fairing (BD+FR) 79
Figure 5.20 Mean wind flow field of the bluff girder without fairing (BD) and with fairing (BD+FR) 79
Figure 5.21 Mean and fluctuating pressure coefficient distribution of the bluff girder with fairing (BD+FR) and wind barriers 80
Figure 5.22 Mean wind flow field of the bluff girder with fairing (BD+FR) with 25-H 81
Figure 5.23 Mean wind flow field of the bluff girder with fairing (BD+FR) with 50-H-3.0m 81
Figure 5.24 Mean wind flow field of the bluff girder with fairing (BD+FR) with 50-T 81
Figure A1.1 Wind velocity vector distribution with 25-H 88
Figure A1.2 Turbulence intensity distribution with 25-H 88
Figure A1.3 Wind flow field distribution of thin girder (BD of 4.98) with 50-H-2.5m 88
Figure A1.4 Wind velocity vector distribution with 50-H-DS 89
Figure A1.5 Turbulence intensity distribution with 50-H-DS 89
Figure A1.6 Wind velocity vector distribution with 50-H-DS+F 89
Figure A1.7 Turbulence intensity distribution with 50-H-DS+F 89
Figure A2.1 Vertical aerodynamic response of the girder with fairing attachment (BD+FR) and basic parameter wind barriers 90
Figure A2.2 Vertical aerodynamic response of streamlined girder with countermeasures 90
Figure A3.1 Pressure distribution of the girder with fairing attachment and wind barriers 91
Figure A4.1 Energy of each mode 92
Figure A4.2 Mean wind velocity (Top side) 92
Figure A4.4 PSD of temporal coefficient of modes 1 to 4 93
Figure A4.5 Energy of each mode 93
Figure A4.6 Mean wind velocity (Top side) 93
Figure A4.7 Vector field of modes 1 to 4 (Top side) 94
Figure A4.8 PSD of temporal coefficient of modes 1 to 4 (Top side) 94
Figure A4.9 Energy of each mode 95
Figure A4.10 Mean wind velocity (Top side) 95
Figure A4.11 Vector field of modes 1 to 4 (Top side) 95
Figure A4.12 PSD of temporal coefficient of modes 1 to 4 (Top side) 96
Figure A4.13 Energy of each mode 96
Figure A4.14 Mean wind velocity (Top side) 96
Figure A4.15 Vector field of modes 1 to 4 (Top side) 96

Figure A4.16 PSD of temporal coefficient of modes 1 to 4 (Top side) 97
Figure A4.17 Energy of each mode 97
Figure A4.18 Mean wind velocity (Top side) 97
Figure A4.19 Vector field of modes 1 to 4 (Top side) 98
Figure A4.20 PSD of temporal coefficient of modes 1 to 4 (Top side) 98
Figure A4.21 Energy of each mode 99
Figure A4.22 Mean wind velocity (Top side) 99
Figure A4.23 Vector field of modes 1 to 4 (Top side) 99
Figure A4.24 PSD of temporal coefficient of modes 1 to 4 (Top side) 100
Figure A4.25 Energy of each mode 100
Figure A4.26 Mean wind velocity (Top side) 100
Figure A4.27 Vector field of modes 1 to 4 (Top side) 101
Figure A4.28 PSD of temporal coefficient of modes 1 to 4 (Top side) 101
Figure A4.29 Energy of each mode 102
Figure A4.30 Mean wind velocity (Bottom side) 102
Figure A4.31 Vector field of modes 1 to 4 (Bottom side) 102
Figure A4.32 PSD of temporal coefficient of modes 1 to 4 (Bottom side) 103
Figure A4.33 Energy of each mode 103
Figure A4.34 Mean wind velocity (Bottom side) 103
Figure A4.35 Vector field of modes 1 to 4 (Bottom side) 104
Figure A4.36 PSD of temporal coefficient of modes 1 to 4 (Bottom side) 104
Figure A4.37 Energy of each mode 105
Figure A4.38 Mean wind velocity (Bottom side) 105
Figure A4.39 Vector field of modes 1 to 4 (Bottom side) 105
Figure A4.40 PSD of temporal coefficient of modes 1 to 4 (Bottom side) 106
Figure A4.41 Energy of each mode 106
Figure A4.42 Mean wind velocity (Bottom side) 106
Figure A4.43 Vector field of modes 1 to 4 (Bottom side) 107
Figure A4.44 PSD of temporal coefficient of modes 1 to 4 (Bottom side) 107
Figure A4.45 Energy of each mode 108
Figure A4.46 Mean wind velocity (Bottom side) 108
Figure A4.47 Vector field of modes 1 to 4 (Bottom side) 108
Figure A4.48 PSD of temporal coefficient of modes 1 to 4 (Bottom side) 109
Figure A4.49 Energy of each mode 109
Figure A4.50 Mean wind velocity (Bottom side) 109

Figure A4.51 Vector field of modes 1 to 4 (Bottom side) 110
Figure A4.52 PSD of temporal coefficient of modes 1 to 4 (Bottom side) 110

List of Tables

Table 4.1 Structural characteristic parameters for free vibration tests.....40
Table 5.1 Structural characteristic parameters for free vibration test 67

Nomenclature

α: Angle of attack

B: Width of the girder

B/D: Side ratio

BO: Bottom side of the girder

C: Center of the girder

C_D: Drag coefficient

CFD: Computational Fluid Dynamics

C_i: Sectional fluctuating lift force

C_L: Lift coefficient

C_M: Moment coefficient

$\overline{C_P}$: Mean pressure coefficient

$\widetilde{C_P}$: Fluctuating pressure coefficient

cov: Covariance

D: Depth of the girder

DO: Downstream side of the girder

δ_V: Damping in vertical mode (logarithmic decrement)

δ_T: Damping in torsional mode (logarithmic decrement)

E: Edge of the girder

f: Natural frequency

F_D: Drag force

F_L: Lift force

F_M: Moment

Fr: Froude number

f_s: Shedding frequency

g: acceleration due to gravity

I: Inertial moment

I_u: Turbulence intensity

L: Length of the girder

L1 to *L6*: Lanes 1 to 6

L_m: Length of model

L_r: Length of real bridge

m: Mass

P: Pressure

P_0: Upstream pressure by pitot tube

$\bar{P}$: Mean surface pressure

$\tilde{P}$: Fluctuating surface pressure

PIV: Particle Image Velocimetry

R_{C_i}: Spanwise correlation coefficient of sectional fluctuating lift force

Re: Reynolds number

Sc: Scruton number

S_t: Strouhal number

T: Top side of the girder

U: Wind velocity

UP: Upstream side of the girder

var: Variance

VIV: Vortex-Induced Vibrations

X/B: Normalized distance

X/D: Normalized distance

Y/D: Normalized height

$\Delta z/D$: Relative distance in the spanwise direction of the girder

λ: Scale factor

μ: Dynamic viscosity of fluid

ρ: Air density

CHAPTER 1
Introduction

1.1 Background

The advent of long-span bridges marks a significant advancement in modern infrastructure, facilitating the bridging of vast geographical divides to bolster economic and social integration. However, these bridges are often subjected to strong crosswinds due to their exposed locations. Such environmental conditions pose serious safety risks to vehicle driving traffic. Hence, wind-induced accidents of vehicles traveling on them, including side slips and rollovers, commonly occur. These incidents not only result in casualties but also lead to significant economic repercussions, encompassing both direct damages to infrastructure and vehicles, as well as indirect effects such as prolonged traffic disruptions and operational downtimes during strong crosswind conditions.

In response to these challenges, traditional mitigation strategies typically involve the implementation of vehicular speed limits, restrictions on types of vehicles allowed during high wind conditions, and occasionally, complete closures of bridges. Although these measures effectively reduce the frequency of accidents, they also cause severe traffic congestion and disrupt economic activities, particularly affecting the logistics sector. The limitations of such reactive traffic management strategies highlight the need for more proactive and sustainable engineering solutions.

Among various mitigative measures, wind barriers have become a preferred method to enhance driving safety on bridges. These barriers are specially designed to reduce wind loads on vehicles, thereby enhancing vehicle stability in crosswind conditions. However, the installation of wind barriers changes the configuration of bridge girders, altering the flow pattern around the bridge and increasing the windward surface area, which in turn, potentially escalates the aerodynamic loads. These consequences significantly affect the overall aerodynamic performance of bridges. While a specific wind barrier may improve the aerodynamic performance of bridges in some cases, more often, these barriers adversely impact it, resulting in discomfort usage, decreased lifespan, and in extreme cases, structural failures of bridges. The effects of wind barriers on driving safety enhancement of vehicles and aerodynamic performance of bridges significantly depend on several factors, including shapes, heights, configurations of openings, and placement methods along the bridge.

Investigating the effects of wind barriers is particularly significant for bridges with varying girder depths (different width-to-depth or side ratios, B/D), whose flow field and aerodynamic performance are distinctively affected by the side ratio along the bridge. The study can provide insights into the design and strategic installation of wind barriers for different side-ratio box girders at optimized installation sections to reduce the risk of driving safety at minimum expense for installation and maintenance together with the benefit of drag coefficient reduction and the limitation of the detrimental effect of wind barriers on the aerodynamic performance of bridges.

Since wind barriers can have either a positive or negative impact on the aerodynamic performance of bridges depending on their configuration and interaction with bridge structures, particularly, in box girders, which are favored for their structural efficiency and cost-effectiveness but with the disadvantage of being vulnerable to vertical Vortex-Induced Vibrations (VIV). Therefore, a comprehensive understanding of the mechanisms by which wind barriers affect vertical VIV in box girders is essential to help in establishing fundamental principles for designing wind barriers specifically for box girders, which can benefit both practical engineering applications and advancing scientific knowledge in the field. The study expects to decrease the reliance on wind tunnel testing to save time and budget and offer a deeper understanding of the characteristics of wind-structure interaction of bluff box girders with different side ratios equipped with wind barriers.

Figure 1.1 Wind-induced traffic accidents (Zhang et al., 2020)

Figure 1.2 Wind barrier installed on the handrail with on-site wind speed measurement (Yang et al., 2022)

1.2 Objectives

The primary aims of this study are to enhance the driving safety of vehicles and to ensure the aerodynamic performance of bridges with varying side ratios of the girders. In addition to understand the mechanisms of vertical vortex-induced vibration (VIV) affected by wind barriers in a bluff box girder. Through comprehensive experimental investigations using wind tunnel tests. The specific objectives of this study are:

1) Investigating the effects of wind barrier parameters on the aerodynamic performance and wind flow field of a bluff box girder with two side ratios of 3.44 and 4.98.
2) Clarifying the mechanism relating to the effect of wind barriers on the vertical vortex-induced vibration (VIV) of a bluff box girder with a side ratio of 5.00.

1.3 Structure

Chapter 1, this opening chapter sets the stage by introducing the topic and motivation encompassing wind-induced traffic accidents and the effect of wind barriers on the wind flow field and aerodynamic performance of different side-ratio box-girder bridges, stating the research objectives, and highlighting the significance of the study.

Chapter 2 provides a detailed review of the related theories and literature, covering topics of wind-induced traffic accidents and their measures, basic principles of bluff body aerodynamics, and fundamental aerodynamic responses of long-span bridges including deeper details of vertical vortex-induced vibrations (VIV). Additionally, the wind tunnel tests that were used as a tool for this study are introduced in this chapter. Finally, several past research on the effects of wind barriers on driving safety and the aerodynamic performance of bridges are discussed in detail.

Chapter 3 describes the experimental approach employed in the research, starting with the outline of the wind tunnel, and then detailing the setup of various tests in the wind tunnel aimed at achieving research objectives, including the methodologies for data collection and analysis.

Chapter 4 focuses on presenting and analyzing the data related to the first objective of the study. This chapter evaluates and discusses how wind barriers influence the aerodynamic performance and wind flow field of bluff-box girders with different side ratios to guarantee the stability of the bridge and vehicles.

Chapter 5 includes the results and discussion of the second objective by analyzing how wind barriers affect the mechanism of the vertical VIV in a bluff box girder including both stabilization by proposed countermeasures, such as triangular wind barrier and fairing, and destabilization by wind barriers. The chapter discusses the implications of these findings on the design and functionality of wind barriers specifically for the bluff girder.

Chapter 6 summarizes the key findings of the study and provides recommendations for future research and potential applications of the research outcomes.

References

Yang, Y., Zhang, J., Cao, F., Ge, Y., Zhao, L., 2022. Evaluation and improvement of wind environment and vehicle safety on long-span bridge deck under strong crosswind. Journal of Wind Engineering and Industrial Aerodynamics 228, 105089. https://doi.org/10.1016/j.jweia.2022.105089

Zhang, Q., Su, C., Wang, Y., 2020. Numerical investigation on aerodynamic performance and stability of a sedan under wind–bridge–tunnel road condition. Alexandria Engineering Journal 59, 3963–3980. https://doi.org/10.1016/j.aej.2020.07.004

CHAPTER 2
Theoretical background and literature review

2.1 Wind-induced accidents and their measures

Wind-induced accidents of vehicles and trains on bridges are a critical area of concern within the field of wind engineering. Bridges, by their nature and structural exposure, are vulnerable to strong lateral winds, which can significantly influence vehicle stability. The impact of wind on vehicles, especially high-profile and high-sided vehicles such as trucks and buses, is predominantly due to the aerodynamic forces exerted by both steady and gusty winds. These forces can cause vehicles to veer off their paths or even overturn in severe cases (Kim et al., 2020, 2022). Additionally, wind-induced vibrations of the bridge itself can also contribute to accidents by affecting the control and operational stability of vehicles (Liu et al., 2023).

Wind-induced accidents have resulted in significant losses over the years, demonstrating the perilous nature of strong wind conditions on transportation systems. In Poland, according to a 2017 police report, strong wind gusts contributed to 300 road accidents, which tragically resulted in 30 fatalities and nearly 400 injuries (Betkier et al., 2019). Similarly, in the Kansai region of Japan, 43 vehicle rollovers were documented during Typhoon No. 20 and No. 21 in 2018, with additional incidents occurring during Typhoon No. 15 in 2019, highlighting the recurring threat posed by typhoon-induced winds (Kim et al., 2021). The impact on rail transport is equally concerning. Since the inception of Japanese railways in 1872, there have been 28 wind-induced train accidents. A notable disaster occurred in 1986 when 7 coaches hauled by a heavy diesel locomotive were blown off the Amarube Bridge due to strong winds, resulting in 6 fatalities and 6 injuries (Fujii et al., 1999).

The stability of vehicles on bridges under strong crosswinds is fundamentally governed by aerodynamic coefficients, especially those relating to lateral or side force. These coefficients, which represent the forces exerted by the wind on moving vehicles, are influenced by several factors including wind speed and direction. As wind speed increases, the lateral force on the vehicle also increases, thereby exacerbating its instability. Furthermore, wind gustiness or fluctuation introduces sudden, unpredictable changes in these forces, significantly challenging the driver's ability to maintain control. The effect of vehicle speed on aerodynamic interactions is complex. Increased vehicle speed modifies the relative velocity between the vehicle and the wind, consequently altering the effective wind speed encountered (Fujii et al., 1999; Kim et al., 2020; Zhang et al., 2020).

Additionally, the aerodynamic design of the vehicle plays a crucial role. Vehicles with higher profiles, due to their larger surface areas exposed to wind, are inherently more susceptible to side forces than those with lower profiles. Moreover, bridge configuration significantly influences the vehicles. The interaction between the vehicle and the bridge’s structural elements, including variations in height, length, and spacing, can markedly influence the aerodynamic forces experienced by the vehicle. Such interactions can modify wind flow patterns across the bridge deck, impacting vehicle stability (Kim et al., 2021).

In the context of bridges with varying-depth girders, the side ratios, which vary along the length of the bridge, significantly influence the wind flow. This variation in bridge configuration alters both the aerodynamic performance of the bridge and the driving stability of vehicles. Extensive research, employing methodologies such as field measurements, wind tunnel experiments, and computational fluid dynamics (CFD), has been conducted to investigate these effects.

For larger side ratios (thin girders), the airflow tends to have a relatively lower separated shear layer with reattached flow patterns, in contrast to smaller side ratios (thick girders), which demonstrate a higher separated shear layer with detached flow type. Consequently, wind speeds are generally higher around thinner girders, accompanied by more significant wind fluctuations, thereby increasing susceptibility to vehicle instabilities and potential accidents (Kaneko et al., n.d.; Kim et al., 2021, 2023).

In terms of aerodynamic forces on vehicles, particularly lateral forces, are markedly higher in scenarios involving thin girders. These forces tend to increase as the side ratios are larger. Nonetheless, contrasting findings have been reported in a study that while the lateral force coefficients on vehicles in the center and windward lanes of bridges increased with decreasing side ratios, these coefficients decreased in the leeward lane, illustrating the complex interaction between wind flow, vehicle aerodynamics, and bridge design (Kim et al., 2021).

To mitigate the risks of wind-induced accidents, a range of strategies have been developed, particularly in areas prone to strong winds such as regulating the speeds of trains and vehicles based on real-time weather conditions, and the closure of bridges. The use of advanced forecasting and monitoring technologies including systems equipped to track wind patterns and predict potential high-wind events are integral to this process. They enable the initiation of pre-emptive safety measures. This integration of predictive analytics into operational protocols represents a significant advancement in efforts to mitigate the dangers posed by high winds.

One popular solution to reduce wind impact is the installation of wind barriers. These barriers are strategically designed and placed to effectively reduce wind speed and disrupt wind flow patterns. Research has shown that wind barriers with varying shapes, heights, and solidity ratios can be specifically designed to meet the needs of a particular area and the typical wind conditions it faces. The effectiveness of these barriers in preventing wind-induced accidents has been extensively studied globally (Fujii et al., 1999; Zhang et al., 2020).

The wind barriers are often assessed through wind tunnel testing and CFD simulations. These methods help determine the most effective configurations that minimize the detrimental aerodynamic impact on bridges while providing significant protection against high winds. Additionally, field measurements have been conducted to confirm the effectiveness of these barriers in real-world conditions.

Overall, the strategies for mitigating wind-induced risks involve a combination of technological integration and structural adaptations. By employing a mix of speed regulation, advanced predictive systems, and wind barriers, it is possible to significantly reduce the occurrence of accidents caused by high winds. This holistic approach not only enhances safety but also ensures the continued functionality of key infrastructure in adverse weather conditions.

2.2 Basic principles of bluff body aerodynamics

2.2.1 Flow separation and vortex shedding

Flow separation occurs when the boundary layer of airflow, which is the layer of air in contact with the surface of the structure, detaches from the surface. This detachment generally happens when the boundary layer cannot withstand the adverse pressure gradient caused by the geometry or wind direction change. In the case of a rectangular bluff body, flow separation is prominently observed at the edges and corners where the flow path changes.

The point of separation is critical because it marks the beginning of a region of recirculating flow behind the body, known as the wake. The size and shape of the wake depend on the bluff body configurations (Figure 2.1). The flow within the wake is highly turbulent with lower pressure than the undisturbed flow. This pressure difference between the front and rear faces of the body generates lift and drag forces, with drag being particularly significant in bluff bodies due to the larger wake.

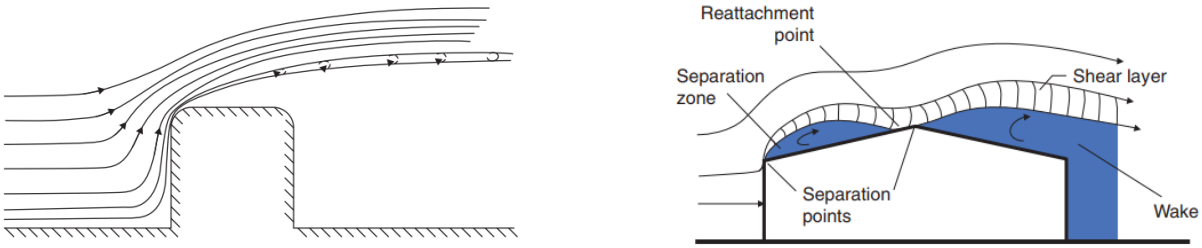

(a) Flow separation at the corner of obstacle (b) Flow around a building

Fig 2.1 Flow separation and vortex shedding (Simiu and Yeo, 2019)

Vortex shedding is a phenomenon that occurs when alternating low-pressure vortices are created as the flow is separated. These vortices form a pattern known as a von Kármán vortex street, which involves the shedding of vortices from each side of the body in an alternating way as in Figure 2.2 (Simiu and Yeo, 2019).

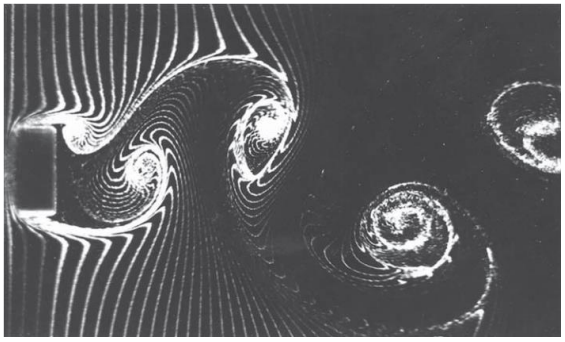

Fig 2.2 Flow and vortex shedding around a rectangular cylinder (Re = 200) (Simiu and Yeo, 2019)

The frequency of vortex shedding is determined by the Strouhal number, a dimensionless parameter that relates the frequency of vortex shedding to the bluff body's width and flow velocity. For rectangular bodies, the sharp corners enhance the formation of strong vortices compared to more aerodynamically shaped bodies (Simiu and Miyata, 2006; Simiu and Yeo, 2019).

2.2.2 Pressure distribution and aerodynamic force coefficients on a bluff body

Pressure distribution around a rectangular bluff body is highly dependent on its shape, wind direction, Reynolds number, and the turbulence of the incoming flow. When wind encounters a bluff body, it exerts static pressure on the windward face, creating a high-pressure zone (directed inward toward the body, positive pressure), while a low-pressure zone (directed outward from the body, negative pressure) forms on the leeward side in the wake region. This pressure differential across the structure creates net forces that can affect structural integrity, leading to specific aerodynamic responses of the body.

The net forces, derived from the integration of pressure over the body's surface, result in force components. These components, in the along-wind and across-wind directions, are termed drag (F_D) and lift (F_L), respectively. Meanwhile, the rotation force about the elastic center is termed the moment (M).

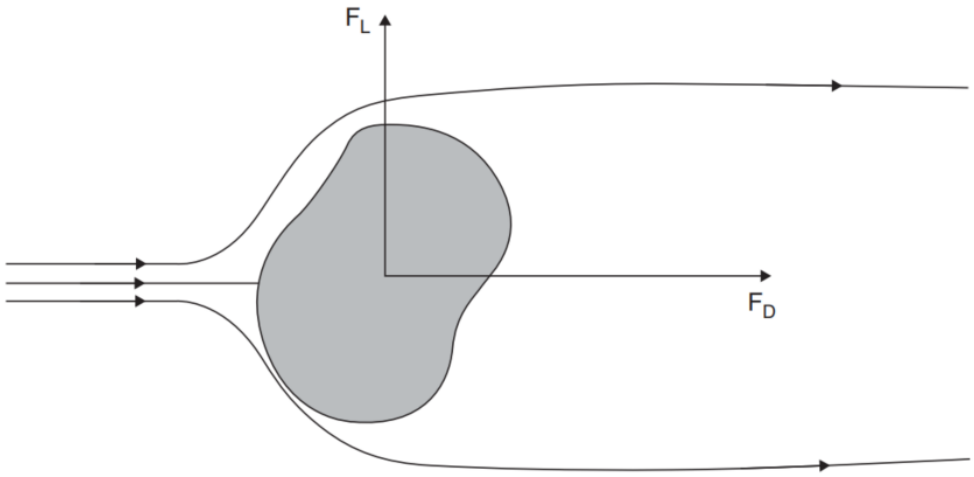

Fig 2.3 Lift and drag on an arbitrary bluff body (Simiu and Yeo, 2019)

The pressure normally refers to the mean dynamic pressure ½ ρU^2 of the upstream flow. Therefore, non-dimensional pressure coefficients, (C_p) describing the pressure at a point on a surface relative to the ambient air pressure are defined as:

$$C_P = \frac{P - P_0}{\frac{1}{2}\rho U^2} \qquad \text{Eq. 2.1}$$

Likely, the force components are also typically normalized and represented by drag, lift and moment coefficients (C_D, C_L and C_M, respectively) as follows:

$$C_D = \frac{F_D}{\frac{1}{2}\rho\, U^2 B}$$

$$C_L = \frac{F_L}{\frac{1}{2}\rho\, U^2 B} \qquad \text{Eq. 2.2 (a, b, c)}$$

$$C_M = \frac{M}{\frac{1}{2}\rho\, U^2 B^2}$$

where U is the mean reference wind speed. $P - P_0$ is the pressure difference between local and upstream pressure. ρ is air density. B is the reference dimension of the body. The non-dimensional form of the pressure and forces facilitates scaling experimental results from models to full-scale structures and helps establish reference values for specific geometric shapes (Simiu and Miyata, 2006; Simiu and Yeo, 2019).

2.3 Fundamental aerodynamic responses of long-span bridges

Long-span bridges, due to their extensive exposure to wind forces, are susceptible to various aeroelastic instabilities. These instabilities, which result from the interaction between aerodynamic forces and the elastic properties of the structure, can significantly impact the safety and lifespan of bridges. Some fundamental aeroelastic phenomena relevant to bridge engineering including vortex-induced vibrations (VIV), galloping, and torsional flutter are discussed in the section. Each of these instabilities contributes uniquely to the challenges faced in the design and maintenance of long-span bridges.

2.3.1 Vortex-induced vibrations

2.3.1.1 Mechanism of VIV

This vibration begins with the shedding of vortices from the body of the bridge as wind flows around it. This vortex shedding occurs alternately from opposite sides of the bridge's structure, creating a fluctuating pressure distribution around the bridge. The frequency at which these vortices shed is known as the shedding frequency (f_s), and can be estimated by the Strouhal number dimensionless number (S_t) describing oscillating flow mechanisms:

$$f_s = S_t \frac{U}{D} \qquad \text{Eq. 2.3}$$

where U is the wind speed and D is a characteristic dimension of the bridge (typically depth).

As the shedding frequency aligns with the natural frequency of a bridge, a resonance condition can occur, leading to the amplification of the bridge's vibrations. This synchronization of frequencies defines the "lock-in" region as described in Figure 2.4. This

phenomenon typically occurs at specific wind speeds depending on the configuration and properties of bridges.

During the "lock-in" phase, even slight variations in wind speed can shift the shedding frequency away from the bridge's natural frequency. However, when within the lock-in range, the shedding frequency tends to remain close to the structural frequency due to mutual energy exchange between the wind-induced forces and the oscillating structure. This interaction ensures that even if the wind speed varies within a certain range, the shedding frequency can adjust to maintain the lock-in condition, prolonging the resonance effect.

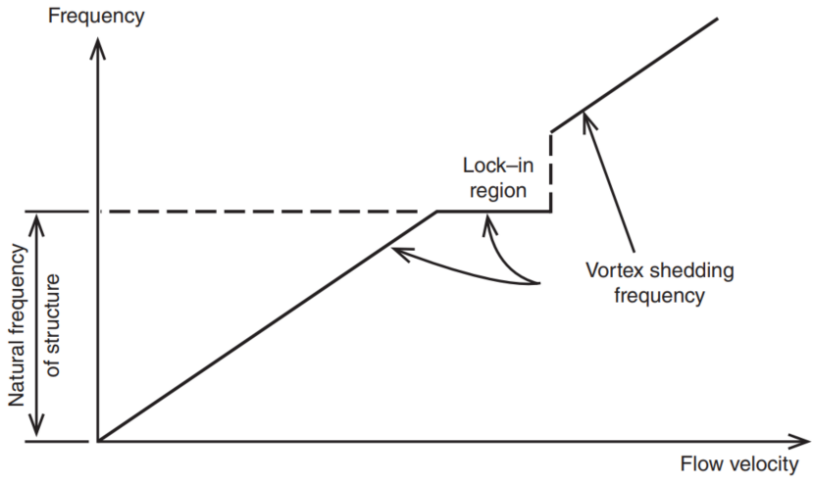

Fig 2.4 Frequency of vortex shedding as a function of wind velocity (Simiu and Yeo, 2019)

This type of vibration is often self-limiting, meaning that it will not increase indefinitely (no convergence). The amplitude of vibration typically reaches a peak due to several factors, including aerodynamic damping and the structural damping properties of the bridge. Aerodynamic damping occurs when the motion of the structure alters the flow field around it in a way that reduces lift and other aerodynamic forces contributing to the vibration. Structural damping refers to the intrinsic ability of the material and construction to dissipate vibrational energy (Simiu and Miyata, 2006; Simiu and Yeo, 2019).

2.3.1.2 Effects of VIV on bridges

Vortex-induced vibrations may not directly cause bridge collapses, but their impact on bridge usage and longevity is profound and multifaceted. Constant exposure to these vibrations introduces repeated stress cycles into structural components, which over time can lead to fatigue damage. This fatigue is particularly detrimental as it progressively weakens metal and concrete elements, making them susceptible to cracks and potential structural failures. Such degradation not only compromises the structural integrity but also necessitates frequent inspections and costly repairs to maintain safety and functionality.

Beyond structural concerns, the dynamic responses induced by VIV can significantly diminish the comfort and safety of bridge users. These vibrations can be perceptible to

pedestrians and motorists alike, potentially causing discomfort or even motion sickness in sensitive individuals. More critically, the oscillations can affect vehicle handling, increasing the risk of accidents, especially during high wind conditions.

The operational implications of VIV are also considerable. To manage the risks associated with high winds and ensure the safety of bridge users, traffic flow may be restricted or slowed, particularly during storm events when VIV is likely to be more pronounced. Such limitations not only affect the efficiency of the transportation network but also lead to increased operational costs. Traffic restrictions can disrupt daily commutes and commercial transport, leading to economic implications for communities reliant on bridge routes. Thus, while VIV does not typically result in catastrophic failures, its influence on maintenance budgets, operational protocols, and overall bridge functionality underscores the need for effective vibration mitigation strategies in bridge design and maintenance.

2.3.1.3 Suppression of VIV

Several strategies can be employed to reduce the effects of VIV, ranging from aerodynamic modifications of the bridge to the implementation of mechanical damping systems.

One effective method to mitigate VIV is through aerodynamic configuration of bridge components. By altering the shape and profile of bridge decks and girders, engineers can modify the flow patterns around these structures, thereby altering the vortex-shedding characteristics. For example, adding fairings or aerodynamic edge modifications can streamline the flow, reducing the formation of coherent vortex-shedding patterns. These modifications help shift the natural frequencies of the structure or alter the critical wind speeds at which lock-in occurs, thus avoiding the resonance conditions that lead to large amplitude vibrations.

Another common approach is the installation of mechanical damping systems, such as tuned mass dampers (TMDs), which are designed to absorb and dissipate the energy of the oscillations induced by VIV. These dampers are tuned to a specific frequency that closely matches the bridge's natural frequency, allowing them to effectively reduce the amplitude of vibrations by introducing counteracting forces during motion.

Increasing the stiffness of bridge elements is also a viable approach. By enhancing the stiffness, the natural frequency of the bridge is increased, which may move it out of the critical wind speed range prone to VIV. This method can be particularly effective when combined with aerodynamic modifications (Simiu and Miyata, 2006; Simiu and Yeo, 2019).

2.3.2 Galloping

Galloping is an aeroelastic instability characterized by large amplitude oscillations. It is distinct from VIV which is associated with the reattachment of separated vortices while galloping typically occurs at higher wind speeds and does not involve flow reattachment. The asymmetry in the lift coefficient causes galloping to vibrate the structure in a direction perpendicular to the wind flow which might result in the collapse of the bridge.

Designing bridge girders with aerodynamically stable configurations is a fundamental approach to mitigate galloping by utilizing streamlined or aerodynamically tapered sections stabilizing the lift forces across the structure. For example, adding triangular fairings or

modifying the girder's cross-sectional shape to be more symmetrical can help in balancing the lift forces generated at different angles of attack. Additionally, active control systems such as controllable flaps or surface modifications can be used to alter the aerodynamic properties dynamically in response to wind conditions. While streamlined girders may suppress galloping by promoting flow reattachment, it could inadvertently increase the amplitude of VIV, representing a design trade-off.

The critical condition for galloping to be possible to occur is defined by the Den Hartog criterion, which relates the wind speed and structural damping to the geometry and dynamic properties of the structure. According to Simiu and Scanlan, galloping occurs when the aerodynamic damping factor is negative, which can be assessed by evaluating the mean lift and drag coefficients of a bluff body and determining whether the left-hand side of Eq. (20.14) is negative.

$$\left(\frac{dC_L}{d\alpha} + C_D\right)_{\alpha=0} < 0 \qquad \text{Eq. 2.4}$$

Where C_L and C_D are lift and drag coefficients, respectively and α is the angle of attack. It is important to note that the quasi-steady theory, which describes self-excited forces as those acting on a stationary body, only applies if there is no flow reattachment. This condition is typically observed in bridge girders with side ratios $B/D < 2$ and flows with relatively high reduced velocities (Simiu and Miyata, 2006; Simiu and Yeo, 2019).

2.3.3 Torsional flutter

Torsional flutter is a critical aeroelastic instability that poses significant risks to long-span bridges, particularly those featuring flexible and relatively flat girders. This phenomenon is characterized by self-excited oscillations whose amplitudes can grow progressively, potentially leading to catastrophic structural failures.

Torsional flutter typically occurs when the aerodynamic forces acting on a bridge reach a critical state where they cause the bridge to oscillate in a torsional manner around its longitudinal axis.

The onset of flutter is determined by several factors, including the bridge's aerodynamic properties, stiffness, mass distribution, and damping characteristics. Flutter becomes a concern when the damping effects, which normally serve to stabilize the structure by dissipating energy, are overcome by aerodynamic forces that effectively produce negative damping. This negative damping occurs at a critical wind speed, beyond which any small perturbation from the structure's equilibrium state doesn't dampen but instead grows over time.

Without considering mechanical damping, the stability of a structure under aerodynamic loading can be described as follows: A structure is considered aeroelastically stable if, after a small perturbation, it returns to its original position due to stabilizing aerodynamic forces. However, as wind speeds increase, these forces can change character. At a critical velocity, the forces no longer stabilize the structure but render it neutrally stable. Beyond this critical point, the aerodynamic forces act to continuously amplify any oscillations caused by perturbations, contrasting to VIV where oscillations are confined to specific wind speed ranges (the lock-in region) (Simiu and Miyata, 2006; Simiu and Yeo, 2019).

2.4 Wind tunnel test

2.4.1 Introduction to wind tunnels

Wind tunnels are essential tools in the field of aerodynamics, offering invaluable insights into the interactions between air and various solid bodies. Originally developed for aviation research, their application has broadened significantly, encompassing areas such as automotive engineering, sports, and notably, civil engineering, particularly in the study and design of bridges.

In the context of bridge engineering, wind tunnels are employed to simulate the complex environmental conditions that bridges are subjected to. This simulation is crucial for ensuring the safety and stability of bridge structures, especially for those spanning great distances, such as suspension or cable-stayed bridges. By conducting tests within a wind tunnel, engineers can observe the effects of wind on a scaled model of the bridge. This method allows for a detailed examination of how wind forces affect the bridge, from the overall load distribution to the localized impacts on specific components.

There are different wind tunnel types depending on specific testing needs and environments:

- Open-Circuit Wind Tunnels: These tunnels draw air from the environment, pass it over the object, and exhaust it back into the atmosphere. They are simpler and cost less but can suffer from varying air quality and temperature.
- Closed-Circuit Wind Tunnels: Featuring a closed loop through which air circulates continuously, these tunnels offer more control over airflow and quality, making them suitable for more precise aerodynamic testing.
- Atmospheric Boundary Layer Wind Tunnels: Specially designed for civil engineering applications, these tunnels simulate the lower atmosphere's wind profile, including turbulence and ground effects, which are crucial for accurately assessing wind loads on structures like bridges.

Section model tests play a critical role in the aerodynamic optimization of bridge decks. These tests are typically conducted during the design phase when selecting a bridge deck cross-section. The primary goal is to minimize the negative impacts of wind-induced vibrations, such as vortex-induced vibration and flutter, which can compromise bridge performance. While the approach of using section model tests might lead to a more conservative deck selection, it enables engineers to make a dependable choice with relative ease.

In a section model test, a rigid model representing a specific part of the structure—such as a segment of the bridge deck or a tower—is utilized. This model is typically supported by springs to simulate real-world dynamical interactions with wind. One of the advantages of this testing method is that it allows the use of a larger-scale model compared to full structure tests. This larger scale is beneficial as it facilitates a more accurate reproduction of the geometrical details of the actual bridge, and achieves higher Reynolds numbers, enhancing the test's relevance to real-life conditions.

Moreover, section model tests require significantly less time and effort compared to full bridge model tests. This efficiency makes it a preferred choice in the early stages of design, allowing for quick iterations and modifications based on test results. The ability to focus on

specific components of the bridge in these tests also provides detailed insights into how different design elements react to wind forces.

Wind tunnels offer significant advantages in the field of aerodynamics, particularly for testing and improving the design of various structures and vehicles. One of the primary advantages is the ability to control environmental conditions precisely, allowing researchers and engineers to test the effects of wind on models under consistent, repeatable settings. Wind tunnels also enable the testing of aerodynamic properties without the risks and costs associated with full-scale prototypes, making them a safer and more cost-effective option for initial testing phases.

However, there are some disadvantages to using wind tunnels. The main limitation is the scale; wind tunnels typically require scaled-down models of actual structures or vehicles, which might not perfectly capture all the aerodynamic behaviors of the full-sized versions. This can lead to discrepancies between wind tunnel results and actual performance. Additionally, operating and maintaining a wind tunnel can be expensive, particularly for those that require larger or more specialized testing environments. These facilities also consume a significant amount of energy, especially high-speed tunnels, adding to operational costs. Despite these challenges, the benefits of wind tunnels often outweigh the disadvantages, making them an indispensable tool in aerodynamics research and engineering (Simiu and Miyata, 2006; Fujino et al., 2012; Simiu and Yeo, 2019).

2.4.2 Basic scaling laws and similarity requirements

In wind tunnel testing, the accuracy and relevance of the results significantly depend on how well the test model replicates the physical and aerodynamic properties of the actual structure. Scaling laws and similarity requirements are fundamental principles that ensure the validity of wind tunnel tests by guaranteeing that the flow conditions around a model realistically simulate those around the full-scale structure. Understanding these principles is crucial for engineers and researchers to conduct meaningful and applicable aerodynamic tests.

1) Geometric similarity means that every dimension of the model is an exact, scaled-down version of the real structure. This requires that all lengths in the model are consistently reduced by the same scale factor. The scale factor λ is defined as:

$$\lambda = \frac{L_m}{L_r} \qquad \text{Eq. 2.4}$$

where L_m is a specific length on the model and L_r is the corresponding length on the real (or prototype) structure. However, in some cases, it is not applicable to reproduce all components of the prototype to the scaled model.

2) Kinematic Similarity

Kinematic similarity involves ensuring that the motion of the fluid relative to the model has the same characteristics as the motion relative to the actual prototype. This is commonly quantified using the Reynolds number (*Re*), a dimensionless number that helps in comparing the flow conditions between the model and the prototype. The Reynolds number is defined as:

$$Re = \frac{\rho U L}{\mu} \quad \text{Eq. 2.5}$$

where ρ is the fluid density, U is the velocity of the fluid, L is a characteristic length, and μ is the fluid's dynamic viscosity. For smaller models, achieving the prototype's Reynolds number may require either very high air speeds or working with a different fluid or may not always be possible since the Reynolds number is the ratio of inertial forces to viscous forces within a fluid that is subjected to relative internal movement due to different fluid velocities. If the Reynolds number is not matched, the flow characteristics (like turbulence and boundary layer transition) around the model may not accurately represent the flow around the actual bridge.

3) Dynamic Similarity

Dynamic similarity involves scaling the forces and their effects such that the model accurately represents the dynamic response of the prototype under similar conditions. This involves maintaining the same values of non-dimensional numbers like the Strouhal number (Eq. 2.3) for vortex shedding and the Froude number (Fr) for effects related to gravity (Simiu and Miyata, 2006; Fujino et al., 2012; Simiu and Yeo, 2019).

$$Fr = \frac{U^2}{gD} \quad \text{Eq. 2.6}$$

Where U is the velocity of the flow, D is a characteristic dimension and g is the acceleration due to gravity.

2.4.3 Principles of Particle Image Velocimetry (PIV)

Particle Image Velocimetry (PIV) is a quantitative flow measurement technique used to obtain instantaneous velocity measurements and related properties in fluid flows. This non-intrusive method captures the movement of seeded particles within a fluid, providing high-resolution spatial and temporal data that is crucial for understanding complex flow dynamics. The below procedures briefly explain the PIV technique.

1) Seeding the flow

The accuracy of PIV largely depends on the characteristics of the tracer particles used. These particles must be small enough to faithfully follow the fluid's flow without affecting its natural state, yet large enough to scatter sufficient light for detection. Typically, these particles are made from materials like polystyrene or glass and are coated to enhance their reflective properties. The seeding density is also crucial; too few particles will result in inadequate data, while too many could lead to overlapping images and errors in analysis.

2) Illumination techniques

Illumination in PIV is typically achieved using lasers, as they provide the intense, coherent light necessary for illuminating the particles effectively. The most common setup includes a pulsed Nd:YAG laser, which emits light at a wavelength that maximizes the reflection from the particles while minimizing the background noise. The laser light is formed into a sheet that intersects the fluid flow at the region of interest, lighting up the plane that contains the tracer

particles. Synchronizing the laser pulses with the camera's capture rate is essential for accurate measurement.

3) Image capture

High-speed cameras equipped with sensitive detectors are generally used to capture the scattered light from the particles. The camera must be positioned to view the illuminated plane at a right angle, ensuring that the particles' movements are recorded accurately over time. The timing between successive images is critical and is known as the interframe time. This interval must be short enough to capture the movement of particles between frames but long enough to ensure measurable displacement.

4) Image processing

The heart of PIV analysis lies in the image processing techniques employed to convert raw images into vector fields that represent the flow velocity. Each image is divided into small interrogation windows. Cross-correlation algorithms are then applied to these windows to determine the average particle displacement between successive images. The peak of the cross-correlation function indicates the most probable displacement of particle groups within each window. This process is repeated across the entire image to build up a complete velocity field.

5) Data analysis

The resulting vector fields from the image processing stage are analyzed to extract meaningful physical quantities such as velocity, vorticity, and shear stresses. Outliers in the data—often caused by reflections, foreign particles, or errors in correlation—need to be identified and corrected. This may involve smoothing techniques or statistical methods to refine the data. Additionally, time-averaging of the velocity fields can be performed to study steady-state flows, while fluctuating components can be analyzed to understand turbulence characteristics.

PIV has emerged as a powerful tool in the field of structural engineering, particularly in understanding the aerodynamic responses of bridge girders. The complex flow patterns and vortex-shedding behaviors around these structures can significantly influence their aerodynamic stability and performance. PIV provides a detailed visualization and quantitative analysis of these flow characteristics, facilitating the development of designs that can withstand aerodynamic loads and reduce wind-induced vibrations.

One of the primary applications of PIV in bridge aerodynamics is the visualization of flow patterns around girders. By seeding the airflow around scale models of bridges in wind tunnels with tracer particles, engineers can use PIV to capture the formation and evolution of vortices and wake structures. This is particularly important for box girders, which are susceptible to complex flow phenomena such as vortex shedding and buffeting. The detailed velocity fields obtained from PIV allow engineers to see how air moves around and through the girder sections, which is crucial for identifying critical regions where flow separations may occur.

Besides, the data from PIV studies enable the calibration of numerical models that simulate the aerodynamic behavior of bridges under various wind conditions and evaluate the effectiveness of aerodynamic modifications such as fairings, guide vanes, or changes in cross-sectional shape. By comparing the flow fields around modified and unmodified sections of

bridge girders, engineers can assess how changes in geometry affect the flow characteristics and, consequently, the aerodynamic forces.

Particle Image Velocimetry has revolutionized the field of experimental fluid mechanics by providing a robust, precise, and flexible method for visualizing and quantifying fluid flows. As technology advances, the scope and accuracy of PIV continue to expand, opening new avenues for research and application in science and engineering.

2.5 Effects of side ratios of the bluff body on wind flow and aeroelastic instabilities

The side ratio of a bluff body, denoted as *B/D* (where *B* is the width and *D* is the depth of the cylinder), particularly in the context of bridge engineering, plays a crucial role in determining its aerodynamic and aeroelastic behaviors. This section delves into how variations in the side ratio of bluff bodies such as bridge girders and rectangular cylinders influence wind flow patterns around them and the resultant aeroelastic instabilities.

Unlike bodies with smooth, curved surfaces where flow separation depends predominantly on the Reynolds number (Re), the flow around bluff bodies with sharp edges, such as rectangular cylinders, separates at fixed points determined by their geometry. In general, the separation of this shape does not mainly depend on Re, making the side ratio a more dominant factor in the flow characteristics. In Figure 2.5, distinct jumps in the Strouhal number, a dimensionless number used to describe oscillating flow mechanisms and reflect the frequency at which vortices shed from the structure, are observed at certain side ratios *B/D* of 2.8 and 6.0. Moreover, the flow behaves differently. At lower side ratios, specifically below 2.8, there is no reattachment of the flow on the surface of the body. Between side ratios of 2.8 and 6.0, reattachment occurs periodically, whereas, for side ratios exceeding 6.0, the flow reattaches completely (Simiu and Miyata, 2006).

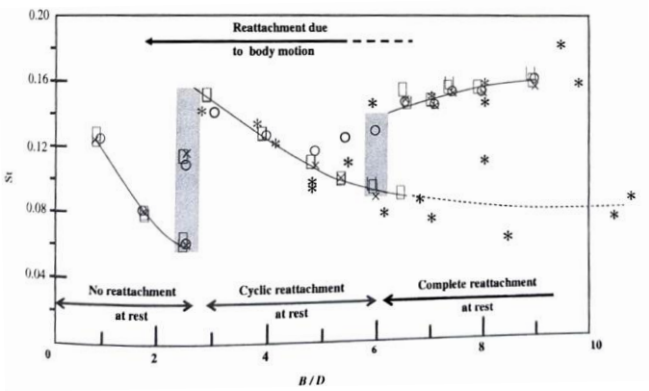

Fig 2.5 Strouhal number *St* for rectangular cylinders as a function of side ratio *B/D* and for bridge decks (Simiu and Miyata, 2006)

At a side ratio of 1 and a Scruton number ranging from 20 to 80, the dominant vibration mode is galloping. The Scruton number is a dimensionless quantity defined as in equations

2.6a and 2.6b for vertical and torsional vibration modes, where m and I are the mass and moment inertia per unit length, ζ is the damping ratio, ρ is the air density, and D is the depth of the cylinder. As the side ratio increases to 2, the vibrations are dominated by vortex-induced vibrations, and without the occurrence of galloping at the same Scruton number of 40. Further increase of the side ratio to 3 and 4 shifts the dominant vibration mode to a combination of VIV and torsional flutter synchronizing with the flow reattachment as previously discussed (Simiu and Miyata, 2006).

$$Sc = \frac{2m\delta_V}{\rho D^2}$$

$$Sc = \frac{2I\delta_T}{\rho D^2}$$

Additionally, Saito and Sakata (1999) noted that a decreasing side ratio in bridge girders increases their vulnerability to galloping and vortex-induced vibrations. Typically, a side ratio of 4 serves as a threshold, differentiating the aerodynamic behaviors of bridge girders concerning susceptibility to galloping. As illustrated in Figure 2.8, girders with a side ratio exceeding 4 do not experience galloping.

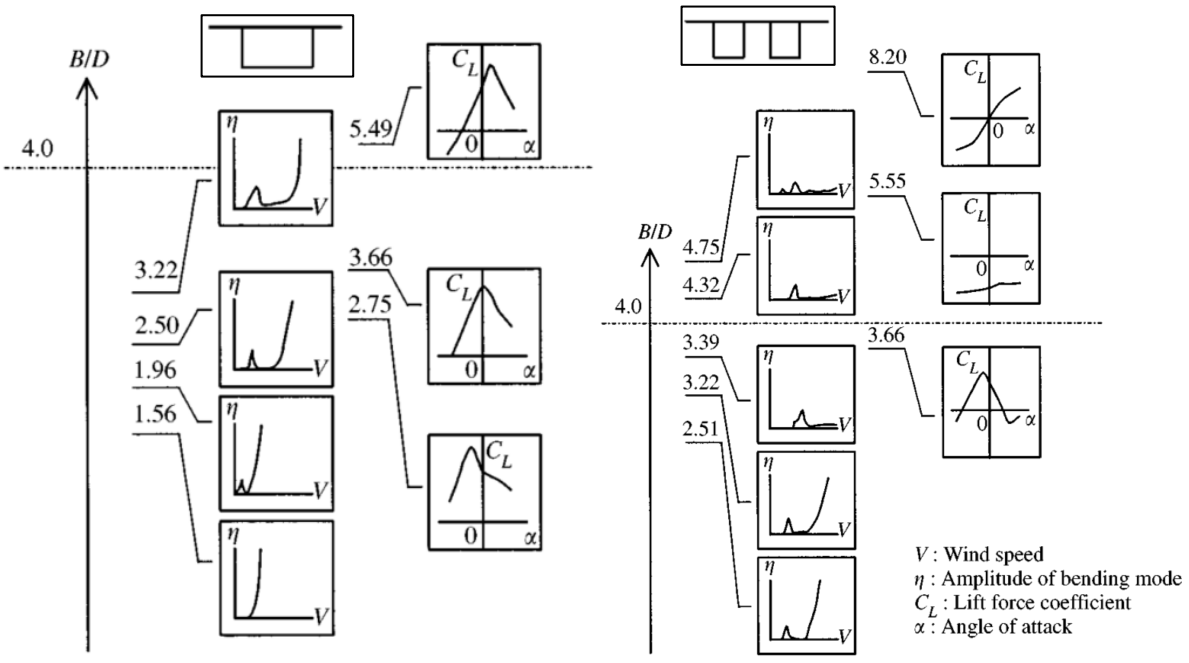

Figure 2.8 Vertical aerodynamic characteristics versus side ratio of one and two box girders (Saito and Sakata, 1999)

2.6 Past research on the effects of wind barriers on vehicle driving stability and aerodynamic performance of bridges

Most long-span bridges are susceptible to the effects of strong winds, which can compromise not only their aerodynamic performance but also the safety and comfort of both

pedestrians and vehicles on the bridges. Such conditions often lead to the implementation of traffic controls, including vehicular restrictions, closures, and speed limits leading to economic losses and traffic disruption. The installation of wind barriers can significantly mitigate these wind-related issues. However, wind barriers can amplify wind loads and increase the risk of aeroelastic instability of bridges.

Many studies have consistently shown that wind barriers can substantially decrease wind velocities, thereby stabilizing vehicles on the bridge. On The Second Severn Bridge, for example, wind barriers reduced gust speeds significantly, approximately 1.4 times lower than at ground level, which alleviated the need for traffic restrictions, but resulted in the increase of the drag force of the bridge by 2.5 times, prompting the use of a more aerodynamically efficient girder design i.e. a streamlined girder (Simiu and Miyata, 2006). In another instance, wind barriers on a bridge deck with parallel box girders (side ratio of 5.8) lowered the lateral forces acting on vehicles from 3.8 to about 0.8 (Chen et al., 2015). A similar strategy involving the selective installation of wind barriers with various porosity ratios on a bridge (side ratio of 3.6) significantly reduced the aerodynamic coefficients for both stationary and moving trains more than two times (M. Wang et al., 2022). It appears that the impact of these barriers on vehicle force coefficients largely depends on their porosity. Increasing the barrier height also proved to enhance vehicular stability on bluff girder bridges with a side ratio of 10.3, compared to shorter barriers (He et al., 2020).

In a detailed numerical analysis conducted in 2019, He examined how different porosity ratios of wind barriers affect streamlined box girders with a side ratio of about 6.7. His findings indicated that the barriers not only shifted the acceleration zone to the top of the wind barrier, effectively blocking the incoming wind and reducing velocity above the girder, but also significantly widened the wake, improving driving safety. However, this also resulted in increased drag force, which could compromise bridge safety. The barriers increased flow separation at the leading edge and accelerated the flow below the lower surfaces, although they did not alter the overall distribution of wind pressure across the streamlined girder (He et al., 2019).

Furthermore, innovative approaches to installing wind barriers have been explored to optimize costs, efficiency, and reduce adverse effects on bridge structures. For instance, Yang recommended an optimal adjustable wind barrier design for the twin box girder section of Xihoumen Bridge, designed to lie down when vehicle traffic is closed at a certain wind speed limit to minimize wind-induced drag when vehicle flow is interrupted by high winds (Yang et al., 2022). Wang suggested the installation of a stepped wind barrier of limited length away from the pylon area, which is known for sudden wind shifts that can destabilize vehicles. Following the installation of these barriers, the increase in wind velocity outside the pylons was effectively diminished, and the transition in wind speeds became increasingly gradual. The effectiveness of the barriers was found to be directly proportional to their length. Nonetheless, it was observed that extending the barriers beyond a certain point did not yield any additional benefits (Wang et al., 2020).

Additionally, various parameters of wind barriers have been explored in recent research. Lou examined how the curvature of wind barriers affects their performance on streamlined box girders with a side ratio of 6.7. Findings indicated that barriers with minimal curvature more effectively reduced aerodynamic forces on trains, yet they simultaneously increased those

forces on the bridge when compared to barriers with greater curvature (Lou et al., 2022). Zhang compared the impact of wind barriers with circular and rectangular openings on the driving stability of vehicles on truss girders with a side ratio of 3.2. His findings highlighted that the shape of the openings had a minor effect on stability relative to factors like height and porosity (Zhang et al., 2021). Lin and Procino found similar results regarding opening types in their studies on the efficiency of wind barriers on single-bluff girders (Lin et al., 2022). Procino additionally noted that wind barriers with a triangle-shaped section facing the wind in a concave manner provided better protection for vehicle driving than those oriented in a convex manner (Procino et al., 2008).

Besides, Telenta analyzed the performance of four wind barriers differing in bar inclinations, ranging from 90 degrees (30% porosity) to 30 degrees relative to the horizontal. The study concluded that reducing the angle of inclination lessened the barriers' effectiveness in mitigating wind, while also altering the airflow patterns behind them (Telenta et al., 2014).

The study of wind barriers to ensure and minimize their effects on the aerodynamic performance of bridges has been a focal point of both experimental and numerical research by numerous scholars. These studies universally suggest that the drag coefficient of bridges increases when wind barriers are implemented, irrespective of the girder shapes or side ratios. However, the impact of these barriers on aeroelastic outcomes remains ambiguous and varies based on the configuration of the bridges and barriers themselves.

Liu conducted experiments on the Vortex-Induced Vibration (VIV) performance of twin-separated parallel girders of streamlined type for railway and highway, with side ratios of 5.5 and 12.1, respectively. His findings indicated that the railway girder was more susceptible to vertical VIV, whereas the highway girder exhibited a greater tendency towards torsional VIV. The installation of wind barriers effectively mitigated VIV amplitudes in both types of girders by significantly reducing the fluctuating wind pressure coefficients, altering correlation coefficients, and diminishing the aerodynamic forces contributing to the overall forces affecting the railway deck. This intervention disrupted the uniform dominant frequency distribution and suppressed the VIV of the railway upstream (Liu et al., 2023). Similarly, Wang observed reduced VIVs in a streamlined girder (side ratio = 9.4) using a wind barrier with 50% porosity. On the other hand, barriers with 0% and 20% porosity ratios exacerbated the VIV amplitudes and decreased the critical wind velocity for torsional flutter (Wang et al., 2022), findings that agree with Gutiérrez's research on a streamlined girder (side ratio = 5.6) and Yang's study on a twin-box girder (Gutiérrez and Longhi, 2014; Yang et al., 2022).

In 2013, Kim reported that wind barriers negatively influenced the aerodynamics of a streamlined girder bridge by increasing wind load and buffeting amplitudes, and by decreasing the critical wind velocity for flutter (Kim and Yarlagadda, 2013). Buljac examined triangle-shaped wind barriers with varied porosity ratios and heights on different girder sections (streamlined, semi-bluff, and bluff) with side ratios of 7.8, 10.9, and 2.7, respectively. These barriers increased the drag force coefficient, particularly as porosity decreased and height increased, notably in the streamlined section. Additionally, the lift force coefficient generally rose in the bluff section, especially with more solid and higher barriers. While the impact on galloping was minimal, torsional flutter was significant in the streamlined section and noticeable in the other two sections, accompanied by a reduction in the critical wind velocity for flutter. In a 2020 study, Buljac further explored the positioning of wind barriers, whether

on the windward, leeward, or both sides of the girders, concluding that the placement significantly affects the aerodynamic force and moment coefficients, without inducing galloping instability. The presence of windward and both-edge barriers produced relatively similar mean flow velocity fields, but the largest variance in flow velocity was observed in the shear layer separating from the top of the windward barrier. The characteristics of this shear layer were pivotal in influencing fluctuations in pressure distribution on the top surfaces of the sections, which critically affected the self-excited lift force and pitch moment, thereby diminishing the torsional flutter stability of the bridge deck sections. The effect of the leeward barrier, however, was comparatively minor (Buljac et al., 2020, 2017a, 2017b).

While numerous studies have explored the effectiveness of wind barriers in reducing wind speeds to enhance driving safety, their impact on the aerodynamic performance of bridges has also been well documented. However, there is a notable gap in research regarding the effects of various wind barrier parameters on both perspectives of driving safety enhancement and the aerodynamic performance of a bridge with varied side-ratio along the girder section. Particularly the changes in the interaction between wind and bridge configuration caused by different side ratios—such as those found in bridges with varying depth girders—affect the overall aerodynamic responses. This lack of comprehensive analysis is particularly significant, as variations in side ratios can lead to pronounced differences in wind flow around the bridge, resulting in distinct aerodynamic responses across different girder profiles.

More specifically, a lack of research on how wind barriers influence the mechanism of vertical vortex-induced vibration (VIV) in a bluff box girder with a common side ratio of 5.0 and its attachment with faring, which is prevalent in modern bridge designs, remains a gap. A deeper understanding of the interaction between wind barriers and VIV mechanisms in these specific girders could provide crucial insights and lead to more informative guidelines for wind barrier design, optimizing aerodynamic performance while reducing the extensive time and costs associated with trial-and-error testing approaches for this kind of girders.

References

Betkier, I., Mitkow, S., Kijek, M., 2019. Analysis of vehicle stability loss due to strong crosswind gusts using web services in the route planning process. AoT 52, 47–56. https://doi.org/10.5604/01.3001.0014.0207

Buljac, A., Kozmar, H., Pospíšil, S., Macháček, M., 2017a. Aerodynamic and aeroelastic characteristics of typical bridge decks equipped with wind barriers at the windward bridge-deck edge. Engineering Structures 137, 310–322. https://doi.org/10.1016/j.engstruct.2017.01.055

Buljac, A., Kozmar, H., Pospíšil, S., Macháček, M., 2017b. Flutter and galloping of cable-supported bridges with porous wind barriers. Journal of Wind Engineering and Industrial Aerodynamics 171, 304–318. https://doi.org/10.1016/j.jweia.2017.10.012

Buljac, A., Kozmar, H., Pospíšil, S., Macháček, M., Kuznetsov, S., 2020. Effects of wind-barrier layout and wind turbulence on aerodynamic stability of cable-supported bridges. J. Bridge Eng. 25, 04020102. https://doi.org/10.1061/(ASCE)BE.1943-5592.0001631

Chen, N., Li, Y., Wang, B., Su, Y., Xiang, H., 2015. Effects of wind barrier on the safety of vehicles driven on bridges. Journal of Wind Engineering and Industrial Aerodynamics 143, 113–127. https://doi.org/10.1016/j.jweia.2015.04.021

Fujii, T., Maeda, T., Ishida, H., Imai, T., Tanemoto, K., Suzuki, M., 1999. Wind-induced accidents of train/vehicles and their measures in Japan. QR of RTRI 40, 50–55. https://doi.org/10.2219/rtriqr.40.50

Fujino, Y., Kimura, K., Tanaka, H., 2012. Wind Resistant Design of Bridges in Japan. Springer Japan, Tokyo. https://doi.org/10.1007/978-4-431-54046-5

Gutiérrez, M.O., Longhi, S.N.F., 2014. Bridge windshield design to avoid aeroelastic phenomena, in: Engineering, Environmental Science.

He, X., Xue, F., Zou, Y., Chen, S., Han, Y., Du, B., Xu, X., Ma, B., 2020. Wind tunnel tests on the aerodynamic characteristics of vehicles on highway bridges. Advances in Structural Engineering 23, 2882–2897. https://doi.org/10.1177/1369433220924791

He, X., Zhou, L., Chen, Z., Jing, H., Zou, Y., Wu, T., 2019. Effect of wind barriers on the flow field and aerodynamic forces of a train–bridge system. Proceedings of the Institution of Mechanical Engineers, Part F: Journal of Rail and Rapid Transit 233, 283–297. https://doi.org/10.1177/0954409718793220

KANEKO, R., KIM, H., KIMURA, K., KATSUCHI, H., FUJINO, Y., n.d. CHARACTERISTICS OF CROSSWIND BASED ON FIELD MEASUREMENT USING A MOVING VEHICLE ON THE TRANS-TOKYO BAY BRIDGE.pdf. Journal of Structural Engineering 27, 207–216.

Kim, H., FUJINO, Y., KATSUCHI, H., SIRINGORINGO, D.M., YAMADA, H., OHKOSHI, S., 2021. Computational fluid dynamics simulation and stability analysis of vehicle on bridge under strong winds. Journal of Japan Society of Civil Engineers, Ser. A1 (Structural Engineering & Earthquake Engineering (SE/EE)) 77, 107–120. https://doi.org/10.2208/jscejseee.77.1_107

Kim, H., Murata, R., Kaneko, R., Kimura, K., Katsuchi, H., 2023. Analysis of Crosswinds on the Box-girder Bridge with Variable Girder Height. Summaries to Technical Papers of Annual Meeting, Japan Association for Wind Engineering 2023, 119. https://doi.org/10.14887/jaweam.2023.0_119

Kim, S., Seyedi, M., Kim, H.-K., 2022. Risk assessment of wind-induced vehicle accidents on long-span bridges using onsite wind and traffic data. J. Struct. Eng. 148, 04022155. https://doi.org/10.1061/(ASCE)ST.1943-541X.0003455

Kim, S.-J., Shim, J.-H., Kim, H.-K., 2020. How wind affects vehicles crossing a double-deck suspension bridge. Journal of Wind Engineering and Industrial Aerodynamics 206, 104329. https://doi.org/10.1016/j.jweia.2020.104329

Kim, Y.H., Yarlagadda, P., 2013. Advanced Technologies in Manufacturing, Engineering and Materials: Trans Tech Publications Ltd. https://doi.org/10.4028/b-RpgE0b

Lin, X., Lin, B., Xia, D., Lin, L., Yuan, Z., 2022. Effects of Wind Barriers on Wind Fields and Vehicle Stability on Bridges. Atmosphere 13, 318. https://doi.org/10.3390/atmos13020318

Liu, L., Zou, Y., He, X., Zhou, X., Cai, C., Yang, J., 2023. Effects of wind barriers on VIV performances of twin separated parallel decks for a long-span rail-cum-road bridge. Journal of Wind Engineering and Industrial Aerodynamics 236, 105367. https://doi.org/10.1016/j.jweia.2023.105367

Lou, P., Tao, W., Cai, C., He, X., Zou, Y., Ai, Y., 2022. Influence of wind barriers with different curvatures on crosswind aerodynamic characteristics of a train-bridge system. Applied Sciences 12, 1747. https://doi.org/10.3390/app12031747

Mashhadi, A., Sohankar, A., Alam, Md.M., 2021. Flow over rectangular cylinder: Effects of cylinder aspect ratio and Reynolds number. International Journal of Mechanical Sciences 195, 106264. https://doi.org/10.1016/j.ijmecsci.2020.106264

Procino, L., Kozmar, H., Bartoli, G., Borsani, A., 2008. Wind barriers on bridges: The effect of wall porosity. Bluff Bodies Aerodynamics & Applications.

Saito, T., Sakata, H., 1999. AERODYNAMIC STABILITY OF LONG-SPAN BOX GIRDER BRIDGES AND ANTI-VIBRATION DESIGN CONSIDERATIONS. Journal of Fluids and Structures 13, 999–1016. https://doi.org/10.1006/jfls.1999.0238

Simiu, E., Miyata, T., 2006. Design of Buildings and Bridges for Wind: A Practical Guide for ASCE-7 Standard Users and Designers of Special Structures, 1. st. ed. Wiley, New York.

Simiu, E., Yeo, D., 2019. Wind Effects on Structures: Modern Structural Design for Wind, 1st ed. Wiley. https://doi.org/10.1002/9781119375890

Telenta, M., Duhovnik, J., Kosel, F., Šajn, V., 2014. Numerical and experimental study of the flow through a geometrically accurate porous wind barrier model. Journal of Wind Engineering and Industrial Aerodynamics 124, 99–108. https://doi.org/10.1016/j.jweia.2013.11.010

Wang, D., Zhang, Y., Sun, M., Chen, A., 2020. Characteristics of the wind environment above bridge deck near the pylon zone and wind barrier arrangement criteria. Applied Sciences 10, 1437. https://doi.org/10.3390/app10041437

Wang, J., Sato, M., Katsuchi, H., Tamura, H., 2022. Experimental investigation on effects of wind barrier on aerodynamic stability of bridge and vehicle on bridge. Wind Engineering Research Papers No. 27.

Wang, M., Wang, Z., Qiu, X., Li, Xingxing, Li, Xiaozhen, 2022. Windproof performance of wind barrier on the aerodynamic characteristics of high-speed train running on a simple supported bridge. Journal of Wind Engineering and Industrial Aerodynamics 223, 104950. https://doi.org/10.1016/j.jweia.2022.104950

Yang, Y., Zhang, J., Cao, F., Ge, Y., Zhao, L., 2022. Evaluation and improvement of wind environment and vehicle safety on long-span bridge deck under strong crosswind. Journal of Wind Engineering and Industrial Aerodynamics 228, 105089. https://doi.org/10.1016/j.jweia.2022.105089

Zhang, J., Zhang, M., Huang, B., Li, Y., Yu, J., Jiang, F., 2021. Wind tunnel test on local wind field around the bridge tower of a truss girder. Advances in Civil Engineering 2021, 1–13. https://doi.org/10.1155/2021/8867668

Zhang, Q., Su, C., Wang, Y., 2020. Numerical investigation on aerodynamic performance and stability of a sedan under wind–bridge–tunnel road condition. Alexandria Engineering Journal 59, 3963–3980. https://doi.org/10.1016/j.aej.2020.07.004

CHAPTER 3
Methodology

3.1 Introduction

This chapter introduces the wind tunnel setup utilized for the research, outlining its specifications and operational parameters. It details the wind tunnel experiments designed for Objective 1 to investigate the effects of various wind barriers on the aerodynamic performance and wind flow field of bluff box girders with side ratios of 3.44 and 4.98. These experiments include an aerodynamic force coefficient measurement on a stationary sectional model, a two-degree-of-freedom free vibration test, and a wind velocity measurement. Subsequently, this chapter describes additional wind tunnel tests aimed at Objective 2, which focuses on elucidating the mechanisms of vertical vortex-induced vibration (VIV) in a bluff box girder with a side ratio of 5.00 and its attachment with faring. These tests encompass a one-degree-of-freedom free vibration test, a pressure measurement, and wind flow visualization using Particle Image Velocimetry (PIV) analysis.

3.2 Outline of wind tunnel

All tests, except for the static pressure distribution measurement, were conducted in the closed-circuit wind tunnel at Yokohama National University, which can achieve wind speeds of up to 40 m/s. This wind tunnel has a cross-sectional area of 1.8 m by 1.8 m, as depicted in Figure 3.1. In contrast, the static pressure distribution measurement was carried out in an open-circuit Eiffel-type wind tunnel at the same university as shown in Figure 3.2, which features a working section measuring 1.3 m by 1.3 m and supports a maximum wind speed of 20 m/s. All sectional models and wind barrier models used in the tests were scaled to 1:100. The experiments were conducted under conditions of smooth flow, with blockage ratios less than 5% without wind barriers and 7% with wind barriers.

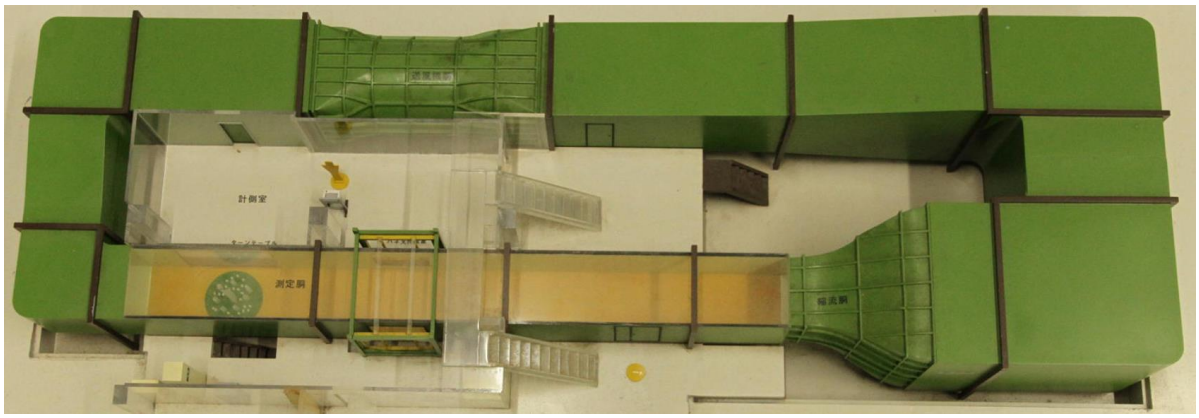

Figure 3.1 Closed-circuit wind tunnel

Figure 3.2 Open-circuit wind tunnel

3.3 Aerodynamic force coefficient measurement

The aerodynamic force coefficients of a stationary sectional model were measured under uniform wind flow conditions at speeds of 4 m/s and 7 m/s to evaluate the influence of the Reynolds number. A load cell, rigidly attached to the model, was supported by a supporting system to ensure stability and precision in the measurement.

The force measurements were conducted across a range of angles of attack from -10° to +10°at 1° intervals in which the nose-up direction is positive. The data captured by the load cell were then processed through a low pass filter to eliminate high-frequency noise, ensuring the clarity and accuracy of the measurements. Subsequently, the filtered data were digitized using an A/D (Analog to Digital) adapter that sampled at a frequency of 1,000 Hz.

Figure 3.3 illustrates the sectional model along with the directions of the aerodynamic force coefficients, including drag (C_D), lift (C_L), and moment (C_M). These coefficients are calculated using equation 3.1 where F_D, F_L, and F_M represent the drag, lift, and moment forces, respectively. The symbols ρ denotes air density, U represents the wind velocity, and L, D and B are the length, depth, and width of the model, respectively.

$$C_D = \frac{F_D}{0.5\rho U^2 DL}$$

$$C_L = \frac{F_L}{0.5\rho U^2 BL} \qquad \text{Eq. 3.1}$$

$$C_M = \frac{F_M}{0.5\rho U^2 B^2 L}$$

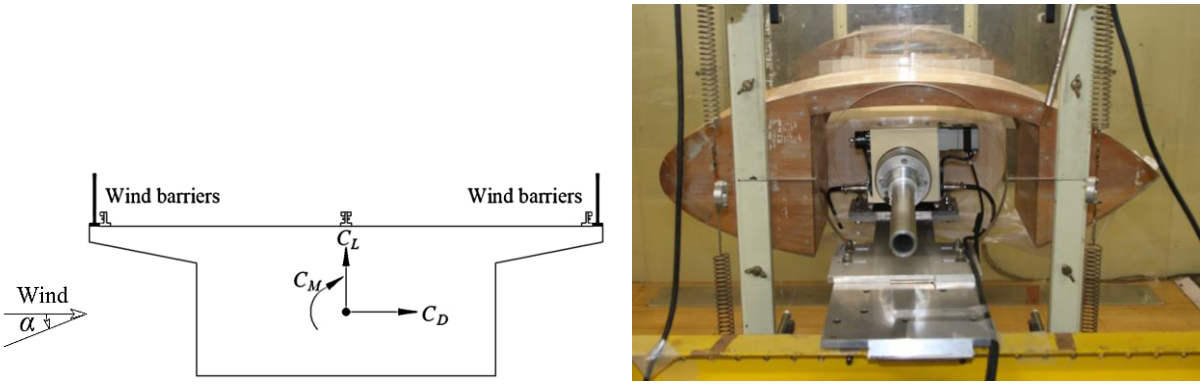

(a) Aerodynamic coefficient direction (b) Load cell and supporting system

Figure 3.3 Details of aerodynamic force coefficient measurement

Figure 3.4 A sectional model in a wind tunnel for aerodynamic force coefficient measurement

3.4 Free vibration tests

A series of free vibration tests were conducted to assess the impact of wind barriers with varying parameters on the aerodynamic responses of the sectional models. These tests involved exposing the models to uniform wind flow at angles of attack α = 0° and +3° across a range of wind speeds. The setup was designed to control vertical damping to a constant value of 0.03 using an electromagnetic damper, while damping in torsional mode was maintained at low values to facilitate the observation of the vibration in this mode. The amplitudes of the vibrations caused by the fluid-structure interaction were then accurately measured using laser displacement meters.

The support structure is illustrated in Figure 3.6, the models were horizontally supported by two arms attached to the model's endplates. Four coil springs provided support for each arm outside the wind tunnel. This support system could enable free vibration tests in both one-degree and two-degree of freedom. Restraint in horizontal and vertical displacements was

achieved by piano wires, whereas torsional displacement was controlled by rigidly connecting the model's axis to a support bar via the springs.

Two laser displacement meters, which are non-contact measuring devices, were employed to capture the distance between the device and the model's surface. These meters measured changes in this distance, which correspond to the displacements caused by wind-induced vibrations. The collected data were recorded at a frequency of 1,000 Hz, allowing for subsequent digital analysis including calculations of mass (m), moment of inertia (I), and structural damping (represented by logarithmic decrement, δ) from decay vibration for Scruton number (Sc) calculation, as in equation 2.7, which is an important non-dimensional parameter affecting the aerodynamic responses of bodies.

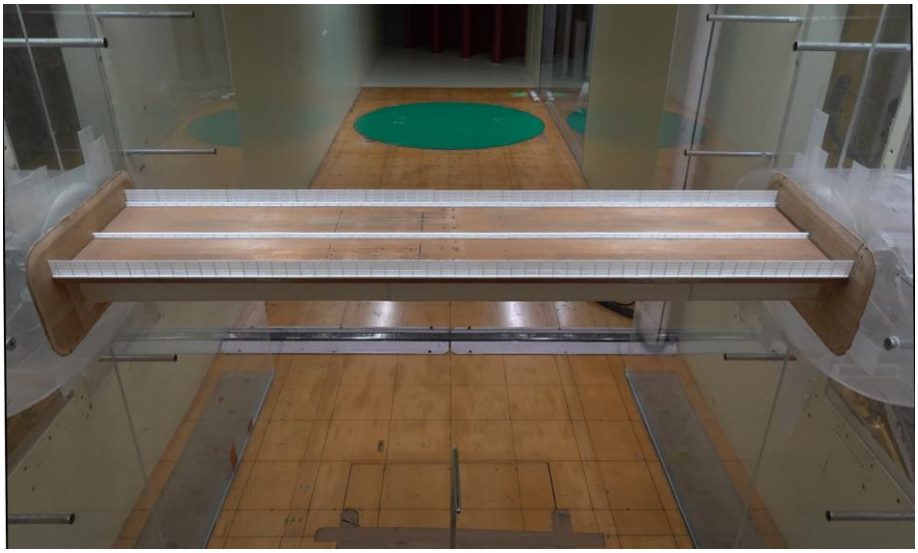

Figure 3.5 A sectional model with wind barriers for free vibration test

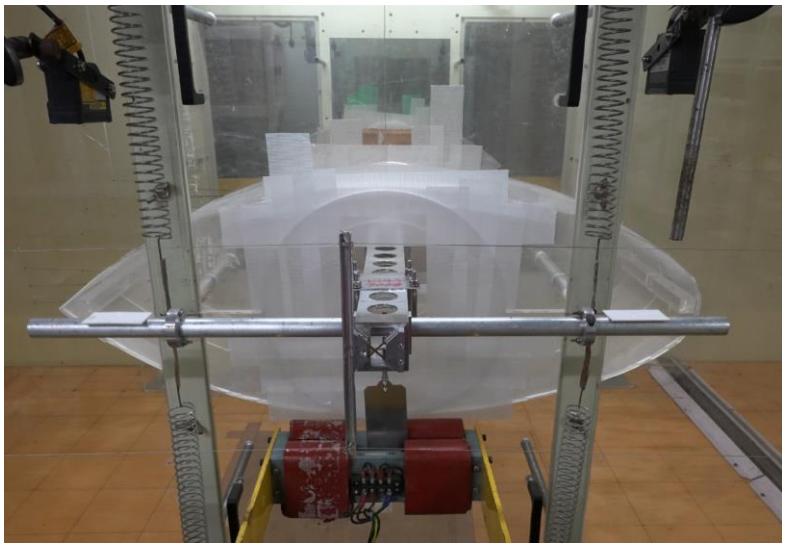

Figure 3.6 Support system for free vibration test

3.5 Wind velocity measurement

The effectiveness of wind barriers in enhancing vehicle driving stability was quantified through the reduction of mean and maximum wind speed above the sectional models, which was measured using an "X" hotwire anemometer as in Figure 3.7. This anemometer utilizes two crossed wires to capture both the magnitude and direction of the wind flow, which are maintained at a constant temperature. As air passes over the wires, they cool down, and this cooling rate is directly proportional to the airflow speed. The anemometer determines the wind speed by measuring the electrical resistance of the wires, which varies with temperature.

Wind measurements were conducted at an angle of attack $\alpha = 0°$ with uniform wind speeds of 4 m/s. Data acquisition lasted for 30 seconds at each measurement point, with a sampling frequency of 1,000 Hz. The specific measurement locations are illustrated in Figure 3.8. These points are strategically placed along vertical lines extending to a height of 12 m in real scale, encompassing the height of all vehicles to ensure their driving stability on bridges and capturing the separated shear layers above the sectional models to study the wind flow field above them. The measurement points are precisely aligned with the center of the traffic lanes, the handrails, and the median of the sectional models.

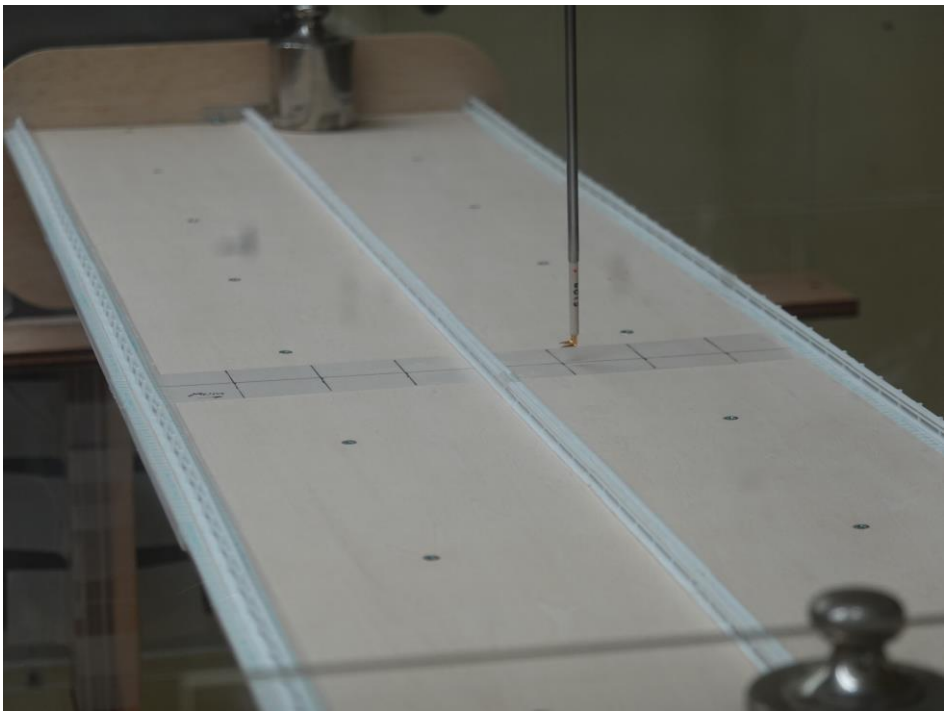

Figure 3.7 A sectional model with “X” hotwire anemometer

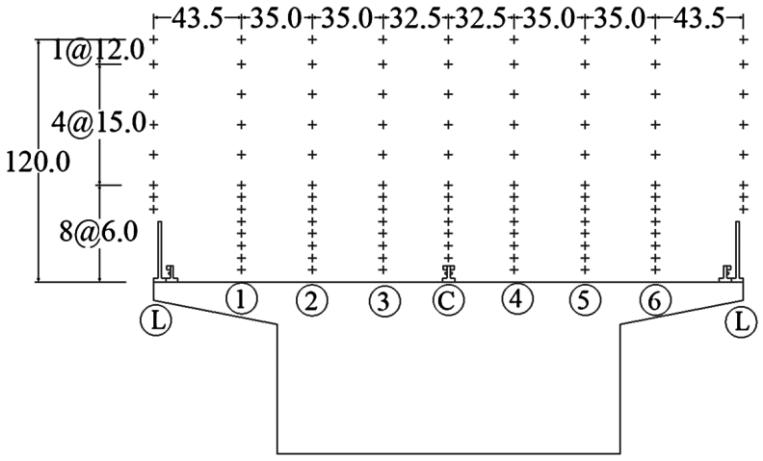

Figure 3.8 Wind measurement points (unit: mm; scale: 1/100)

Notes: 1) L is the edges and C is the center of the sectional models.

2) ① to ⑥ are the center of the traffic lanes.

3) The sectional models used in wind measurement had almost similar widths.

3.6 Pressure measurement on the stationary sectional model

This experiment was conducted at a uniform wind speed of 7 m/s with an angle of attack α = 0° to explore the effects of wind barriers on pressure distribution around the bluff box girder and its attachment to the fairing. The reference pressure, which is the sum of static and dynamic pressures in the incoming wind flow, was measured using a Pitot tube.

As depicted in Figure 3.9, the bluff girder model is equipped with 32 pressure taps distributed over one section. These taps are more closely spaced near the edges of the model on both the top and bottom surfaces to accurately capture flow separation, whereas the removable fairings conclude 6 pressure taps. There are five such sections along the length of the model, named Section 1 through Section 5, where Section 3 was positioned at the center of the model as in Figure 3.10, to help verify the accuracy of the pressure distribution and assess the influence of the wind tunnel's walls on the pressure measurement. More specifically, the pressure distribution of sections 1 and 2, sections 1 and 3, and sections 1 and 4 were simultaneously measured to clarify how the wind barriers affect the flow structure along the spanwise direction *(Δz/D*) of the girder, through the spanwise correlation coefficient, which contributes to the VIV.

The mean surface pressure coefficient is defined in equation 3.2a, while the fluctuating pressure coefficient is defined in equation 3.2b.

$$\overline{C_P}(n) = \bar{P}(n)/(0.5\rho U^2)$$

$$\widetilde{C_P}(n) = \tilde{P}(n)/(0.5\rho U^2) \qquad \text{Eq. 3.2 a,b}$$

Where $\bar{P}(n)$ and $\tilde{P}(n)$ are the mean and fluctuating surface pressure measured at the pressure taps *n*, respectively. *U* is mean wind speed and ρ is air density.

The spanwise correlation coefficient was calculated from equation 3.3.

$$R_{C_i}(\Delta z/D) = cov[C_i(\Delta z/D)]/var[C_i] \quad \text{Eq. 3.3}$$

Where R_{C_i} is a spanwise correlation coefficient, C_i is sectional fluctuating lift force calculated from the integration of fluctuating pressure on the top and bottom sides of the girder, $\Delta z/D$ is the relative distance in spanwise direction from section 1 normalized by the depth of the girder, cov is covariance and var is variance.

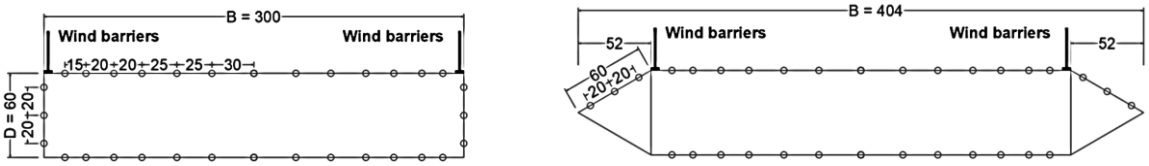

Figure 3.9 Sectional models with pressure tap points (unit: mm; scale: 1/100)

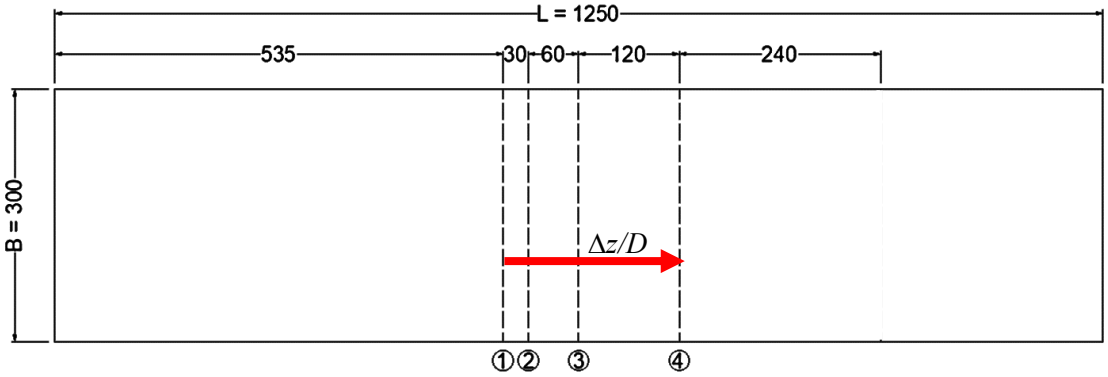

Figure 3.10 Pressure measurement sections (unit: mm; scale: 1/100)

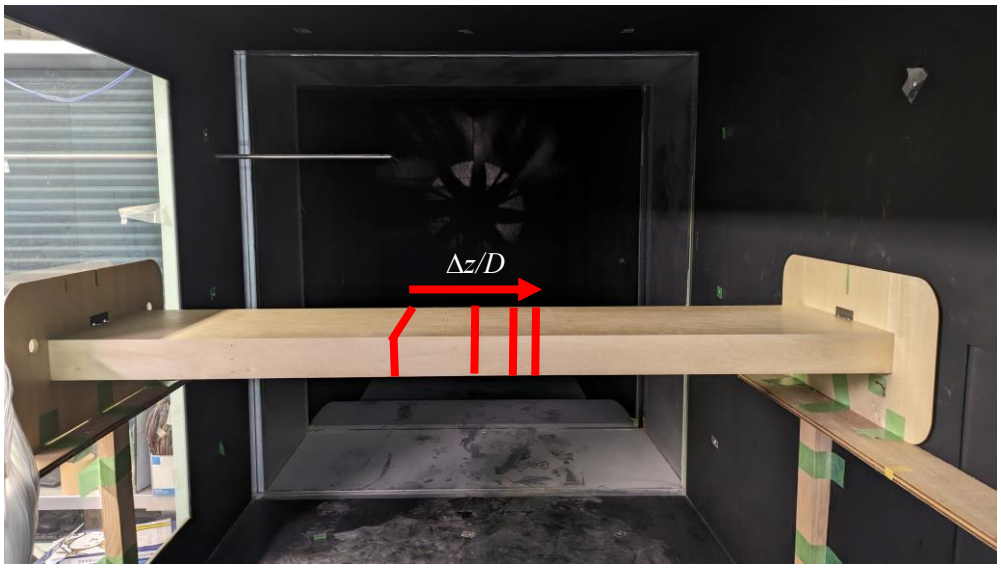

Figure 3.11 Pressure measurement in open-circuit wind tunnel

3.7 Flow visualization

In this experiment, PIV was utilized to visualize and quantify wind flow characteristics—such as velocity, vorticity, and turbulence intensity—around the stationary bluff girder and its attachment to the fairing, influenced by wind barriers. The test was conducted at a uniform wind speed of 2 m/s at an angle of attack $\alpha = 0°$.

Tracer particles were introduced into the flow using a smoke generator, a common method for seeding in PIV experiments to ensure even distribution and optimal visibility of the flow patterns. A laser sheet, generated from a laser positioned at the top of the wind tunnel, illuminated the top plane of the models. In the case of capturing the flow on the lower side of the models, wind barriers were moved to be installed at the bottom side of the models. The test setup is shown in Figure 3.12.

Image capture was performed using a high-speed K5 camera, which recorded the scattered light from the tracer particles. The camera was set to capture images at a resolution of 640 x 480 pixels, at a high frame rate of 2,000 frames per second (fps), ensuring detailed temporal resolution of the rapidly changing flow. A total of 27,000 frames were recorded with a shutter speed of 1/2,000 of a second, allowing for precise measurement of particle displacement between frames. The recorded data was analyzed using the Katokoken(R) FlowExpert Version 1.3.3.1 software for a period of image pairs of 0.0005 s, grid interval of 11.05 pixels, and interrogation size of 25 pixels.

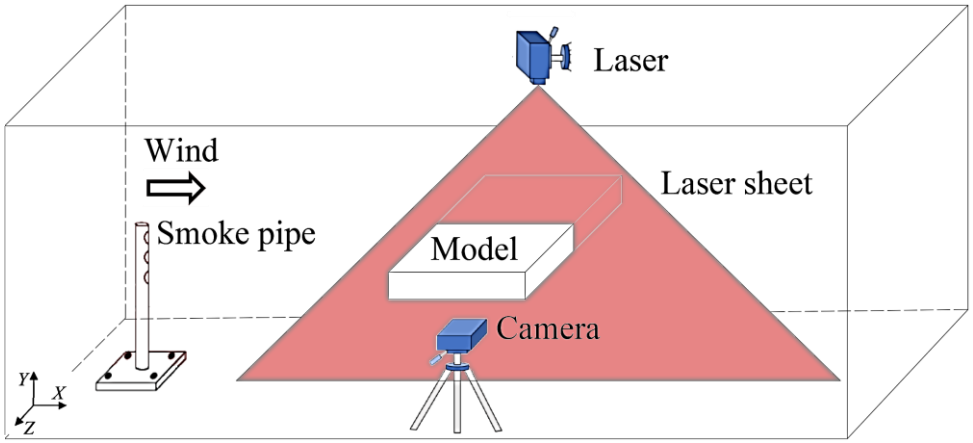

Figure 3.12 Test setup of flow visualization

CHAPTER 4

Effects of wind barriers on the aerodynamic performance and wind flow field of bluff box girders with different side ratios

4.1 Introduction

This chapter explores the influence of wind barriers with varying parameters on the aerodynamic performance and wind flow field of bluff box girders, particularly focusing on two different side ratios of 3.44 (thick girder) and 4.98 (thin girder). The discussion commences with an in-depth overview of the sectional models utilized in wind tunnel tests, accompanied by a detailed selection of various parameters for the wind barriers, as outlined in Section 4.2.

The investigation into aerodynamic coefficients—drag, lift, and moment coefficients—sheds light on the effects of wind barriers on the stationary thick girder. Section 4.3 explores these dynamics, evaluating the potential for galloping under steady-quasi-steady conditions due to the girder's smaller side ratio. This section specifically highlights how the increased drag force on the girder, caused by an expanded windward surface area due to wind barriers, impacts its aerodynamic performance.

Section 4.4 then delves into the aerodynamic responses of both girders in the vertical and torsional directions at angles of attack of 0° and +3°. This analysis examines how the girders' unique configurations—characterized by different side ratios—and the application of various wind barrier designs affect their aerodynamic interaction and stability. This section comprehensively discusses how these barriers might inadvertently cause destabilization and outlines effective countermeasures to stabilize vibration.

Section 4.5 focuses on the wind flow field above both girders, highlighting how wind barriers modify flow dynamics. This section provides a thorough examination of wind vector distribution, turbulence intensity, and wind speed profiles. The implications of these modifications are considered in terms of their impact on the aerodynamic vibration of the girders and on enhancing vehicle driving safety.

Finally, Section 4.6 gives the concluding remarks on the effect of parameters of wind barriers on the aerodynamic performance of both girders from the perspectives of the aerodynamic stability of the bridge and the wind flow field affecting the driving safety of the vehicles with useful suggestions for design and implementation of a wind barrier for these girders.

4.2 Sectional and wind barrier models

4.2.1 Sectional models

For wind tunnel experimentation, sectional models of a bluff box girder with a scale of 1:100 and a length of 1,250 mm, were employed. These models represent various segments along the

length of a bridge with varying girder depths characterized by side ratios (defined as *B/D*, where *B* is the width and *D* is the depth of the girder) such as an extension section of the Trans-Tokyo Bridge.

The first model represented a section located at the central span of the bridge with the minimum depth at point *L*/2 (where *L* is the maximum span), while another model depicted a section closer to the girder's support at point *L*/8.6. These two models have side ratios of 3.44 (thick girder) and 4.98 (thin girder), respectively as shown in Figure 4.1. The selection was based on both perspectives of the representative of the aerodynamic performance of the bridge as reported by (Fujino and Yoshida, 2002), and the driving safety of vehicles as detailed in Section 2.1.

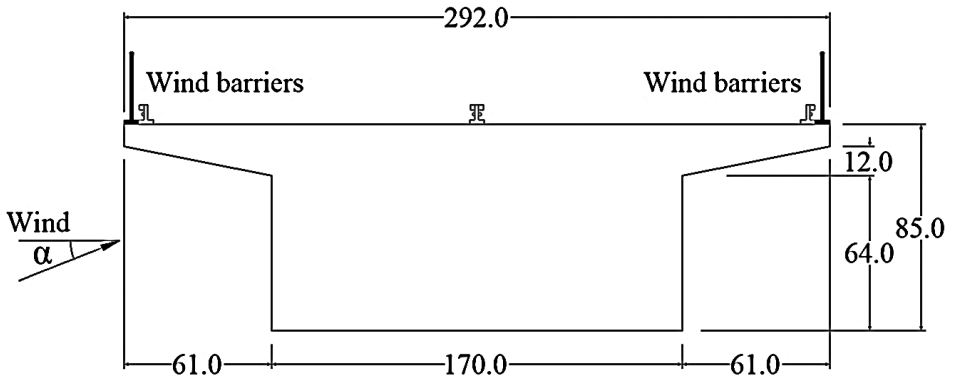

(a) Thick girder (*B/D* = 3.44)

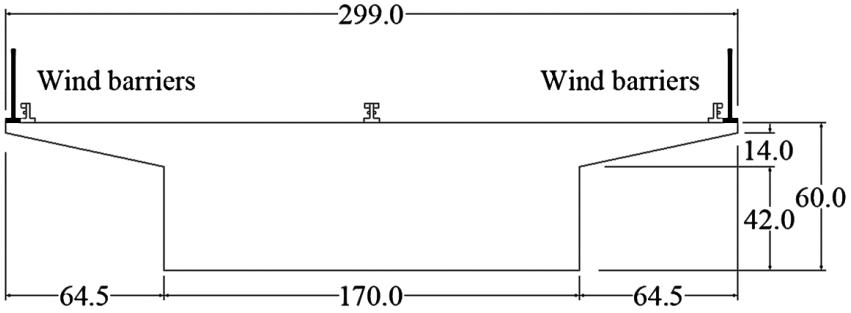

(b) Thin girder (*B/D* = 4.98)

Figure 4.1 Sectional models (unit: mm; scale: 1/100)

4.2.2 Wind barrier models

As discussed in Section 2.6, the impact of wind barriers on the aerodynamic stability of bridges and vehicles strongly depends on their configurations. Various parameters of wind barriers with a height of 30 mm (in a wind tunnel scale of 1/100), as shown in Figure 4.2, were therefore investigated. Initially, the hole schemes in vertical (V) and horizontal (H) directions were established. Then, three porosity ratios—defined by the ratio of the open area to the total area— of 25%, 50%, and 70% were further examined for optimal benefits to both the aerodynamic performance of the bridge and vehicle safety, the horizontal hole schemes with porosity ratios of 25% and 50% were selected. Subsequently, methods for installing wind

barriers on bridges were evaluated by experimenting with partial placement of barriers above the handrails (P), as opposed to full installation alongside them.

The aerodynamic response tests indicated that wind barriers considerably increased the vertical vortex-induced vibration (VIV) amplitude for both girders. To mitigate this effect, new strategies were proposed for a wind barrier with a horizontal hole scheme and a porosity ratio of 50% (50-H-3.0m, standard wind barrier) to stabilize the vibrations by varying the spacing of the horizontal bar members to have larger hole spacing at the bottom and smaller at the top (DS). Additionally, combining wind barriers with single and double flaps (+F and +DF, respectively) was explored as another method to enhance aerodynamic stability. However, most proposed countermeasures failed to stabilize the VIV in the thin girder. Hence, the height of the standard wind barrier was reduced to 2.5 m (50-H-2.5m) with the measurement of wind velocity as well.

- Hole schemes and porosity ratios

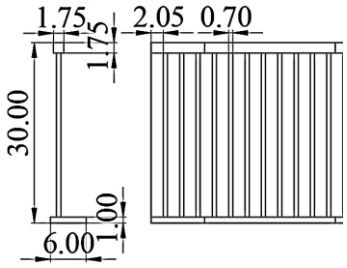

(a) 25-V

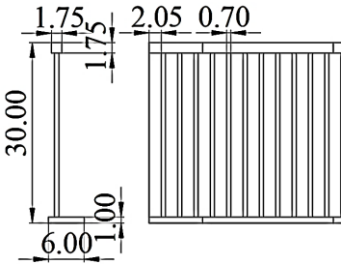

(b) 50-V

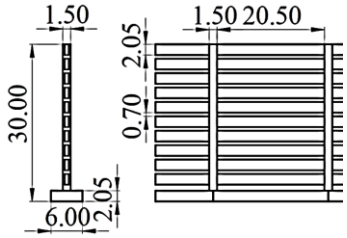

(c) 25-H

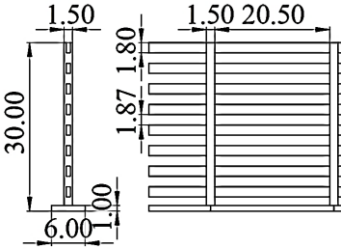

(d) 50-H-3.0m

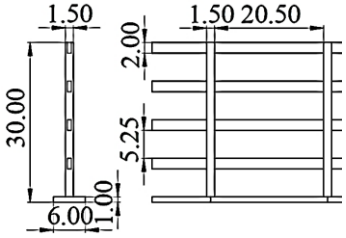

(e) 70-H

- Installation method

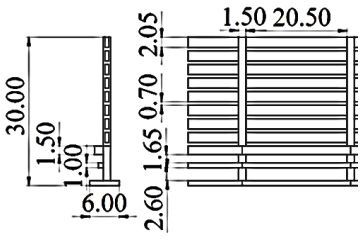

(f) 25-H-P

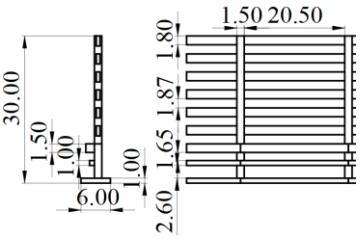

(g) 50-H-P

- VIV countermeasures

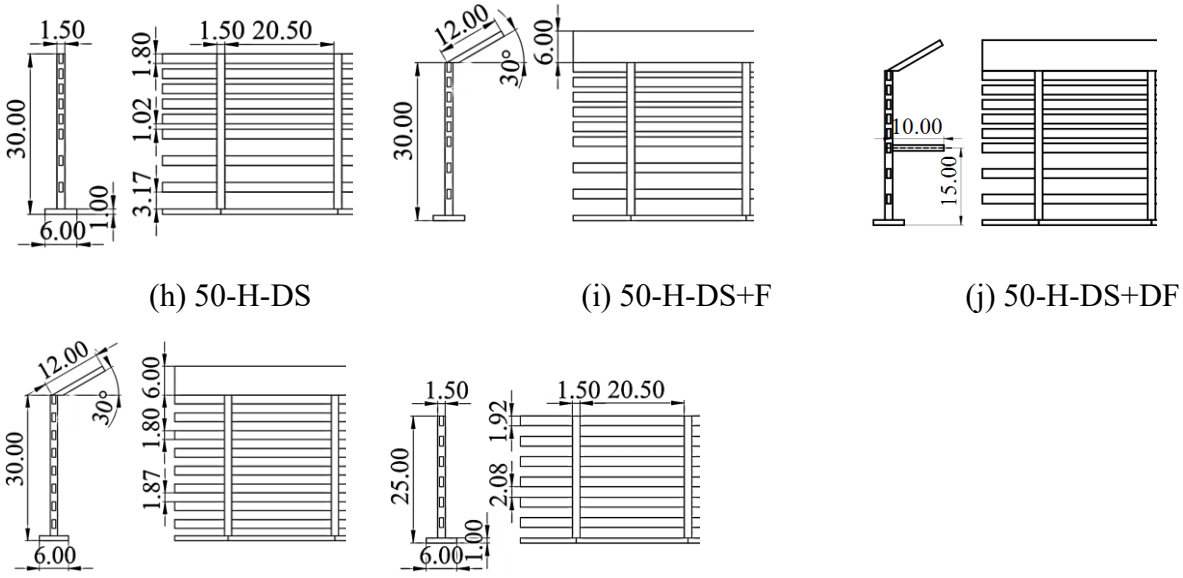

(h) 50-H-DS (i) 50-H-DS+F (j) 50-H-DS+DF

(k) 50-H+F (l) 50-H-2.5m

Figure 4.2 Details of wind barrier models (unit: mm; scale: 1/100)

Notes: 1) 25, 50, and 70 are porosity ratios.

2) 3.0m and 2.5m are heights.

3) V and H are vertical and horizontal hole schemes.

4) DS is the different spacing of the horizontal bars.

5) +F and +DF are the combinations of wind barriers with single and double flaps.

6) P is a partial wind barrier installed above the handrails.

4.3 Aerodynamic force coefficients of the thick girder

This section focuses on the impact of wind barriers on the aerodynamic force coefficients of the thick girder, which is particularly susceptible to galloping due to its smaller side ratio (B/D = 3.44). This susceptibility contrasts with the thin girder, which, with a side ratio greater than 4, is not prone to galloping as elaborated in Section 2.3.2. Consequently, we analyze the lift coefficient of the thick girder to assess the potential for galloping, using the following quasi-steady theory equation:

$$\left(\frac{dC_L}{d\alpha} + C_D\right)_{\alpha=0} < 0 \qquad \text{Eq. 4.1}$$

It is important to note that the application of this quasi-steady theory, which pertains to self-excited forces on a stationary body, is primarily relevant for non-reattachment flow types. This condition generally occurs in bridge girders with side ratios B/D < 2 and in contexts of relatively high reduced velocities, as noted by Simiu and Miyata (2006) and Simiu and Yeo (2019) (Simiu and Miyata, 2006; Simiu and Yeo, 2019).

Additionally, this analysis aims to validate concerns from numerous studies indicating that wind barriers can significantly increase drag forces on bridges as discussed in Section 2.6. These increased forces often lead to adverse effects on bridge stability and integrity, such as increased structural stress and deformation.

The measurement and calculation of these force coefficients including drag (C_D), lift (C_L) and moment (C_M) coefficients against angles of attack are detailed in Section 3.3.

Initially, the study evaluates the influence of wind barriers with different hole orientations—horizontal and vertical—using porosity ratios of 25% and 50% (25-H and 25-V; 50-H and 50-V, respectively). Following this, we assess the impact of completely installing wind barriers adjacent to the handrails versus partially installing them above the handrails (25-H and 25-H-P; 50-H and 50-H-P). The analysis concludes with an examination of various countermeasures, including different spacings of wind barriers (50-H-DS) and their combinations with single and double flaps (50-H-DS+F and +DF).

4.3.1 Effects of hole schemes and porosity ratios

The results presented in Figure 4.3 (a) demonstrate that the bare deck case (BD of 3.44) exhibits the lowest drag coefficient, suggesting minimal resistance to wind loads. When equipped with 25% porosity wind barriers, the drag coefficient is consistently higher across all angles of attack compared to both the bare deck and the 50% porosity barriers. This increase is particularly noticeable around $\alpha = 0°$, where the drag peaks substantially higher than in the bare deck, with an average relative increase of about 1.4 times that of the bare deck. The 25% porosity barriers, allowing limited airflow through, create significant blockage and consequently higher aerodynamic resistance due to the restricted open area relative to the closed area.

The 50% porosity barriers show drag coefficients that lie between those of the bare deck and the 25% porosity barriers, with an average relative increase of about 1.3 times that of the bare deck. This intermediate performance suggests that while the drag is still higher than in the bare deck, the increased open area of the 50% porosity barriers somewhat mitigates the increase in drag. This indicates a balance between barrier permeability and structural blockage.

Figure 4.3 (b) reveals that between $-10° < \alpha < -4°$, the lift coefficients for wind barriers are higher than for the bare deck, particularly for the 25% porosity barriers. Beyond $\alpha = -4°$, the wind barriers substantially reduce lift, with the lowest coefficients observed in the 25% porosity case. The peak lift coefficient for the bare deck exceeds 0.8 at $\alpha = 1°$—the highest among all cases—before decreasing with larger angles of attack. For the wind barriers, the peak lift is not only lower but also broader, centering around 0.5, with reductions in lift spanning nearly the entire tested range.

The negative gradient in the lift coefficient of all cases, particularly steep in the bare deck, indicates a potential for aerodynamic instabilities such as galloping. Figure 4.3 (d), however, suggests that galloping does not occur in any case, likely due to the significant drag forces and the relatively shallow gradient of the lift curve introduced by the wind barriers.

Figure 4.3 (c) shows that the moment coefficient for the bare deck increases up to $\alpha = -10°$ but then declines gradually from $\alpha = -1°$, peaking at about 0.25. In contrast, the moment

coefficients for all wind barrier cases remain relatively stable, ranging from about 0.15 to 0.22 across all angles of attack.

Furthermore, the trends of the force coefficients for wind barriers with the same hole scheme are similar, with only minor variations, suggesting that the hole scheme's impact on force coefficients is minimal.

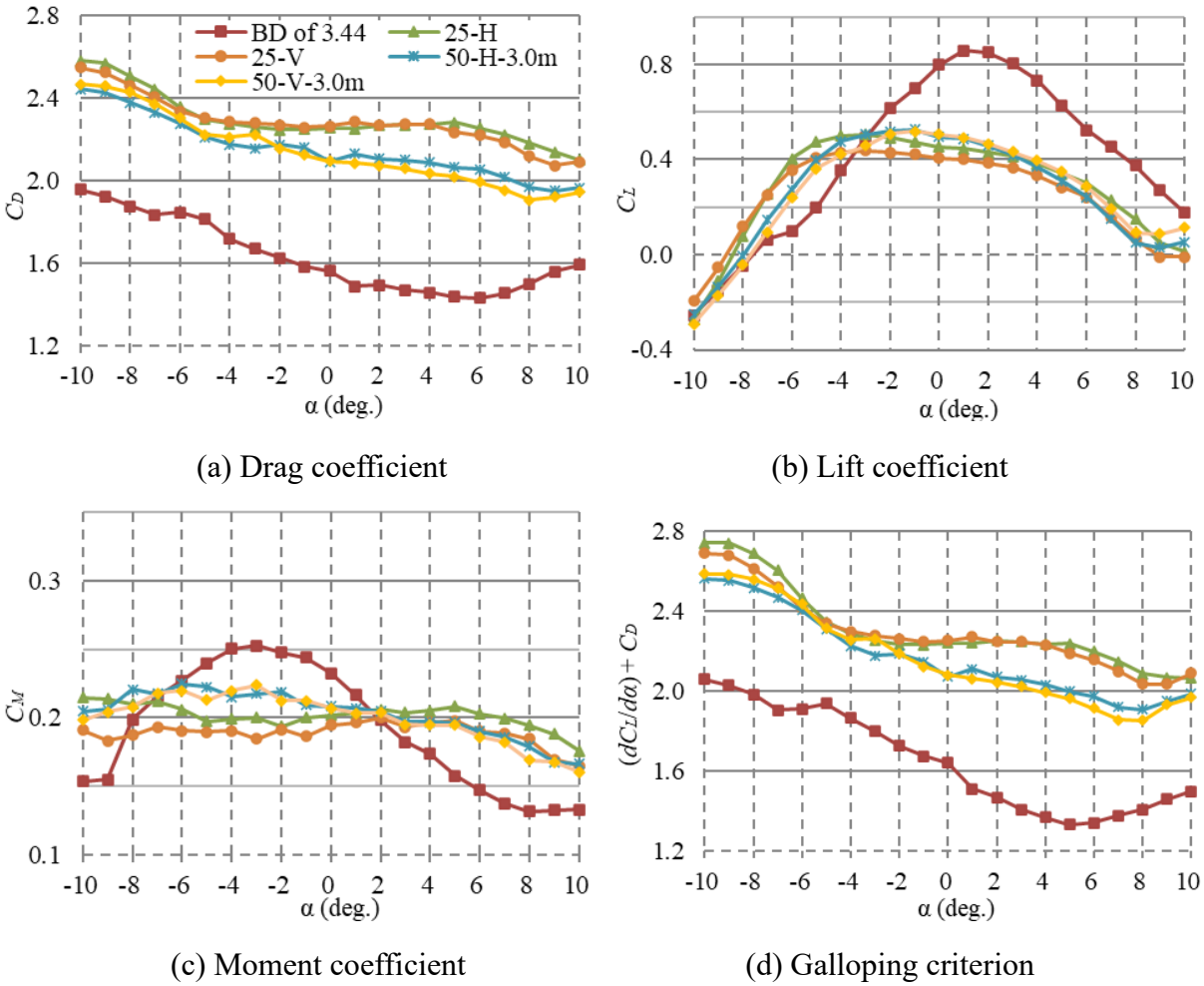

(a) Drag coefficient

(b) Lift coefficient

(c) Moment coefficient

(d) Galloping criterion

Figure 4.3 Aerodynamic force coefficients and galloping criterion of thick girder with different hole scheme wind barriers

4.3.2 Effects of installation method

This section mainly discusses the effect of installation method on the aerodynamic coefficients since the changes in the bare deck and porosity ratios are detailed in section 4.3.1. In Figure 4.4 (a), the partial installation of a 25% wind barrier (25-H-P) shows a slightly higher drag coefficient below $\alpha = -2°$, but as the angle increases, the drag coefficient is lower compared to the full installation (25-H). For the 50% porosity case, the partial installation (50-H-P) exhibits a higher drag coefficient across almost all angles of attack compared to the full barrier (50-H-3.0m), though the difference is minimal.

Conversely, Figure 4.4 (b) shows that the lift coefficient for the 25% porosity full wind barrier (25-H) is higher under α = -3°, while it is higher when the angle increases as compared to the partial installation (25-H-P). For the 50% porosity cases, the full wind barrier (50-H) consistently has a relatively higher lift coefficient. Interestingly, Figure 4.4 (d) implies that no galloping will occur despite these variations. While the installation method appears to have a minor effect on the drag and lift coefficients, it significantly influences the moment coefficient, as shown in Figure 4.4 (c). The partial installation increases the moment coefficient about 1.3 times at α = -5° for the 25% porosity case and about 1.1 times at α = 0° for the 50% porosity case.

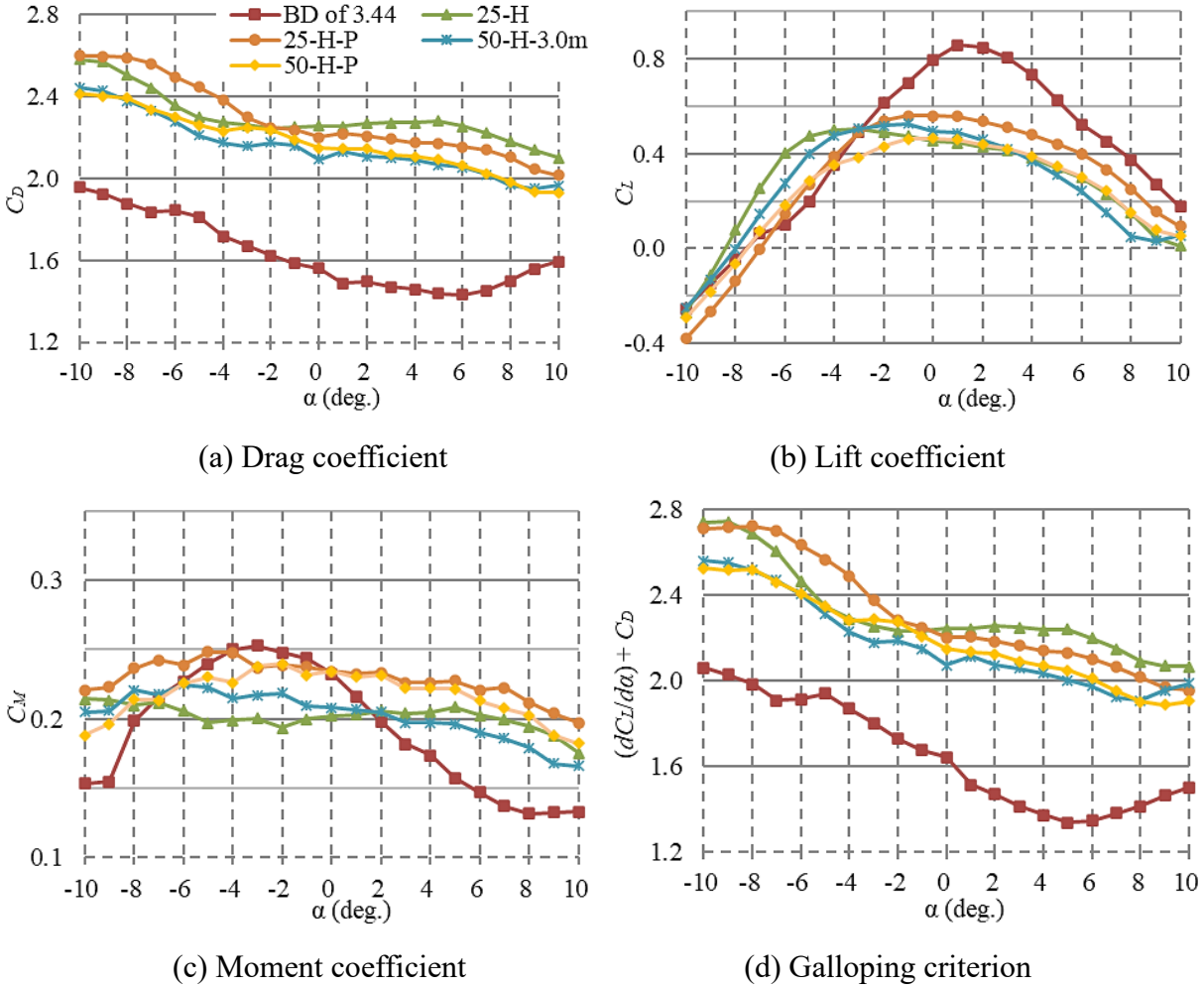

(a) Drag coefficient

(b) Lift coefficient

(c) Moment coefficient

(d) Galloping criterion

Figure 4.4 Aerodynamic force coefficients and galloping criterion of thick girder with installation method of wind barriers

4.3.3 Effects of countermeasures

This section examines how countermeasures designed to stabilize vertical VIV, such as different spacing in wind barrier and combinations with single and double flaps (50-H-DS, +F, and +DF), influence the aerodynamic force coefficients of the thick girder. Figure 4.5 (a) reveals that the different spacing wind barrier exhibits a similar trend to the standard wind

barrier (50-H-3.0m), underscoring that porosity primarily drives the impact on the drag force rather than modifications to the horizontal member bar arrangement, which appears to have minimal effect. The addition of flaps, which increases the windward area resulting in a larger load on the bridge girder, significantly escalates the drag coefficient, increasing it by approximately 1.4 times and 1.1 times on average across all angles of attack compared to the bare deck and standard wind barrier, respectively. Nonetheless, the overall trend of drag coefficient variation with angle of attack remains consistent with other wind barrier cases.

In Figure 4.5 (b), below α = -2°, the lift coefficients across all cases do not show significant variation. However, the standard wind barrier case exhibits the highest lift, with the combination of a double flap yielding the lowest. As the angle of attack increases, the lift coefficient for the case with flaps positions itself between those of the bare deck and standard wind barrier case. This positioning reflects wider and shallower changes in the lift gradient, leading to the largest positive values of the galloping criteria as in Figure 4.5 (d).

Moreover, the countermeasures lead to a notable increase in the moment coefficient across almost all angles of attack. The different spacing wind barrier shows an average increase in the moment coefficient of about 1.1 times compared to the standard wind barrier, while the combinations with flaps exhibit an increase of about 1.4 times, with the double flap combination showing the most significant rise.

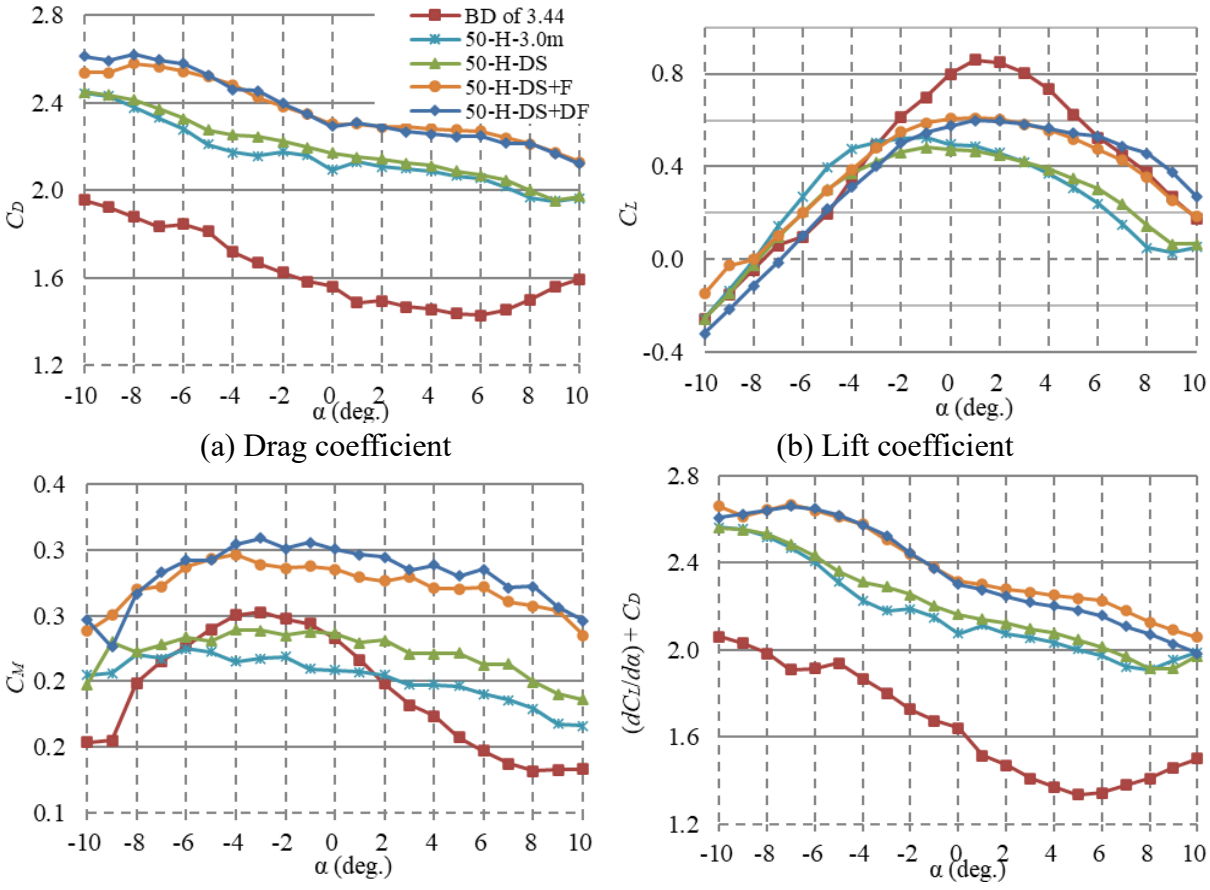

(a) Drag coefficient

(b) Lift coefficient

(c) Moment coefficient

(d) Galloping criterion

Figure 4.5 Aerodynamic force coefficients and galloping criterion of thick girder with countermeasures

4.4 Aerodynamic responses of bluff box girders with different side ratios

The presence of wind barriers significantly modifies the airflow around bridges, impacting their aerodynamic performance. This section examines the effects of various wind barrier configurations on the vertical and torsional vibration responses of the thick and thin girders at angles of attack of 0° and +3°. Table 4.1 summarizes the structural parameters of all cases.

In the aerodynamic response figures, the horizontal axis represents the wind velocity at the bridge site calculated based on the natural frequencies of the prototype, with values of 0.35 Hz for vertical and 1.52 Hz for torsional vibration modes (YOSHIDA et al., 1999). The vertical axis displays the vibration amplitudes of vertical mode (mm) and torsional mode (deg.).

The study began by selecting a hole scheme as the basic design for the wind barriers. Subsequently, the impact of different porosity ratios was analyzed to identify the most effective configuration. Additionally, the feasibility and cost-effectiveness of strategically positioning wind barriers above the handrails were evaluated.

The findings indicated that wind barriers notably increase the vertical VIV amplitude for both girder types. Consequently, this section suggests several strategies to mitigate these vibrations, including modifying the design of the standard wind barrier, incorporating flaps, and reducing its height to 2.5 meters as elaborated in section 4.2.2. These strategies are designed to mitigate the adverse effects of wind barriers on vertical VIV. Overall, this comprehensive analysis provides valuable insights into the complex interactions between wind barriers and bridge girders, proposing effective approaches to improve bridge aerodynamics and vehicle safety on bridges.

Table 4.1 Structural characteristic parameters for free vibration tests

Case	Thick girder (BD of 3.44)						Thin girder (BD of 4.98)					
	m	I	δ		f		m	I	δ		f	
			V	T	V	T			V	T	V	T
Bare deck	2.94	0.0220	0.03	0.012	3.42	7.26	2.95	0.0386	0.03	0.007	3.29	9.00
25-V	3.00	0.0233	0.03	0.013	3.39	7.12	-	-	-	-	-	-
50-V	2.98	0.0230	0.03	0.011	3.39	7.15	-	-	-	-	-	-
25-H	3.00	0.0234	0.03	0.014	3.38	7.10	3.01	0.0400	0.03	0.012	3.25	8.88
50-H-3.0m	2.98	0.0229	0.03	0.011	3.40	7.16	2.99	0.0395	0.03	0.007	3.26	8.93
50-H-P	2.96	0.0225	0.03	0.011	3.41	7.21	2.97	0.0391	0.03	0.007	3.26	8.95
50-H-2.5m	-	-	-	-	-	-	2.98	0.0394	0.03	0.008	3.26	8.93
70-H	2.97	0.0228	0.03	0.011	3.40	7.18	2.99	0.0394	0.03	0.007	3.26	8.94
50-H-DS	2.98	0.0228	0.03	0.011	3.40	7.16	2.99	0.0394	0.03	0.007	3.25	8.92
50-H-DS+F	3.01	0.0234	0.03	0.013	3.38	7.07	-	-	-	-	-	-
50-H+F	-	-	-	-	-	-	3.02	0.0403	0.03	0.008	3.24	8.84

Notes: 1) m is mass (kg/m) and I is moment of inertia ($kg \times m^2/m$).

2) δ is damping (logarithmic decrement).

3) f is the natural frequency (Hz).

4) V and T are vertical and torsional vibration modes.

4.4.1 Effects of hole schemes

The influence of various wind barrier hole schemes, oriented horizontally (H) and vertically (V), with porosity ratios of 25% and 50%, on the aerodynamic responses of the thick girder (BD of 3.44) is depicted in Figure 4.6 and 4.7. The findings indicate that the hole schemes have a minimal impact on vertical vibrations and torsional flutter. In all cases, the critical wind velocity for flutter exceeded 80 m/s for both angles of attack as in Figures 4.6 and 4.7 (b). Nonetheless, Figure 4.6 (a) reveals a slight variation in the onset wind velocity for vertical VIV at α = 0°. The findings align with prior research (Lin et al., 2022; Zhang et al., 2020) that highlighted the limited influence of hole schemes on wind flow characteristics above bridge girders.

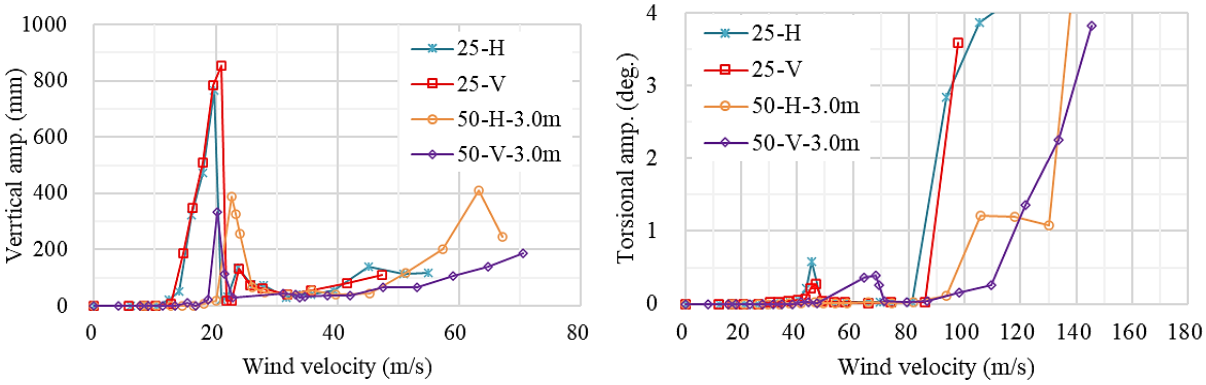

(a) Vertical response (b) Torsional response

Figure 4.6 Aerodynamic responses of thick girder (BD of 3.44) with different hole scheme wind barriers (α = 0°)

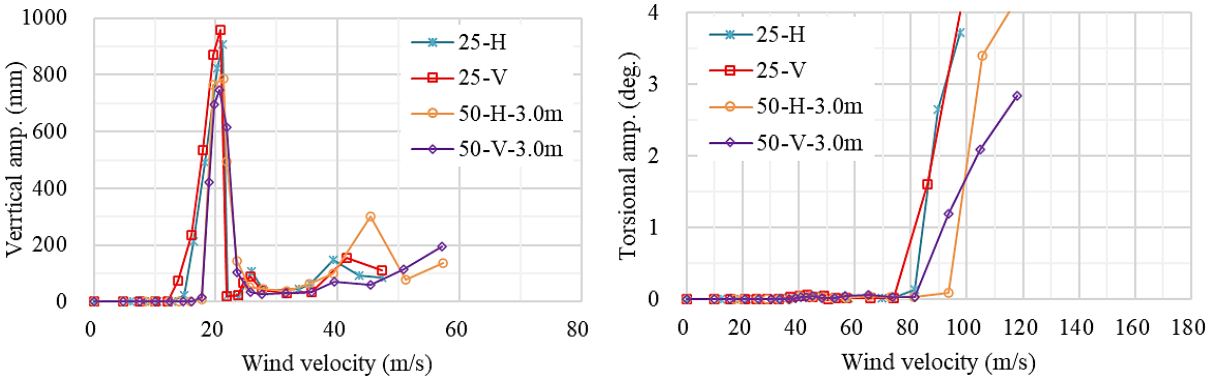

(a) Vertical response (b) Torsional response

Figure 4.7 Aerodynamic responses of thick girder (BD of 3.44) with different hole scheme wind barriers (α = +3°)

It is noteworthy that the VIV responses for both vertical and torsional modes demonstrate almost identical trends across both porosity ratios sharing the same hole schemes. However, an exception occurs with the horizontal hole scheme at a 50% porosity ratio (50-H-3.0m), which

effectively suppresses torsional VIV in both angles of attack as illustrated in Figures 4.6 and 4.7 (b). This configuration also elevates the corresponding wind velocity of vertical VIV from approximately 20 m/s to around 22 m/s as in Figure 4.6 (a), potentially enhancing traffic regulation during strong winds. The performance improvements observed in this case may be attributed to localized turbulence generated around the barrier's bar members, which are less pronounced in the 25% porosity cases that more closely resemble a solid wall.

Hence, the horizontal hole scheme was chosen for further investigation. This decision was based not only on its aerodynamic benefits but also on factors such as ease of installation and maintenance, which are anticipated to lead to reductions in overall costs. This approach aligns with the goal of optimizing both the structural and economic efficiency of wind barrier implementations on bridges.

4.4.2 Effects of porosities

The porosity ratio is a critical parameter in wind barriers, profoundly influencing both the aerodynamic performance of bridges and the safety and comfort of vehicle traffic as detailed in Section 2.6. This section explores the impact of porosity ratios of 25%, 50%, and 70% on the aerodynamic responses of bridge girders.

A clear pattern in the vertical vibration response of both girders is evident from Figures 4.8 and 4.9 for both angles of attack, except for the occurrent of rolling vibration in the thin girder with 25% porosity case (25-H) at $\alpha = +3°$, as shown in Figure 4.9 (b). The amplitude of vertical VIV for both girders increases significantly as the porosity ratio decreases. Specifically, the amplitudes are about 3.3 times, 1.8 times, and 1.3 times higher at $\alpha = 0°$, and even more pronounced at 6.2 times, 4.0 times, and 3.4 times at $\alpha = +3°$, for porosity ratios of 25%, 50%, and 70%, respectively, compared to the bare deck cases. This indicates that the detrimental effects of wind barriers are more accentuated at $\alpha = +3°$ for both girders. These observations align with prior studies that noted a similar trend in VIV.

Additionally, wind barriers with varying porosity ratios significantly influence the corresponding wind velocity for vertical VIV. For the thick girder, the corresponding wind velocity increases from approximately 18 m/s to 22 m/s at $\alpha = 0°$, and from 20 m/s to 21 m/s at $\alpha = +3°$. For the thin girder, these velocities rise from 16 m/s to 20 m/s at $\alpha = 0°$, and from 18 m/s to 22 m/s at $\alpha = +3°$. Notably, a porosity ratio of 70% markedly reduces the VIV amplitudes to levels similar to those observed in the bare deck cases at $\alpha = 0°$. Furthermore, this highest porosity ratio results in the smallest amplitude at $\alpha = +3°$ compared to other porosity ratios.

The notable enhancement in torsional VIV suppression for both girders, as facilitated by the installation of wind barriers, is illustrated in Figures 4.10 and 4.11. For the thick girder, a porosity ratio of 50% effectively stabilizes torsional VIV at both angles of attack (Figure 4.10 (a, b), while other porosity ratios (25% and 70%) also significantly reduce the amplitude when compared to the bare deck cases. In the case of the thin girder, wind barriers at all tested porosity ratios successfully suppress torsional vibrations within a wind velocity of 80 m/s (Figure 4.11 (a, b)).

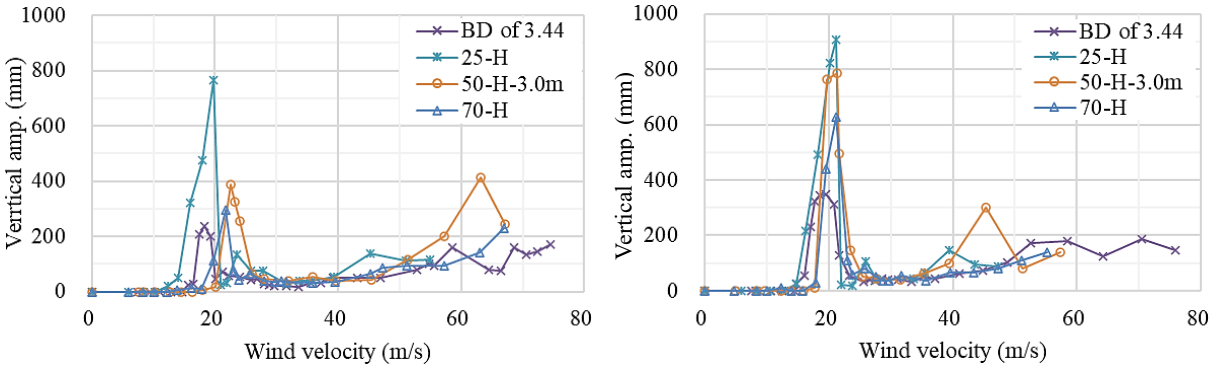

(a) $\alpha = 0°$ (b) $\alpha = +3°$

Figure 4.8 Vertical aerodynamic response of thick girder (BD of 3.44) with different porosity wind barriers

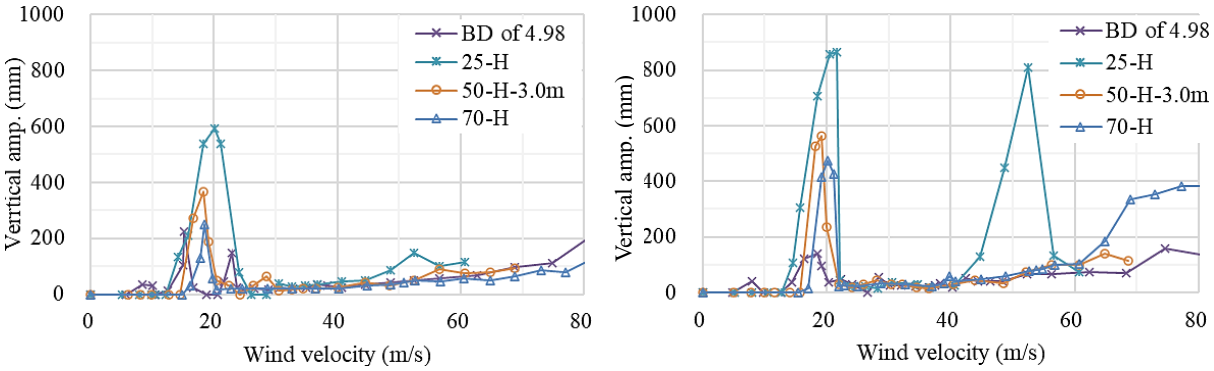

(a) $\alpha = 0°$ (b) $\alpha = +3°$

Figure 4.9 Vertical aerodynamic response of thin girder (BD of 4.98) with different porosity wind barriers

However, a decrease in critical wind velocity for flutter is observed in both girders. At $\alpha = 0°$, the wind barriers with porosity ratios of 70%, 50%, and 25% result in a reduction of the critical wind velocity for flutter in the thick girder from approximately 110 m/s to about 98 m/s, 94 m/s, and 82 m/s, respectively. Similarly, in the thin girder, the critical wind velocity decreases from around 170 m/s to approximately 135 m/s, 120 m/s, and 80 m/s. These results are consistent with previous studies that have demonstrated a reduction in critical wind velocity for flutter as porosity decreases (Wang et al., 2022).

An intriguing outcome is noted in the thick girder at an $\alpha = +3°$ (Figure 4.10 (b)), where the critical wind velocity for flutter exhibits an increase. Specifically, with the installation of wind barriers, the critical wind velocity rises from approximately 76 m/s in the bare deck case to over 81 m/s.

Considering the findings discussed in this section, the 50% porosity ratio case has been selected as the standard wind barrier for further testing. This decision is based on its performance in showing acceptable vertical VIV amplitude and its ability to stabilize torsional VIV for both girders at all tested angles of attack under the wind velocity of 80 m/s. While the

70% porosity case exhibits the smallest vertical VIV amplitude, it still induces torsional VIV in the girders. Additionally, its effectiveness in shielding against wind is significantly lower than that observed in the 50% porosity case which will be discussed in Section 4.5.3. Thus, the 50% porosity ratio strikes a balance between reducing vibration amplitudes and maintaining effective wind shielding, making it the preferred choice for subsequent experiments.

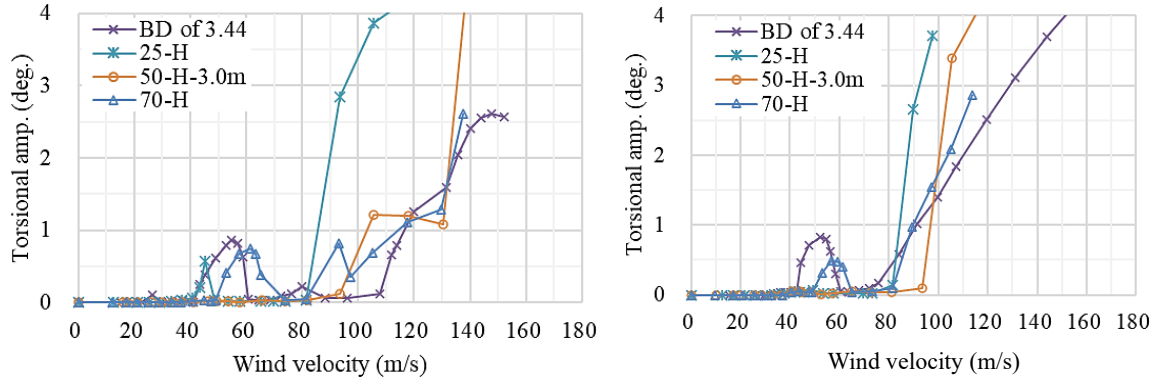

(a) $\alpha = 0°$ (b) $\alpha = +3°$

Figure 4.10 Torsional aerodynamic response of thick girder (BD of 3.44) with different porosity wind barriers

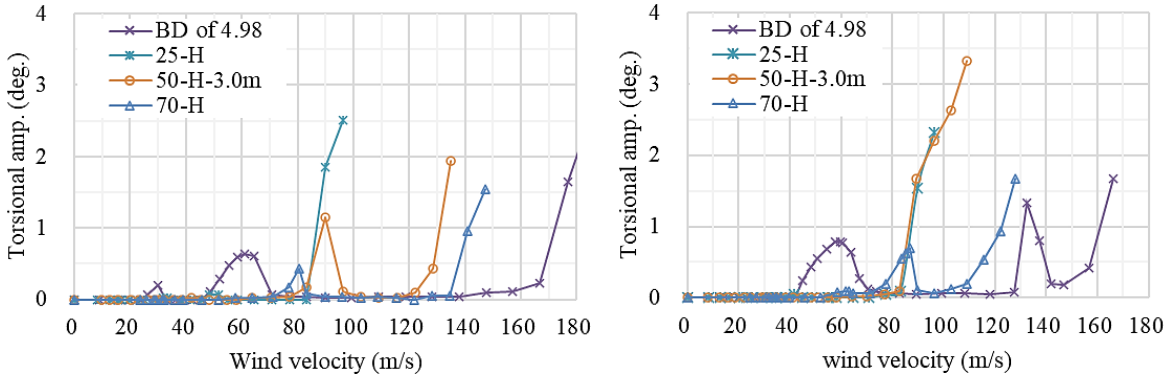

(a) $\alpha = 0°$ (b) $\alpha = +3°$

Figure 4.11 Torsional aerodynamic response of thin girder (BD of 4.98) with different porosity wind barriers

4.4.3 Effects of installation methods

The comparative results of the effects of installing a full wind barrier along the handrails (50-H-3.0m, named standard wind barrier) versus a partial wind barrier positioned above the handrails (50-H-P) on the vertical and torsional vibrations of both girders reveal some insightful outcomes. In the thick girder, at $\alpha = 0°$, the partial installation (50-H-P) dramatically reduces the vertical VIV by approximately 2.2 times compared to the standard wind barrier (50-H-3.0m) and by 1.3 times relative to the bare deck, as depicted in Figure 4.12 (a). This setup also increases the critical wind velocity for flutter to over 110 m/s, though it results in

torsional VIV appearing at an onset wind velocity of about 95 m/s, as shown in Figure 4.14 (a). Furthermore, at α = +3°, the partial installation exhibits a reduction in the vertical VIV amplitude for the first and second modes by about 1.2 times and 1.5 times, respectively, compared to the standard wind barrier, as in Figure 4.12 (b).

Additionally, the partial installation triggers the second vertical VIV mode at an onset wind velocity from approximately 27 m/s to 31 m/s in the thin girder, as illustrated in Figure 4.13 (b). This second mode of vibration, characterized as rolling vibration, occurs at a wind frequency different from the first mode. The first vibration mode, in contrast, is a vertical flexural vortex-induced vibration whose frequency aligns with the heaving natural frequency of the system.

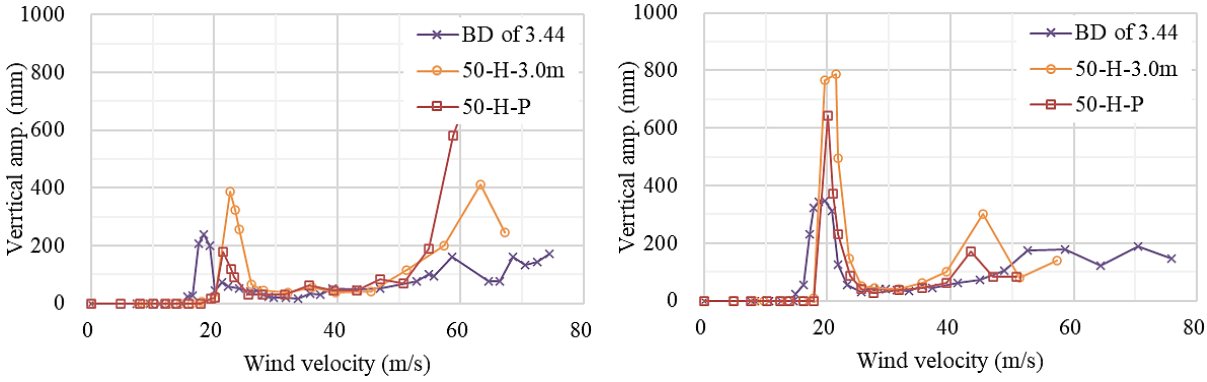

(a) α = 0° (b) α = +3°

Figure 4.12 Vertical aerodynamic response of thick girder (BD of 3.44) with different installation methods

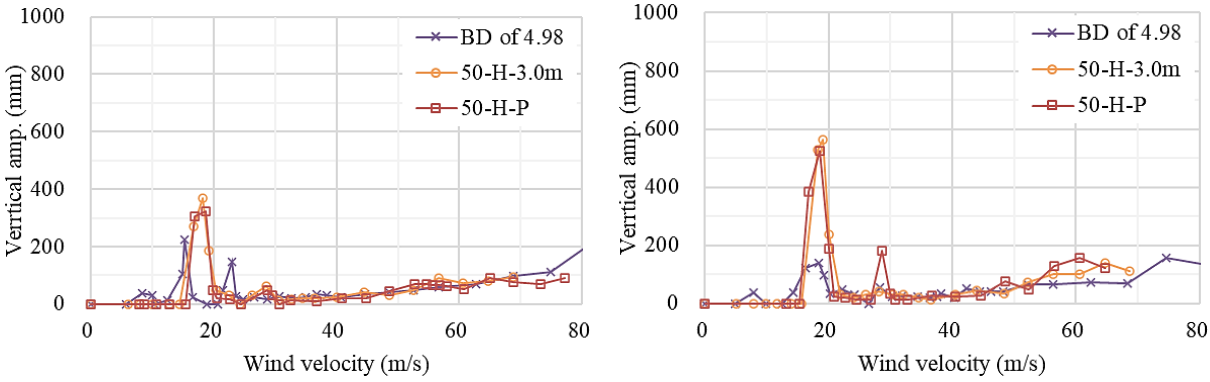

(a) α = 0° (b) α = +3°

Figure 4.13 Vertical aerodynamic response of thin girder (BD of 4.98) with different installation methods

Furthermore, the wind barriers effectively stabilize torsional VIV within a wind speed of up to 80 m/s for both girders at all angles of attack, as in Figures 4.14 and 4.15. Additionally, they

elevate the critical wind velocity for flutter in the thick girder from approximately 75 m/s to over 90 m/s at $\alpha = +3°$, as depicted in Figure 4.15 (b). However, contrasting outcomes are noted for the thin girder, where the critical wind velocity for flutter decreases, yet it remains above the design threshold of 67.8 m/s.

These results indicate that installing partial wind barriers not only generally enhances aerodynamic stability but also benefits a cost-effective and time-efficient manner, making it a viable strategy for improving bridge safety and performance.

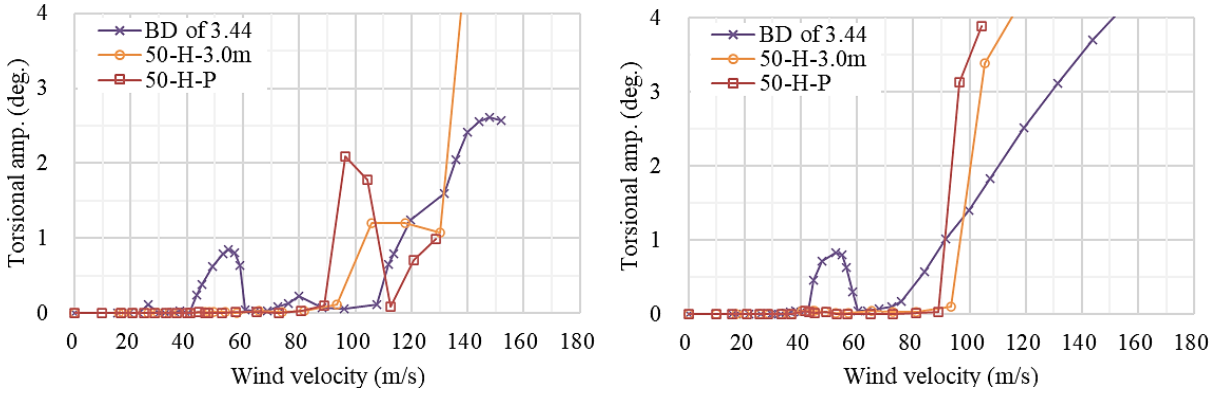

(a) $\alpha = 0°$ (b) $\alpha = +3°$

Figure 4.14 Torsional aerodynamic response of thick girder (BD of 3.44) with different installation methods

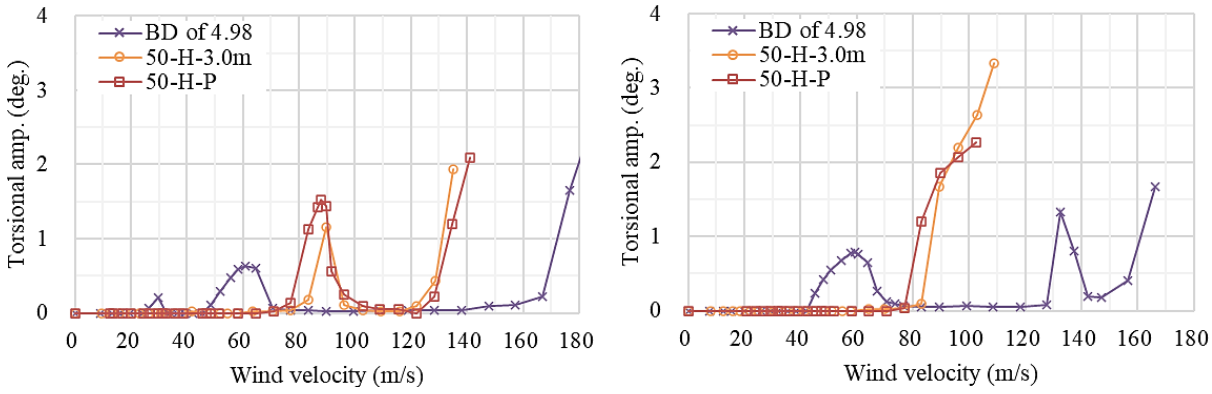

(a) $\alpha = 0°$ (b) $\alpha = +3°$

Figure 4.15 Torsional aerodynamic response of thin girder (BD of 4.98) with different installation methods

4.4.4 Countermeasures to stabilize VIV

This section focuses on stabilizing the increased vertical VIV amplitudes induced by wind barriers, as discussed in the previous sections. The 50% porosity wind barrier with a height of 3.0 m (50-H-3.0m) was selected for modification. This choice was based on the aerodynamic responses observed in both girders, detailed in the preceding sections. Additionally,

considerations were given to potential wind speed reductions to enhance vehicle driving safety and minimize obstruction scenarios when implemented on an actual bridge.

4.4.4.1 Height and bar arrangement

The effectiveness of the different spacing wind barrier (50-H-DS) in stabilizing vertical VIV for the thick girder at $\alpha = 0°$ is shown in Figure 4.16 (a). This barrier successfully reduces the amplitude compared to both the standard wind barrier (50-H-3.0m) and the bare deck (BD of 3.44) by 2.1 times and 1.3 times, respectively. However, at $\alpha = +3°$, although the amplitude is still higher than that of the bare deck by about 1.6 times, it is lower than that of the standard barrier by about 1.4 times (Figure 4.16 (b)). The possibility of this improvement may be attributed to the enlarged hole spacing at the lower part of the wind barrier, which facilitates more wind flow and influences vortex shedding and formation near the girder surfaces, which is one of the most important factors impacting the mechanism of vortex-induced vibration.

Despite reducing the amplitude for the thick girder, the different spacing barrier exhibits similar vibrational results to the standard barrier for the thin girder at both angles of attack as shown in Figure 4.17. Therefore, the height of the standard wind barrier was reduced to 2.5 m (50-H-2.5m) for this girder to potentially decrease the blockage area, thereby reducing the wind load on the bridge which might enhance aerodynamic performance. However, similar to the different spacing barrier, it fails to stabilize vertical VIV, with the second mode of rolling vibration observed at an onset wind speed from 25 m/s to 29 m/s at $\alpha = +3°$ (Figure 4.17 (b)).

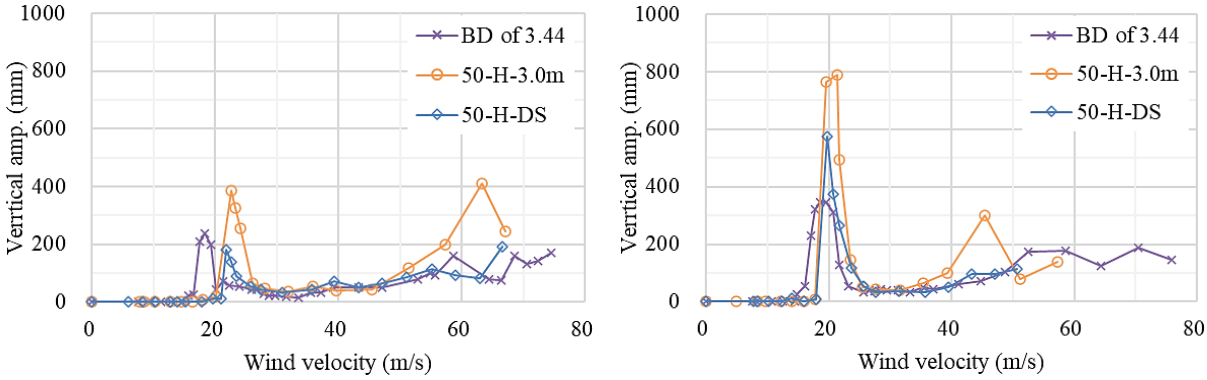

(a) $\alpha = 0°$ (b) $\alpha = +3°$

Figure 4.16 Vertical aerodynamic response of thick girder (BD of 3.44) with different bar arrangements

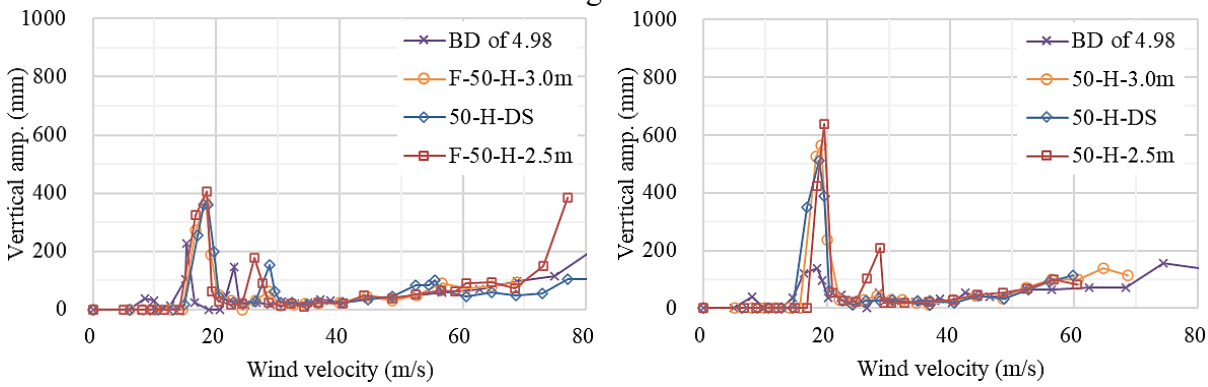

(a) $\alpha = 0°$ (b) $\alpha = +3°$

Figure 4.17 Vertical aerodynamic response of thin girder (BD of 4.98) with different heights and bar arrangements

The different spacing barrier not only stabilizes the vertical VIV amplitude for the thick girder at $\alpha = 0°$ but also stabilizes torsional VIV under a wind velocity of 90 m/s as in Figure 4.18 (a) with increased critical wind velocity for flutter from approximately 93 m/s (standard barrier) and 103 m/s (bare deck) to 130 m/s (Figure 4.18 (b)). The results of the thin girder in Figure 4.19 indicate that both countermeasures of different spacing and 2.5-m wind barriers exhibit almost identical vibrational responses with the standard wind barrier, with a slight decrease in wind velocity for flutter at $\alpha = 0°$ for the 2.5 m high wind barrier case at $\alpha = 0°$, reducing it from 122 m/s to 109 m/s compared to the standard barrier (Figure 4.19 (a)). Additionally, both the standard wind barrier and all countermeasures successfully suppress torsional VIV under a wind velocity of 80 m/s.

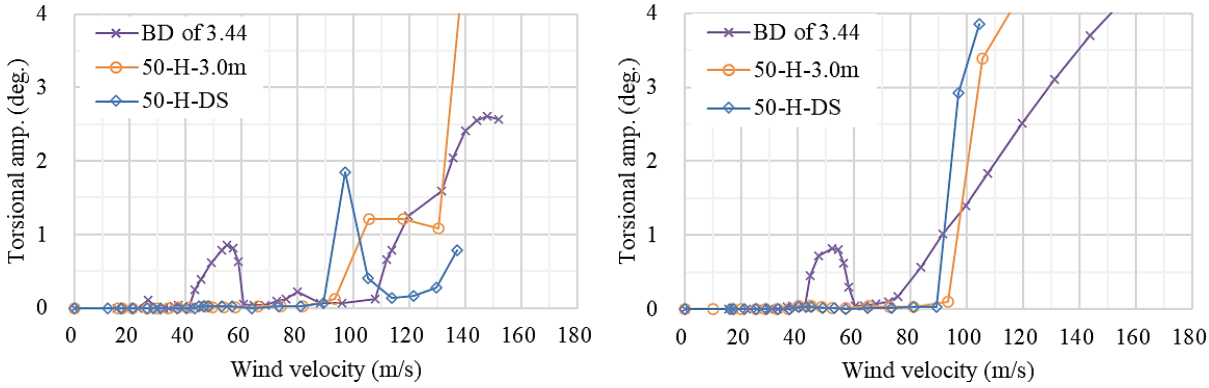

(a) $\alpha = 0°$ (b) $\alpha = +3°$

Figure 4.18 Torsional aerodynamic response of thick girder (BD of 3.44) with different heights and bar arrangements

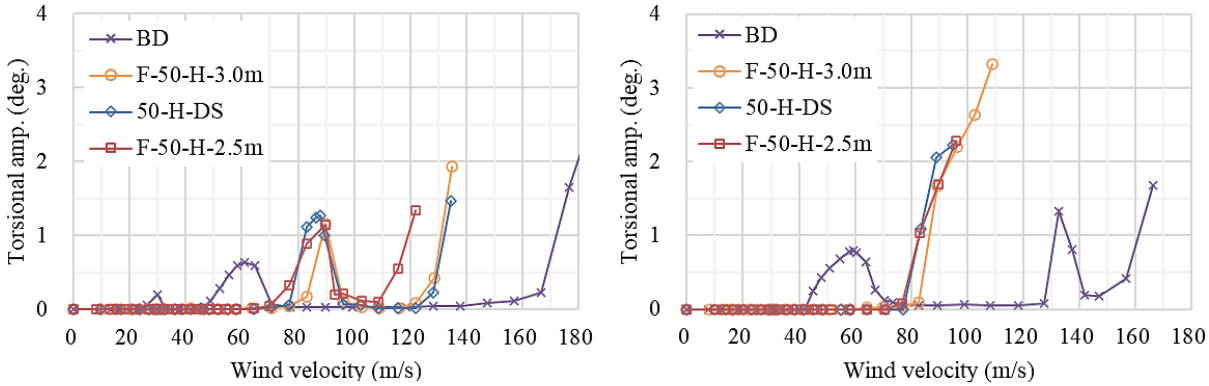

(a) $\alpha = 0°$ (b) $\alpha = +3°$

Figure 4.19 Torsional aerodynamic response of thin girder (BD of 4.98) with different heights and bar arrangements

4.4.4.2 Combination with flaps

Given that the different spacing wind barrier still exhibited a higher vertical VIV amplitude than the bare deck at α = +3° in the thick girder, and both the previously mentioned countermeasures (50-H-DS and 50-H-2.5m) failed to reduce the amplitude of such vibration in the thin girder, as discussed in section 4.4.4.1, additional measures were implemented. Single and double flaps were added to the different spacing wind barrier due to its proven efficiency in suppressing VIV at α = 0° for the thick girder. Similarly in the thin girder, the flaps were attached to the standard wind barrier, as there were no significant differences between it and the countermeasures and to avoid potentially reduced wind shielding effectiveness resulting from the lower height (50-H-2.5m) and larger spacing at the bottom part (50-H-DS), which could allow more wind to act on the vehicles.

For the thick girder, the integration of flaps (50-H-DS+F and +DF) proves highly effective in stabilizing vertical VIV, as in Figure 4.20. Comparing to the bare deck (BD of 3.44) and different spacing wind barrier (50-H-DS), this approach reduces the amplitude by about 1.5 times and 2.5 times (α = 0°), and 5.1 times and 11.6 times (α = +3°) with a substantial increase in the corresponding onset wind velocity from about 18 m/s and 22 m/s to about 26 m/s (α = +0°) and about 20 m/s and 21 m/s to about 30 m/s (α = +3°), respectively. This finding not only significantly reduces the vertical VIV amplitude but also enhances traffic control regulations due to the increased corresponding wind velocity under strong crosswind conditions.

This outcome is consistent with a previous study that found a similar trend in a bluff-box girder with a side ratio of 3.81, where the installation of a flap not only generated small negative aerodynamic damping but also energized the shear layer forming at the leading edge of the section, while diminishing vortex formation near the girder surface (Sarwar and Ishihara, 2010).

However, the flaps have a limited effect in stabilizing vertical VIV in the thin girder at both angles of attack (Figure 4.21). Similar to the previous countermeasures, the vertical VIV amplitude with and without flaps shows an almost identical vibrational trend.

At α = +3°, both flaps induce galloping in the thick girder at wind velocities of about 43 m/s and 54 m/s for double and single flaps (50-H-DS+SF and +F), respectively, but the galloping in the thin girder is observed at a wind velocity of about 64 m/s in the case of the double flap (50-H+DF) only. Overall, both flaps exhibit a similar vibrational trend for vertical VIV, but the single flap shows better performance in terms of galloping.

The stabilization of torsional VIV under a wind velocity of 80 m/s for both girders at different angles of attack is depicted in Figures 4.22 and 4.23. Additionally, for the thick girder, the combination with flaps increases the critical wind velocity for flutter. Specifically, it increases from approximately 115 m/s and 91 m/s to about 140 m/s at α = 0°, and from approximately 73 m/s and 91 m/s to about 100 m/s at α = +3°, in comparison to the bare deck and different spacing wind barrier. Conversely, the thin girder exhibits a lower critical wind velocity compared to the bare deck case, yet it remains higher than that observed with the standard wind barrier.

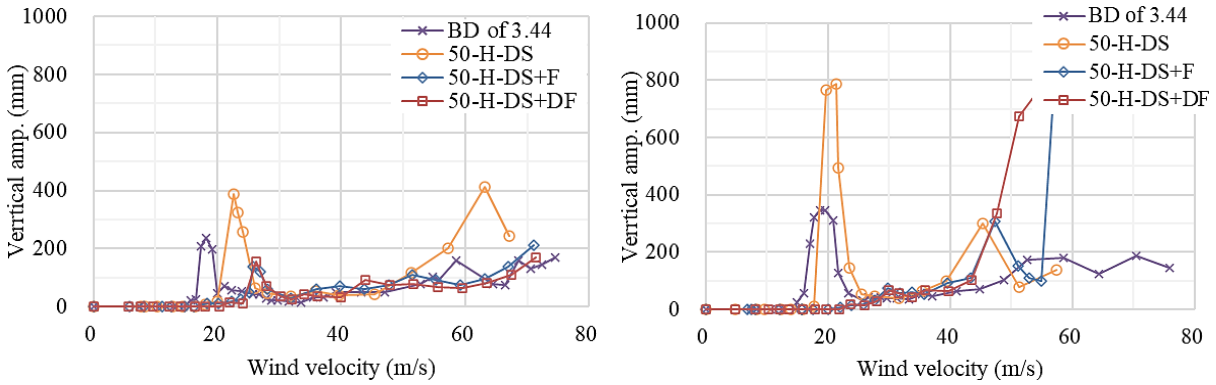

(a) $\alpha = 0°$ (b) $\alpha = +3°$

Figure 4.20 Vertical aerodynamic response of thick girder (BD of 3.44) with wind barriers combined with flaps

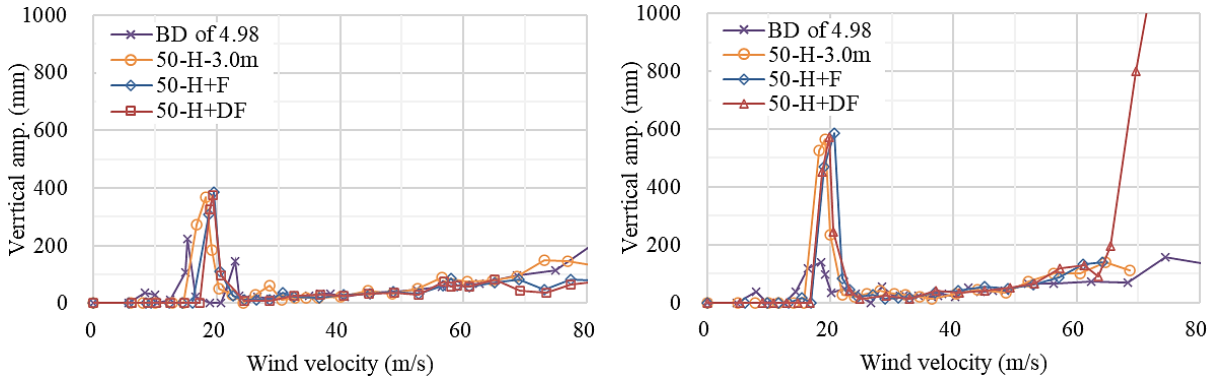

(a) $\alpha = 0°$ (b) $\alpha = +3°$

Figure 4.21 Vertical aerodynamic response of thin girder (BD of 4.98) with wind barriers combined with flaps

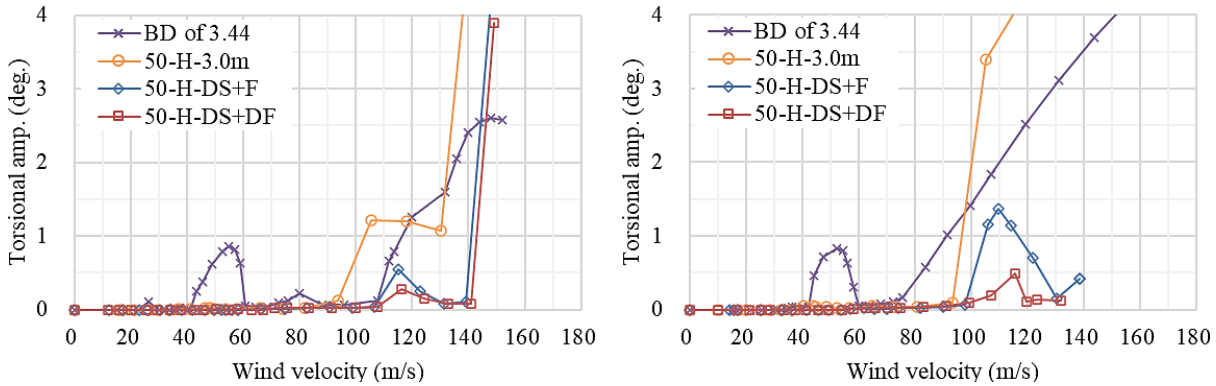

(a) $\alpha = 0°$ (b) $\alpha = +3°$

Figure 4.22 Torsional aerodynamic response of thick girder (BD of 3.44) with wind barriers combined with flaps

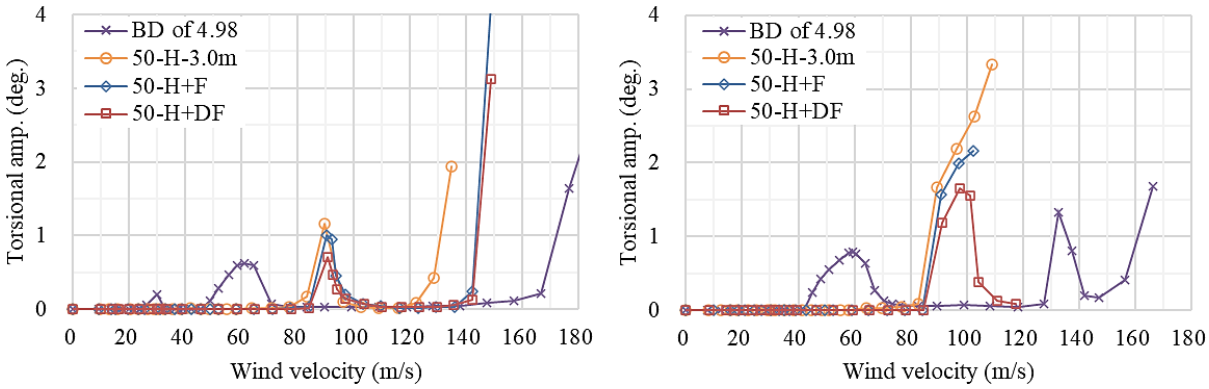

(a) $\alpha = 0°$ (b) $\alpha = +3°$

Figure 4.23 Torsional aerodynamic response of thin girder (BD of 4.98) with wind barriers combined with flaps

4.5 Wind flow field above the bluff box girders with different side ratios

This section explores the impact of wind barriers on the characteristics of the wind flow field over bluff box girders with different side ratios of 3.44 and 4.98, corresponding to thick and thin girders, respectively. Initially, we analyze the flow patterns above both thick and thin girders and explore how these patterns are altered by the presence of wind barriers in Section 4.5.1. Subsequently, we discuss the relationship between the flow field and the vertical Vortex-Induced Vibration (VIV) amplitude for a basic understanding of how wind barriers can either stabilize or destabilize this vibration in Section 4.5.2. Finally, the effectiveness of wind barriers with different parameters in reducing mean and maximum wind speeds is detailed in Section 4.5.3, highlighting their potential to enhance vehicle driving safety.

4.5.1 Flow patterns above the bluff box girders and their alteration by wind barriers

This section examines the flow patterns over both girders and how they are changed by wind barriers, focusing on the mean wind velocity vector and turbulence intensity distributions. At the center of each girder, an arrow and a line represent the nondimensional wind velocity vector ($U = 1$) and turbulence intensity ($I_u = 1$), respectively. Turbulence intensity is defined as the local standard deviation of a measurement point divided by approaching wind velocity. Detailed information on the distribution points is provided in Section 3.5. The horizontal axis (X/B) represents the normalized distance from the center of the girders (X), relative to their widths (B). The vertical axis (Y/D) denotes the normalized distance from the bottom surface of the girders (Y), relative to their depths (D).

The flow field observed over both bluff box girders with different side ratios, as delineated in Figures 4.24 and 4.25, demonstrates notable distinctions in the patterns of flow separation and turbulence characteristics. Both girders manifest separation phenomena on the upper windward side immediately behind the handrail. However, the flow dynamics differ significantly beneath a relative height of about $X/B = 1.5$.

For the thick girder as in Figures 4.24 (a) and 4.25 (a), the distribution of wind velocity vectors is considerably compact, with limited vertical dispersion near the girder surface, suggesting a more coherent and uniform flow influenced predominantly by the girder's

substantial presence. This results in overall reduced wind velocities and increased turbulence intensities when compared to the thin girder. The progression of boundary layer separation from the leading edge towards the leeward edge is marked by a corresponding increase in turbulence intensity. The turbulence near the girder surface is intensified, indicative of larger eddy formations and more robust turbulent activities, contributing to a broader wake region characterized by substantial flow disturbances.

Conversely, the thin girder exhibits a disparate flow. The wind velocity vectors display greater vertical distribution, which may signify a reattachment of the flow after its initial separation at the leading edge, potentially diminishing the wake region relative to the thick girder. This reattachment scenario corresponds with the observation of a narrower wake proximal to the deck surface at the girder's midpoint, as depicted in Figure 4.24 (b). Such reattachment contributes to a reduction in turbulence intensity at comparable heights relative to the thick girder as in Figure 4.25 (b), aligning with findings from a prior numerical simulation and underscoring the divergent flow behaviors intrinsic to the different side ratios (Kim et al., 2021).

In essence, the aerodynamic configuration of the thick girder promotes a more turbulent wake directly downstream, likely due to a larger separation bubble characteristic of bluff bodies with a more pronounced profile. In contrast, the thin girder, with its more streamlined shape, modifies the flow pattern allowing for flow reattachment, which may reduce the magnitude of the wake, the drag coefficient, and vortex-induced vibrations.

Additionally, the larger mean wind speed observed over the thin girder significantly elevates risks related to vehicle driving safety when compared to the thick girder aligning well with previous studies reported that the susceptibility is attributed to the aerodynamic characteristics of the thin girders with higher side ratios, which inherently experience increased wind speeds. Such conditions augment the aerodynamic force coefficients exerted on vehicles, thereby fostering driving instability as discussed in Section 2.6.

The insights from Figures 4.24 and 4.25 not only show the flow characteristics elucidating distinct aerodynamic behaviors of the two girder types but also provide valuable guidance for bridge girder design aimed at minimizing wind-induced accidents. The data suggests implementing strategic measures, such as the possibility of the partial installation of wind barriers on the thin girder only. This approach is particularly beneficial for bridges with girders of varying depths along the length, where selective barrier placement can significantly enhance overall driving safety, effectiveness of cost and time together with reducing the detrimental effect of wind barriers on the aerodynamic performance of bridges.

For the sake of conciseness and clarity, the alteration of the wind patterns above both thick and thin girders by wind barriers will be discussed through the standard wind barrier (50-H-3.0m) only. This choice is justified as other wind barriers have demonstrated similar effects on the flow patterns which can be found in Appendix 1. A detailed examination of how wind barriers influence the wind flow field, encompassing aspects such as turbulence intensity and wind velocity for both girder types, will be quantitatively discussed in more detail in subsequent sections, specifically Sections 4.5.2 and 4.5.3.

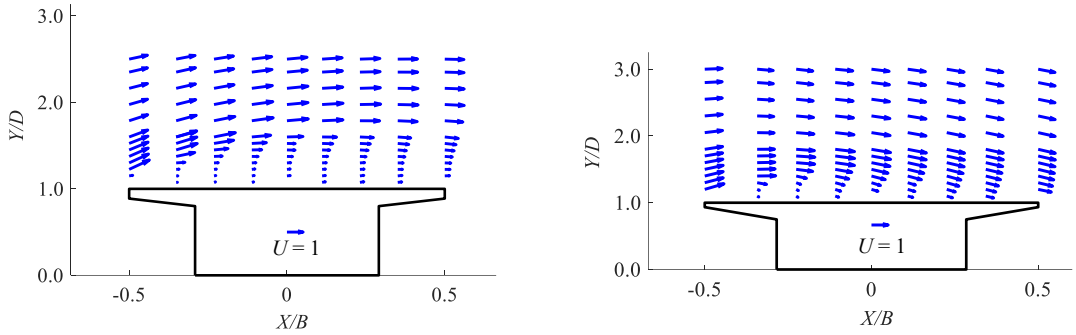

(a) Thick girder (BD of 3.44) (b) Thin girder (BD of 4.98)

Figure 4.24 Wind velocity vector distribution of bare deck cases

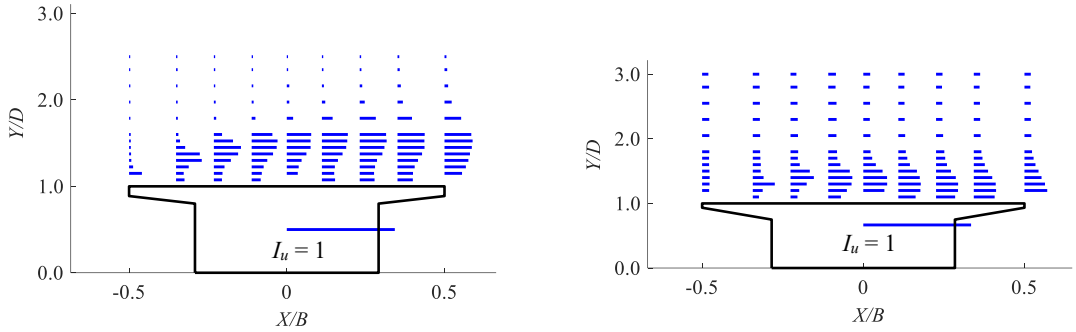

(a) Thick girder (BD of 3.44) (b) Thin girder (BD of 4.98)

Figure 4.25 Turbulence intensity distribution of bare deck cases

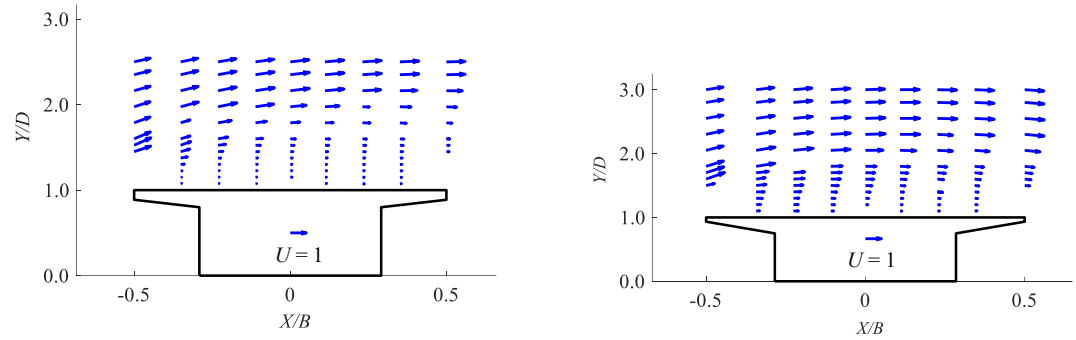

(a) Thick girder (BD of 3.44) (b) Thin girder (BD of 4.98)

Figure 4.26 Wind velocity vector distribution of the standard wind barrier (50-H-3.0m)

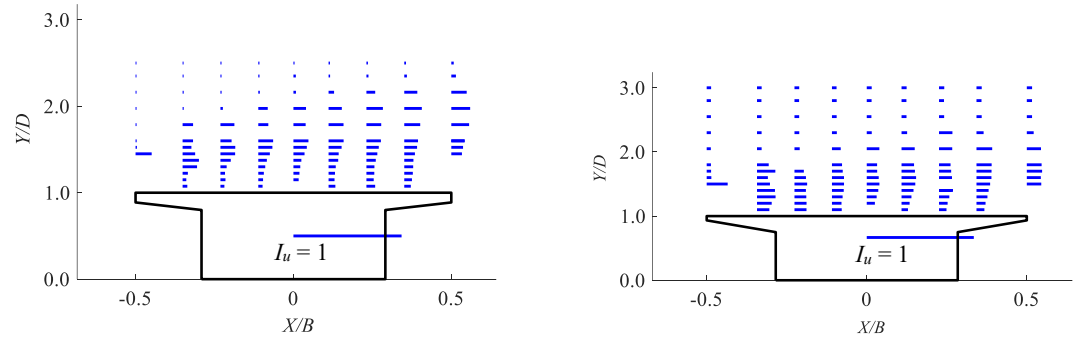

(a) Thick girder (BD of 3.44) (b) Thin girder (BD of 4.98)

Figure 4.27 Turbulence intensity distribution of the standard wind barrier (50-H-3.0m)

Figures 4.26 and 4.27 show that the presence of the standard wind barrier significantly modifies the flow patterns above both thick and thin girders. For the thick girder (Figures 4.26 and 4.27 (a)), the barrier alters the flow by moderating wind velocity vectors and significantly reducing turbulence intensity near the surface. In contrast, Figures 4.26 and 4.27 (b) show that the flow pattern of the thin girder undergoes a complete transformation by eliminating the reattachment of the flow, transitioning to a flow pattern more akin to that observed around the thick girder. Additionally, the region of flow acceleration shifts upward from a relative height of approximately $Y/D = 1.5$ to around 2.0, thereby broadening the wake region above the girder and substantially diminishing the turbulence intensity compared to the bare deck. This alteration from a reattached to detached flow type may attributed to the ineffectiveness of certain countermeasures aimed at stabilizing vertical VIV as compared to the thick girder. While the flow pattern of the thick girder is insignificantly changed by the wind barrier i.e. by those countermeasures. The decrease in wind velocity and turbulence intensity by the wind barrier significantly contributes to the driving safety enhancement.

4.5.2 Mean turbulence intensity above the bluff box girders and its alteration by wind barriers

This section discusses how wind barriers influence turbulence intensity, impacting vehicle driving safety and relating to the vertical VIV amplitude in both girders at $\alpha = 0°$. The details include the destabilization of such vibration by 25% and 50% porosity wind barriers (25-H and 50-H-3.0) in both girders and the stabilization by the countermeasures in the thick girder of a different spacing wind barrier and its combination with a single flap (50-H-DS and 50-H-DS+F). However, such countermeasures maintain consistent vibration amplitudes with the standard wind barrier (50-H-3.0m) in the thin girder (50-H-DS, 50-H+F, and 50-H-2.5), as depicted in Figure 4.28, which shows the peak vertical VIV amplitudes for both girders. Additional discussion on the aerodynamic responses is detailed in Section 4.4.

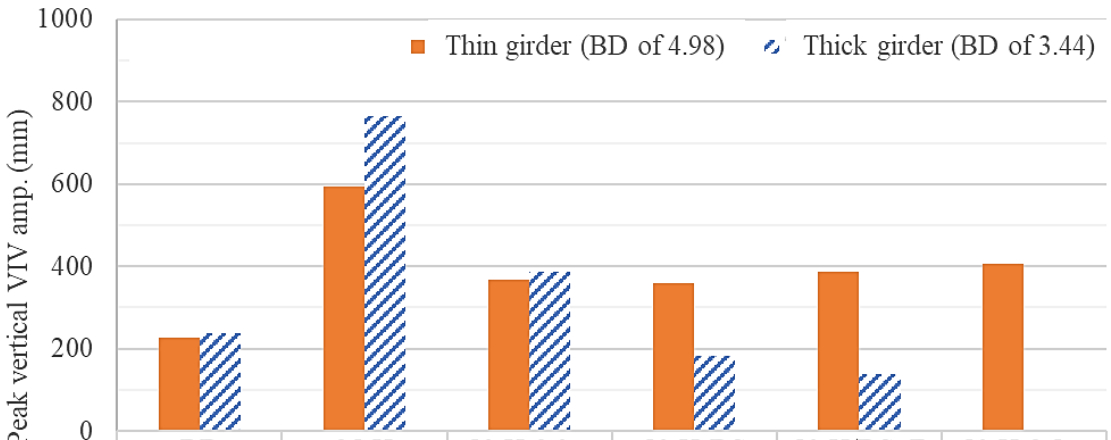

	BD	25-H	50-H-3.0m	50-H-DS	50-H/DS+F	50-H-2.5m
Thin	225.14	592.50	367.91	358.30	387.40	406.347
Thick	237.82	764.66	386.53	182.84	137.60	

Figure 4.28 Peak vertical VIV amplitude of both girders

Figures 4.29 and 4.30 show the nondimensional mean turbulence intensity of lanes 1 to lanes 6 (L1 to L6) and the center (C) of both girders. The vertical axis denotes the normalized distance from the bottom surface of the girders *Y/D* where *Y* is the relative distance and *D* is the depths of the girders.

The turbulence intensity variations above the thick girder are detailed in Figure 4.29. Below the height of approximately *Y/D* = 1.5, in the windward lanes ranging from L1 to C, there is a significant reduction in turbulence intensity with the implementation of the 25% and 50% porosity wind barriers (25-H and 50-H-3.0m) compared to the bare deck. Conversely, the turbulence intensity increases markedly with the two countermeasures (50-H-DS and +F), surpassing levels observed in the bare deck, particularly near the surface of the girder under *Y/D* = 1.25.

In the leeward lanes (L4 to L6), the turbulence intensity for all wind barriers and countermeasures remains below that of the bare deck at an approximately specific *Y/D* = 1.7. However, the turbulence of the countermeasures is still notably higher than the 25-H and 50-H-3.0m wind barriers. Across all cases under this height, the 25% porosity barrier consistently exhibits the lowest turbulence intensity, while the combination with a single flap shows the highest turbulence intensity below *Y/D* = 1.5 mark in all lanes relative to other wind barrier cases.

Figure 4.30 indicates that in the thin girder, even the countermeasures (50-H-DS, 50-H+SF, and 50-H-2.5m) tend to increase turbulence intensity in lanes L1 and L2 near the girder's surface below *Y/D* = 1.2. However, the turbulence intensity in other lanes (L3 to L6 and C) below *Y/D* = 1.5 remains significantly lower than that of the bare deck case. Moreover, the turbulence intensity in these lanes under *Y/D* = 2.0 of the different spacing barrier and the combination with a flap (50-H-DS and 50-H+SF) shows a consistent value with the standard wind barrier, indicating negligible effect relative to the turbulence increase observed in the thick girder. In almost all lanes under *Y/D* = 1.7, the 25% porosity barrier displays the lowest turbulence intensity, whereas the 2.5 m high wind barrier exhibits the highest compared to other wind barriers and countermeasures.

These findings suggest that the turbulence intensity near the surface, which directly relates to vortex shedding and its formation, is influenced by wind barriers and contributes to vertical VIV. The minimal turbulence intensity observed in the 25% porosity case correlates with the highest vibrational amplitudes in both girders. Meanwhile, the significant promotion in turbulence intensity by the countermeasures in the windward lanes of the thick girder demonstrates their effectiveness in stabilizing such vibrations. Additionally, the relatively low turbulence intensity near the surface of the thin girder of those countermeasures, compared to the bare deck, along with consistent turbulence intensity with the standard barrier, might contribute to the ineffectiveness in destabilizing the vertical VIV in the thin girder.

The changes in turbulence intensity by wind barriers and countermeasures above the girders not only contribute to the vertical VIV amplitude but also significantly affect vehicle driving safety. Under certain heights in most lanes of both girders, 25% and 50% porosity wind barriers (25-H and 50-H) reduce turbulence intensity significantly. In the thick girder, the turbulence intensity of all lanes except lane 1 under *Y/D* = 1.5, which is 4.25 m from the surface of the

girder on a real-world scale covering all heights of vehicle types, is relatively reduced compared to the bare deck case. This reduction is also pronounced in most lanes of the thin girder under *Y/D* of about 1.5 (3 m on a real-world scale from the surface of the girder) which covers the heights of most vehicles.

Although the countermeasures that effectively stabilize vertical VIV in the thick girder increase turbulence intensity primarily in the windward lanes under *Y/D* = 1.2 (approximately 2.1 m on a real-world scale), as in Figure 4.29, which surpasses the height of motorbikes and light vehicles, potentially compromising vehicle safety. However, these vehicles are less susceptible to wind-induced accidents compared to large vehicles.

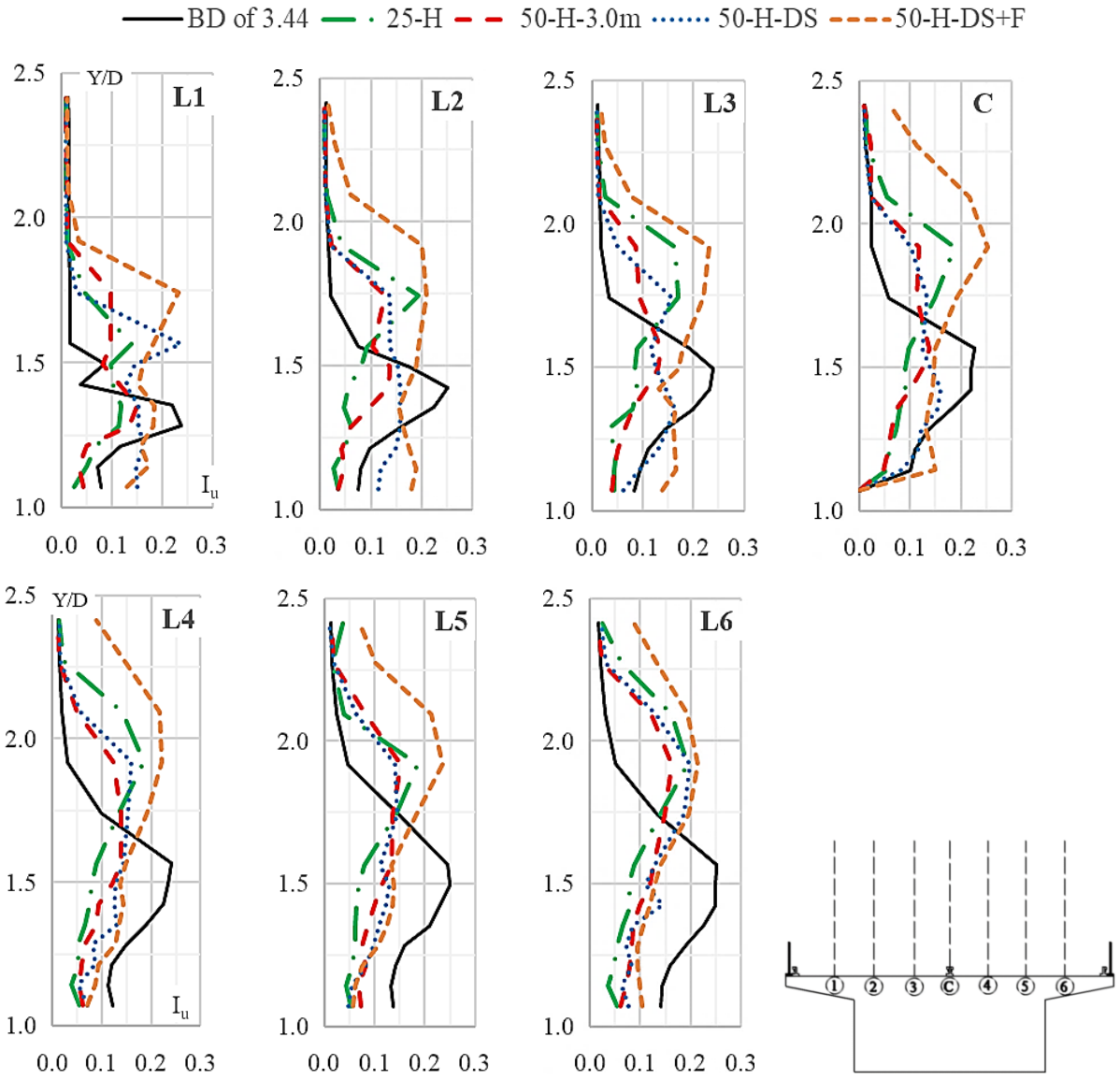

Figure 4.29 Mean turbulence intensity of thick girder (BD of 3.44) with wind barriers

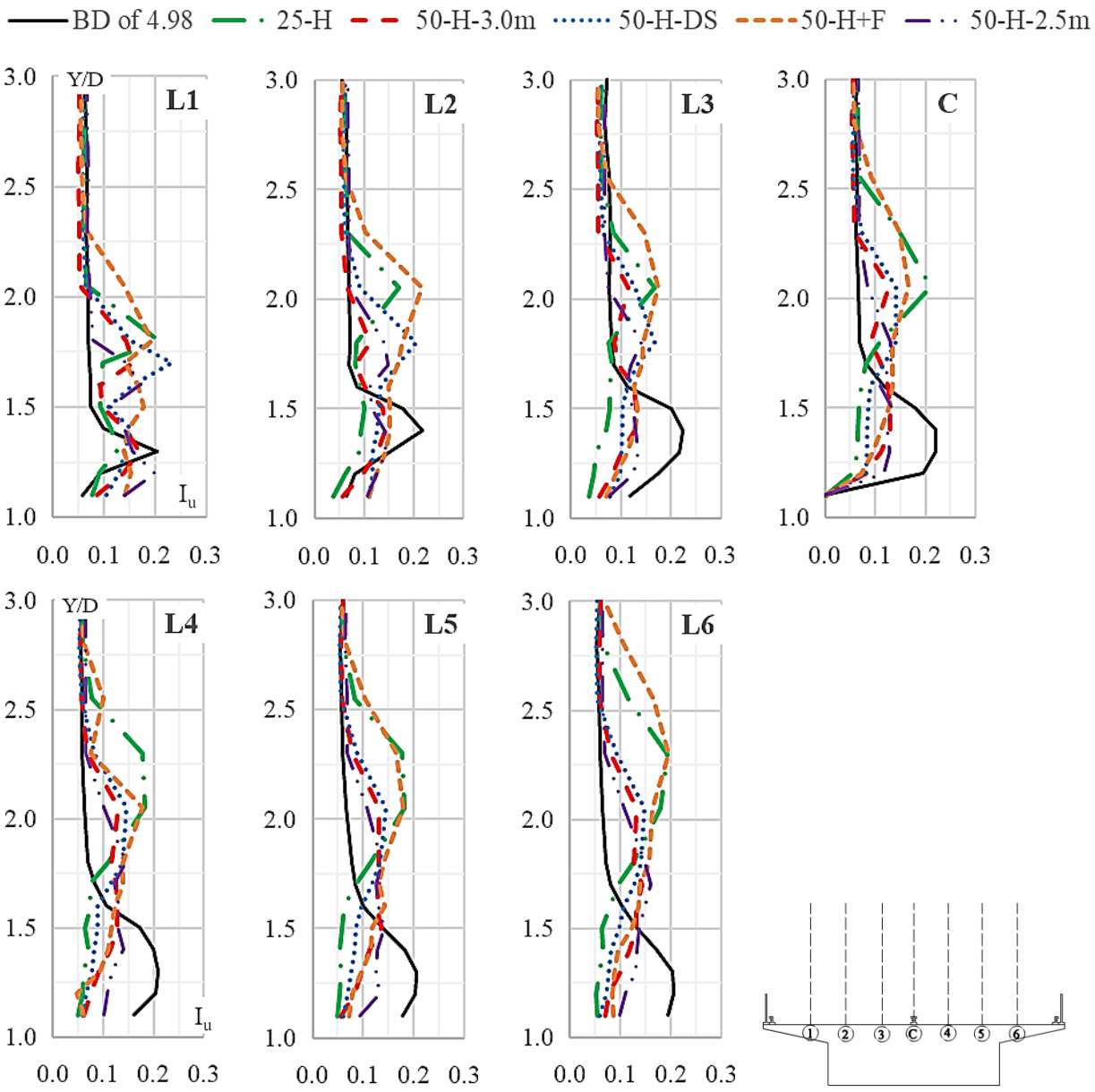

Figure 4.30 Mean turbulence intensity of thin girder (BD of 4.98) with wind barriers

In the case of the thin girder, the countermeasures that increase turbulence intensity affecting vehicle driving safety would not be employed in this girder since they failed to stabilize vertical VIV. Hence, in most lanes under the height of the shielding area that covers the heights of all vehicle types, wind barriers show relatively lower turbulence intensity.

Furthermore, heightened turbulence intensity may affect the reaction time available to drivers and escalate the driving difficulty, potentially resulting in loss of vehicle control. Thus, the 25% porosity barrier, which exhibits the lowest turbulence intensity across both girders, proves most beneficial in enhancing driving safety due to its superior shielding effectiveness. The specific impact of wind barriers on driving safety through mean and maximum wind speed reduction will be explored in greater detail in Section 4.5.3.

4.5.3 Efficacy of wind barriers in wind speed reduction

The impact of wind barriers including different porosity ratios, heights, and various countermeasures on reducing wind speed to enhance vehicle driving safety and comfort is detailed through mean and maximum wind velocity profiles above both girders. For clarity, these velocity profiles are represented on a real-world scale. The horizontal axis indicates the nondimensional wind speed normalized to the approaching wind speed and the vertical axis denotes the height above the girder surfaces. Three dashed lines mark the average heights of light, medium, and large vehicles at 1.6 m, 2.6 m, and 3.8 m, respectively.

Comparative result of bare deck girders (solid black line) in Figures 4.31 and 4.32, alongside wind vector distribution discussed in Section 4.5.1, reveals that the mean and maximum wind velocities under the height of 4 m—covering the height of all vehicle types—are generally larger in the thin girder compared to the thick girder. Notably, the height at which the thick girder reaches a nondimensional mean wind velocity of 1 consistently exceeds 4 m, whereas the thin girder reaches this velocity at only about 2 m. These differences highlight the thin girder's increased vulnerability to strong crosswinds, particularly in the first lane where maximum wind speeds can accelerate to 3.0 times the approaching wind speed, compared to approximately 2.0 times in the thick girder.

These observations underscore how side ratios significantly influence wind characteristics along bridges, corroborating with findings from previous numerical and field studies (KANEKO et al., 2022; Kim et al., 2023, 2021). The thin girder's heightened susceptibility to wind-induced accidents informs strategic decisions, such as installing wind barriers predominantly in areas of higher side ratios, like the central span of the bridge.

Considering the area below 4 m as a critical shielding zone for vehicles, Figures 4.31 and 4.32 show that the 25% and 50% porosity wind barriers (25-H and 50-H-3.0m) effectively reduce both mean and maximum wind velocities across all lanes of both girders within this zone. The reduction in mean wind velocity is approximately 3 times and 2 times, while the maximum wind velocity reduces by about 4 times and 3.2 times in lane 1 of the thick and thin girders, respectively. The difference in shielding effectiveness between the porosities is marginal in the thick girder, but the 25% porosity wind barrier exhibits superior performance in the thin girder.

However, increasing the hole spacing of the bottom part of the wind barrier (50-H-DS) and combining the barriers with a single flap (50-H-DS/H+F) results in an increased wind velocity below the height of about 2.5 m in the windward lanes of both girders, which may affect the driving of light and medium vehicles. Above this height, a significant reduction in wind speed is observed, crucial for enhancing driving safety, particularly for larger vehicles which are more prone to instability.

In Figure 4.31, for the 2.5-m high wind barrier (50-H-2.5m) installed on the thin girder, its shielding performance under about 2 m is slightly less effective compared to the 3-m high barrier but is comparable to that of the combination with the flap (50-H+F). Additionally, its effective shielding height is lower than that of other barriers.

Moreover, mean and maximum wind velocities above the height of light vehicles (1.6 m) in almost all lanes, except lanes 1 and 2 of the thin girder, of wind barriers with a 50% porosity ratio show consistent shielding performance.

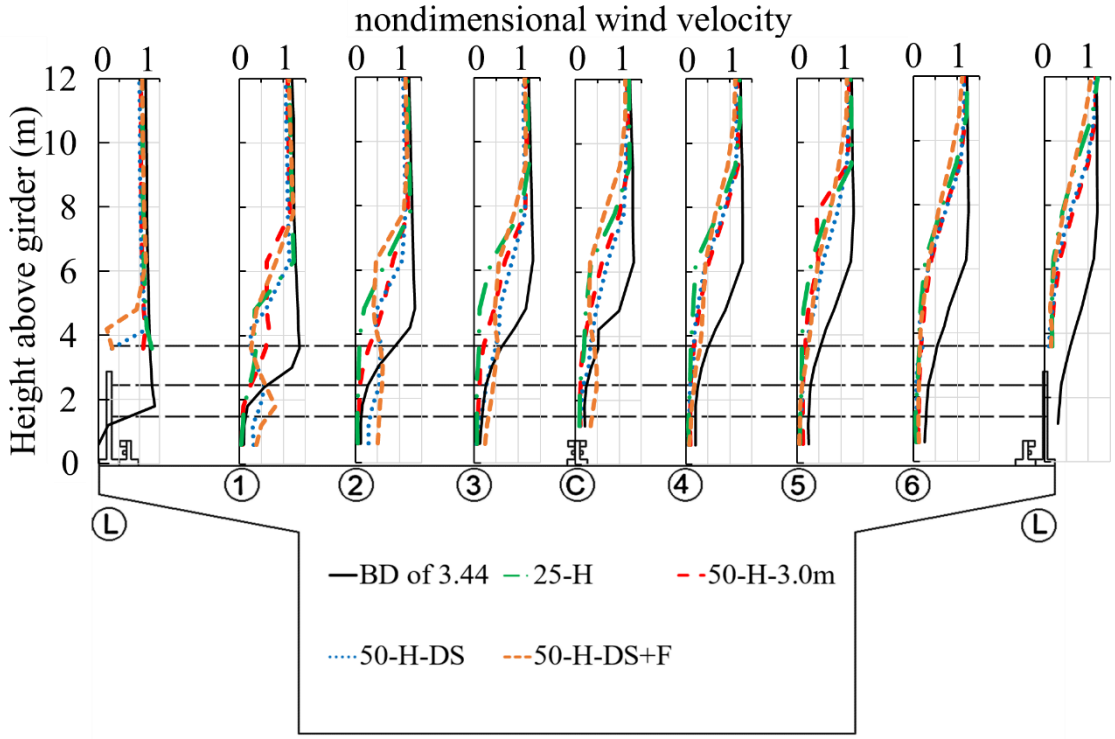

(a) Thick girder (BD of 3.44)

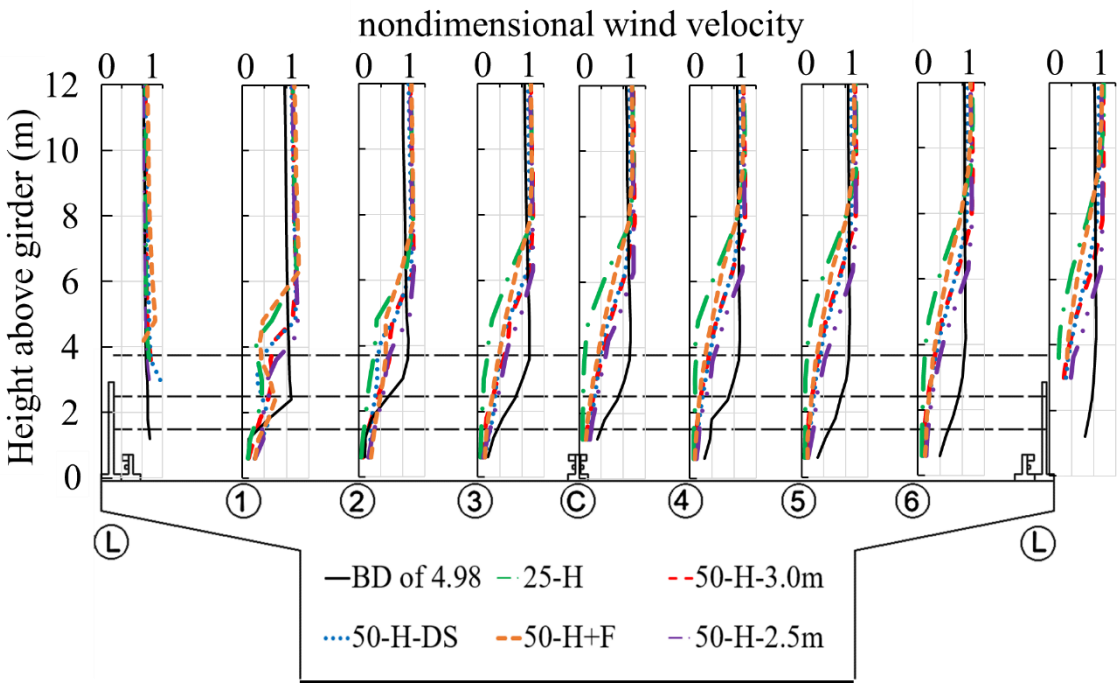

(b) Thin girder (BD of 4.98)

Figure 4.31 Mean wind velocity profile above both girders with different wind barriers

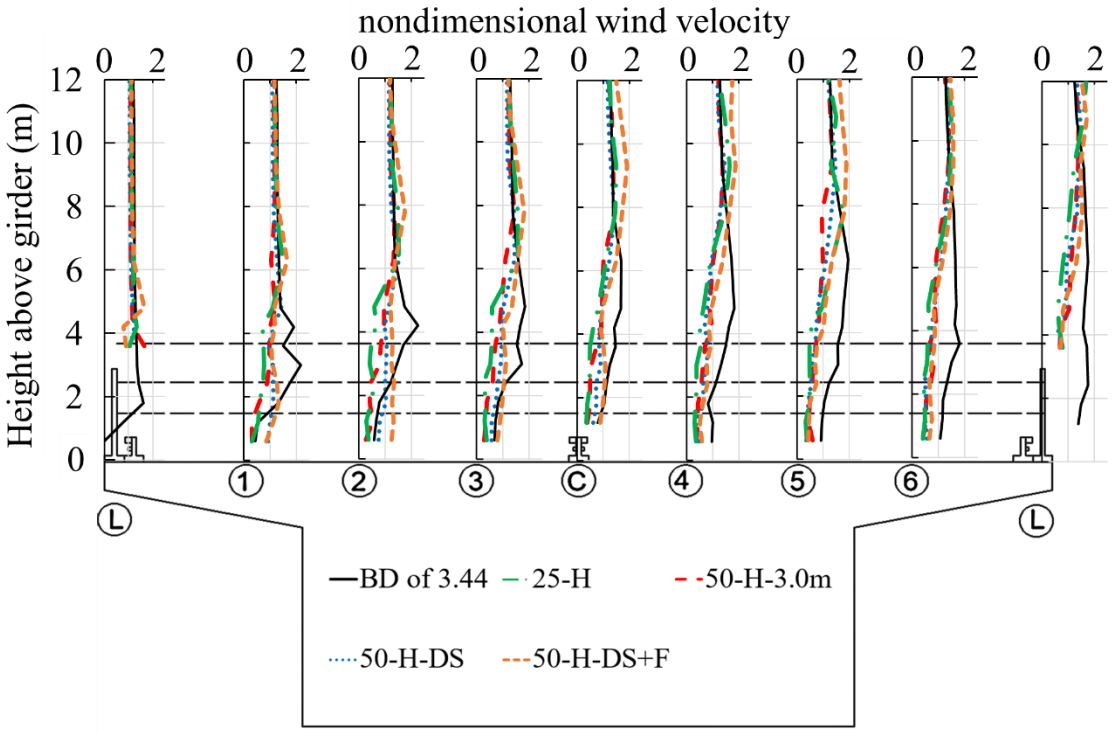

(a) Thick girder (B D of 3.44)

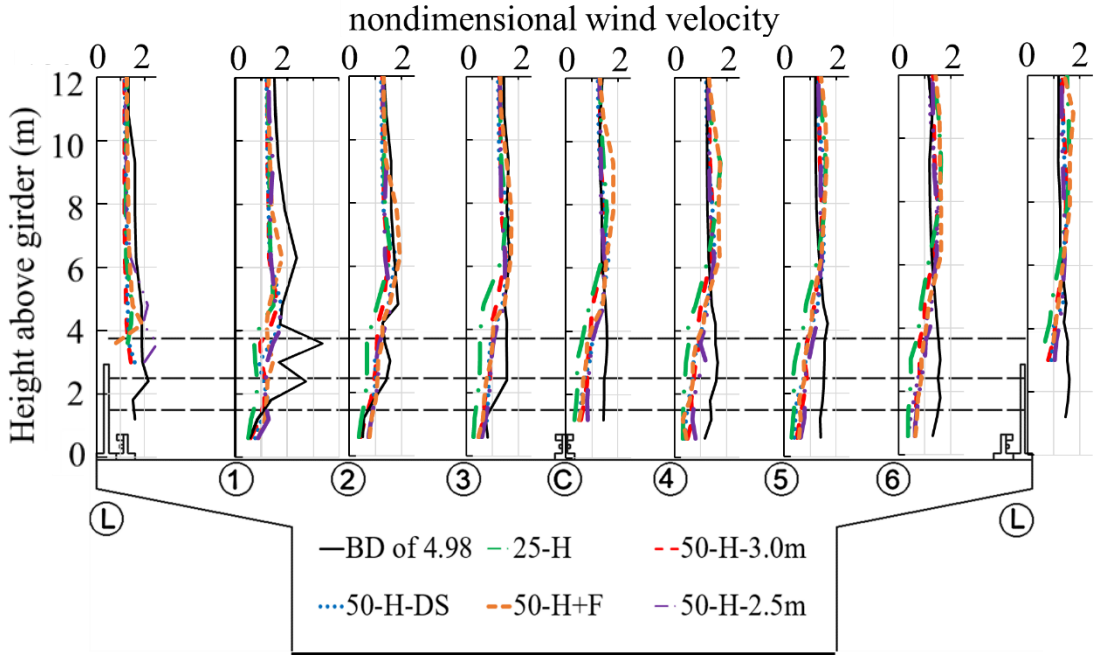

(b) Thin girder (BD of 4.98)

Figure 4.32 Maximum wind velocity profile above both girders with different wind barriers

4.6 Concluding remarks

This section has systematically investigated the impacts of various wind barrier parameters, including hole schemes, porosity ratios, heights, installation method, and vertical vortex-induced vibration (VIV) countermeasures, on the aerodynamic responses and wind flow field of two bluff box girders with different side ratios of 3.44 (thick girder) and 4.98 (thin girder). The study utilized comprehensive approaches including aerodynamic force measurements, two-degree-of-freedom free vibration tests, and wind velocity measurements. The principal findings are summarized as follows:

1) Installation of wind barriers significantly increased the drag coefficient and the amplitude of vertical VIV but decreased the critical wind velocity for torsional flutter resulting in detrimental effects on the aerodynamic performance of both girders. However, most wind barriers with a porosity ratio of 50% and their modifications had the benefit of stabilizing torsional VIV under a wind velocity of 80 m/s in both girders.
2) The proposed countermeasures such as enlarging the hole space at the lower part of a wind barrier and combining wind barriers with flaps, effectively reduced the vertical VIV amplitude in the thick girder. This modification also raised the onset wind velocity for vertical VIV, substantially improving traffic regulation during strong winds. Conversely, similar measures did not reduce such vibrational amplitudes in the thin girder, even when the height of the wind barrier was reduced from 3.0 m to 2.5 m.
3) Wind barriers significantly altered the flow fields above both girders. For the thin girder, the flow pattern transformed from reattached to detached, while for the thick girder, the flow pattern remained the same. Additionally, wind barriers reduced wind velocity and changed turbulence intensity in both girders. The variations in turbulence intensity near the top surface of the girders were directly related to vortex formation and shedding, significantly influencing vertical VIV. An increase in turbulence intensity due to countermeasures in the thick girder tended to reduce the peak vertical VIV amplitude. In contrast, a decrease in turbulence intensity caused by 25% and 50% porosity ratio wind barriers, as well as countermeasures in the thin girder, tended to amplify the vibrational amplitude compared to the bare deck cases.
4) Mean and maximum wind speeds were relatively higher in the thin girder compared to the thick girder, indicating that girders with larger side ratios are more susceptible to vehicle driving safety issues under strong crosswind conditions. Therefore, the strategic placement of wind barriers on bridges with varying girder depths is crucial for cost and time effectiveness. This approach also helps limit the detrimental effects of wind barriers on the aerodynamic performance of the bridge. For instance, installing a wind barrier only at the mid-span of the bridge could be a practical solution.
5) In most traffic lanes, wind barriers considerably reduced the mean and maximum wind speeds as well as turbulence intensity over the driving areas of both girders, particularly at the windward lanes. Although the countermeasures slightly increased wind speeds near the girder surfaces at heights affecting light vehicles, they still provided significant benefits for the stability of large vehicles which are more susceptible to strong crosswinds.

6) Among the various parameters of wind barriers, the porosity ratio is particularly significant due to its dual role in minimizing bridge instability and enhancing driving safety for vehicles on both girders. Higher porosity ratios reduced the vertical VIV amplitude and increased the critical wind velocity for torsional flutter, although at the cost of diminished barrier shielding efficiency compared to lower porosity ratios. Conversely, the orientation of the hole scheme, whether horizontal or vertical directions, had a negligible effect on the aerodynamic performance of the thick girder. Furthermore, the partial installation of wind barriers above the handrail proved practical, especially for bridges with limited installation space, as it demonstrated improved aerodynamic performance for the thick girder without significantly affecting the thin girder.

Given these findings, a wind barrier with a 50% porosity ratio emerges as an effective compromise contributing to minimal impacts on the aerodynamic performance of the bridge with efficient wind speed reduction. Such barriers could be optimally placed around the center span of varying-depth girder bridges. This area, characterized by a lower side ratio, is more exposed to higher wind speeds, thus increasing the risk to vehicle driving safety compared to the girder sections near the piers, which have a larger side ratio and are less affected by wind.

Furthermore, the study revealed that the aerodynamic responses of both girders to wind barriers could either stabilize or destabilize the amplitude of vertical VIV. These effects vary significantly with the specific configurations of the bridge girders and the design of the wind barriers. Therefore, a detailed understanding of the mechanisms through which wind barriers influence vertical VIV is crucial. Such knowledge is essential for developing guidelines for wind barrier design that enhance both the structural stability of bridges and the safety of vehicles under windy conditions will be discussed in detail in Section 5.

References

Fujino, Y., Yoshida, Y., 2002. Wind-Induced Vibration and Control of Trans-Tokyo Bay Crossing Bridge. Journal of Structural Engineering 128, 1012–1025. https://doi.org/10.1061/(ASCE)0733-9445(2002)128:8(1012)

Kaneko, R., Kim, H., Kimura, K., Katsuchi, H., Fujino, Y., 2022. Characteristics of crosswind based on field measurement using a moving vehicle on the Trans-Tokyo Bay Bridge. Wind Engineering Research 27, 207–216. https://doi.org/10.14887/windengresearch.27.0_207

Kim, H., Fujino, Y., Katsuchi, H., Siringoringo, D.M., Yamada, H., Ohkoshi, S., 2021. Computational fluid dynamics simulation and stability analysis of vehicle on bridge under strong winds. Journal of Japan Society of Civil Engineers, Ser. A1 (Structural Engineering & Earthquake Engineering (SE/EE)) 77, 107–120. https://doi.org/10.2208/jscejseee.77.1_107

Kim, H., Murata, R., Kaneko, R., Kimura, K., Katsuchi, H., 2023. Analysis of Crosswinds on the Box-girder Bridge with Variable Girder Height. Summaries to Technical Papers of Annual Meeting, Japan Association for Wind Engineering 2023, 119. https://doi.org/10.14887/jaweam.2023.0_119

Lin, X., Lin, B., Xia, D., Lin, L., Yuan, Z., 2022. Effects of Wind Barriers on Wind Fields and Vehicle Stability on Bridges. Atmosphere 13, 318. https://doi.org/10.3390/atmos13020318

Sarwar, M.W., Ishihara, T., 2010. Numerical study on suppression of vortex-induced vibrations of box girder bridge section by aerodynamic countermeasures. Journal of Wind

Engineering and Industrial Aerodynamics 98, 701–711. https://doi.org/10.1016/j.jweia.2010.06.001
Simiu, E., Miyata, T., 2006. Design of Buildings and Bridges for Wind: A Practical Guide for ASCE-7 Standard Users and Designers of Special Structures, 1. st. ed. Wiley, New York.
Simiu, E., Yeo, D., 2019. Wind Effects on Structures: Modern Structural Design for Wind, 1st ed. Wiley. https://doi.org/10.1002/9781119375890
Wang, J., Sato, M., Katsuchi, H., Tamura, H., 2022. Experimental investigation on effects of wind barrier on aerodynamic stability of bridge and vehicle on bridge. Wind Engineering Research Papers No. 27.
Yoshida, Y., Fujino, Y., Tokita, H., Honda, A., 1999. Wind tunnel study and field measurement of vortex-induced vibration of a continuous steel box girder in Trans-Tokyo Bay Highway. Doboku Gakkai Ronbunshu 1999, 103–117. https://doi.org/10.2208/jscej.1999.633_103
Zhang, J., Zhang, M., Li, Y., Qian, Y., Huang, B., 2020. Local wind characteristics on bridge deck of twin-box girder considering wind barriers by large-scale wind tunnel tests. Nat Hazards 103, 751–766. https://doi.org/10.1007/s11069-020-04010-y

CHAPTER 5
Mechanism of vertical vortex-induced vibration of a bluff box girder

5.1 Introduction

This chapter explores the mechanisms of vertical vortex-induced vibration (VIV) in a bluff-box rectangular girder with a side ratio of 5.00, including its attachment with a fairing which serves as a stabilization countermeasure, focusing on the influence of various wind barrier parameters and countermeasures for both stabilization and destabilization effects on the girder. The decision to adopt this girder is based on the challenges encountered in stabilizing vertical VIV in a thin girder with a side ratio of 4.98, as discussed in Chapter 4, while successful mitigation was achieved in a thick girder with a side ratio of 3.44 by countermeasures.

Section 5.2 provides a detailed description of the sectional models of the bluff box girder and its fairing attachment. This section also introduces various wind barrier models with different parameters, such as porosity ratios and heights, which are critical parameters, and countermeasures that succeeded in stabilizing vibrations in the thick girder but failed in the thin girder. Additionally, a new proposed countermeasure for vertical VIV, the triangular bar member wind barrier, is also detailed.

Section 5.3 discusses the vertical aerodynamic response of the girder and its fairing attachment, including the effects of wind barriers and the effectiveness of the proposed countermeasures in stabilizing vertical VIV.

In Section 5.4, this chapter delves into how wind barriers and proposed countermeasures impact the mechanisms of vertical VIV in the bluff girder with fairing through the interplay between pressure distributions and the mean flow field around the girder including both stabilizing and destabilizing mechanism.

Section 5.5 discusses the flow structure in the spanwise direction along the girder by the correlation coefficient of sectional fluctuating lift force.

Section 5.6 details the better stabilization performance in the case of the fairing attachment for some wind barrier cases compared to no fairing by the interplay between pressure distribution and mean wind flow field.

Finally, Section 5.7 summarizes the significant findings of this chapter regarding the vertical aerodynamic response and VIV mechanisms of the bluff girder and its fairing attachment. It discusses the implications of different wind barriers and countermeasures, offering valuable insights for the design of wind barriers for bluff box girders with a side ratio of 5.00.

5.2 Sectional and wind barrier models

5.2.1 Sectional models

Sectional models were utilized in the wind tunnel tests at a scale of 1:100 with a length of 1,250 mm. The bluff girder was designed to have a side ratio (*B/D*, where *B* is the width and *D* is the depth) of 5.00, closely aligning the side ratio of the thin girder which exhibited challenges in stabilizing vertical VIV due to complex aerodynamic interactions despite the implementation of various countermeasures as discussed in the previous Section 4. The bluff girder (BD), illustrated in Figure 5.1 (a), is used to elucidate the mechanisms of vertical VIV akin to bluff box girders in the previous Section 4. On the other hand, its fairing attachment (BD+FR) on both sides as shown in Figure 5.2 (b) represents a more aerodynamically efficient design, potentially mitigating issues such as high vertical VIV amplitudes and susceptibility to galloping. This feature is intended to reduce the aerodynamic instabilities often exacerbated by wind barriers, offering insights into how structural modifications can influence the overall aerodynamic performance of bridge girders.

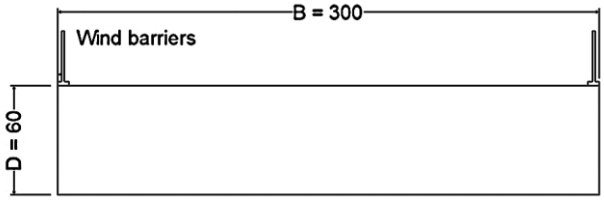

(a) bluff box girder (BD)

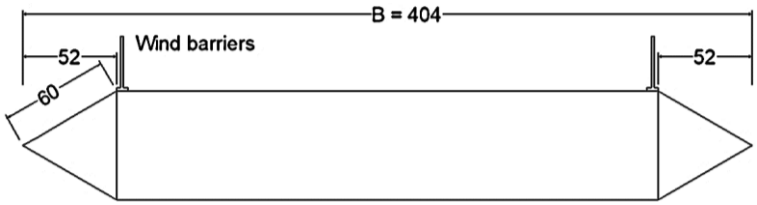

(b) bluff box girder with faring (BD+FR)

Figure 5.1 Sectional models (unit: mm; scale: 1/100)

5.2.2 Wind barrier models

Building upon the comprehensive consideration of various wind barriers and their impact on bridge aerodynamics and vehicle driving safety from Chapter 4. Some wind barriers as detailed in Figure 5.2 were selected for further study in this section. Initially, porosity ratios, defined by the ratio of open area to total area, of 25% and 50% (25-H and 50-H-3.0m, respectively) were chosen (Figures 5.2 (a) and (b)). The porosity ratio is a crucial parameter influencing the stability of bridges and the safety of vehicles traversing them.

Additionally, modifications to the 50% porosity ratio wind barrier were explored, such as reducing the height from 3.0 m to 2.5 m (50-H-2.5m, Figure 5.2 (c)). This alteration aims not only to limit the increase in drag force caused by wind barriers but also to reduce both the cost and time associated with their installation and maintenance. Countermeasures for stabilizing

vertical VIV were also assessed, including different spacing wind barriers whose hole space at the bottom part is larger and its combinations with single flaps (50-H-DS and +F, Figures 5.2 (d) and (e), respectively). These approaches demonstrated complex interactions with the side ratio of the girders, they were successful in reducing vertical VIV amplitude in the thick girders but less effective for the thin girders.

Furthermore, an innovative wind barrier incorporating triangular bar members (50-T, Figure 5.2 (f)) was introduced for study, the detail of two bar sections is shown in Figure 5.2 (g). Triangular shapes can optimize the flow dynamics around the barriers compared to traditional rectangular profiles by reducing aerodynamic drag and suppressing flow separation. This geometric benefit potentially results in improved aerodynamic performance and enhanced stability, offering a promising avenue for future aerodynamic enhancements in bridge design.

- Porosity ratios and heights

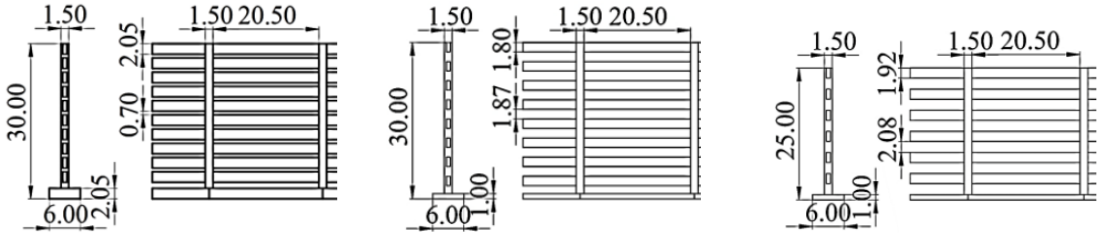

(a) 25-H (b) 50-H-3.0m (c) 50-H-2.5m

- Countermeasures

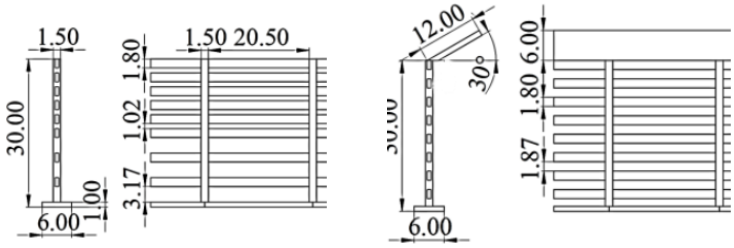

(d) 50-H-DS (e) 50-H+F

- Triangle bar members

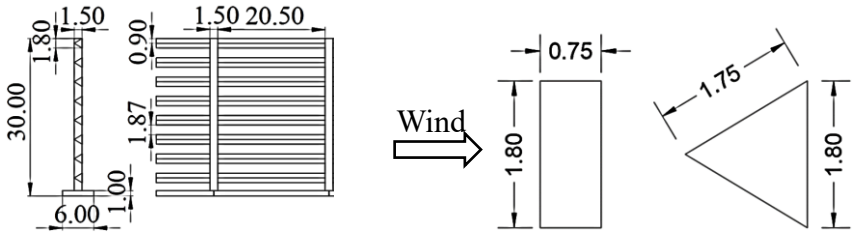

(f) 50-T (g) detail of two bar sections

Figure 5.2 Details of wind barrier models (unit: mm; scale: 1/100)

Notes: 1) 25 and 50 are porosity ratios.

2) 3.0m and 2.5m are heights.

3) H and T are rectangular and triangular bar members.

4) DS is the different spacing of the horizontal bars.

5) +F is combining wind barriers with a single flap.

5.3 Vertical aerodynamic responses of the girder

This section mainly explores how wind barriers influence the aerodynamic response of the bluff girder in the vertical direction at angles of attack $\alpha = 0°$ and $+3°$ which is the main target section of this research. Meanwhile, the aerodynamic response for fairing attachment to serve as a countermeasure to stabilize vertical VIV can be found in Appendix 2.

Table 5.1 summarizes the structural characteristic parameters for each case, demonstrating that the installation of wind barriers has a minimal impact on the structural characteristics of the girders. Consequently, the primary contribution to the aerodynamic performance of both girders is attributed to alterations in the wind flow field, specifically vortex shedding and its formation. These changes are a direct result of changes in the configuration of the bridge girder induced by the introduction of wind barriers.

The following subsections initially describe the effects of basic parameters of wind barriers encompassing porosity ratios and heights on the vertical VIV response. Then, the proposed countermeasures to stabilize the vertical VIV are discussed. In the aerodynamic response figures, the horizontal axis is the wind velocity, and the vertical axis displays the vibration amplitude (mm) on a real-world scale, more details can be found in Section 4.4.

Table 5.1 Structural characteristic parameters for free vibration test

Case	Bluff girder (BD)			Bluff girder with fairing (BD+FR)		
	m	δ	f	m	δ	f
Bare deck	4.06	0.03	3.83	4.26	0.03	3.71
25-H	4.12	0.03	3.80	4.31	0.03	3.68
50-H-3.0m	4.10	0.03	3.81	4.30	0.03	3.69
50-H-2.5m	4.10	0.03	3.81	4.30	0.03	3.68
50-T	4.11	0.03	3.81	4.31	0.03	3.68
50-H-DS	4.10	0.03	3.81	4.30	0.03	3.69
50-H+F	4.14	0.03	3.79	4.33	0.03	3.67

Notes: 1) m is mass (kg/m)

2) δ is damping (logarithmic decrement).

3) f is the natural frequency (Hz).

5.3.1 Effect of porosity ratios and heights

Figure 5.3 illustrates that when wind barriers are attached, the 25% porosity wind barrier (25-H) markedly heightens the VIV amplitude for both angles of attack by approximately 1.4 times and 2.4 times at $\alpha = 0°$, and by 1.3 times and 2.5 times at $\alpha = +3°$, respectively, relative to the 50% porosity wind barrier and the bare deck (50-H-3.0m and BD). In addition to the height of the wind barriers, both the 50% porosity wind barriers of 3.0 m and 2.5 m heights (50-H-3.0m and 2.5m) show almost identical vertical VIV response. Compared to the bare deck case (BD), they increase the vertical VIV amplitude approximately 2.0 times and 1.7 times with decreased corresponding wind velocity from approximately 25 m/s to 22 m/s and from 23 m/s to 20 m/s at $\alpha = 0°$ and +3°, respectively.

The result also reveals that the second mode of vibration, characterized as rolling vibration whose frequency differs from the natural frequency of the system as detailed in Section 4.4.2, manifests at both angles of attack with the onset wind velocity approximately from 26 m/s to 33 m/s. This rolling vibration is significantly amplified by wind barriers—more than 3.2 times and 1.3 times for $\alpha = 0°$ and +3°, respectively, compared to the bare deck.

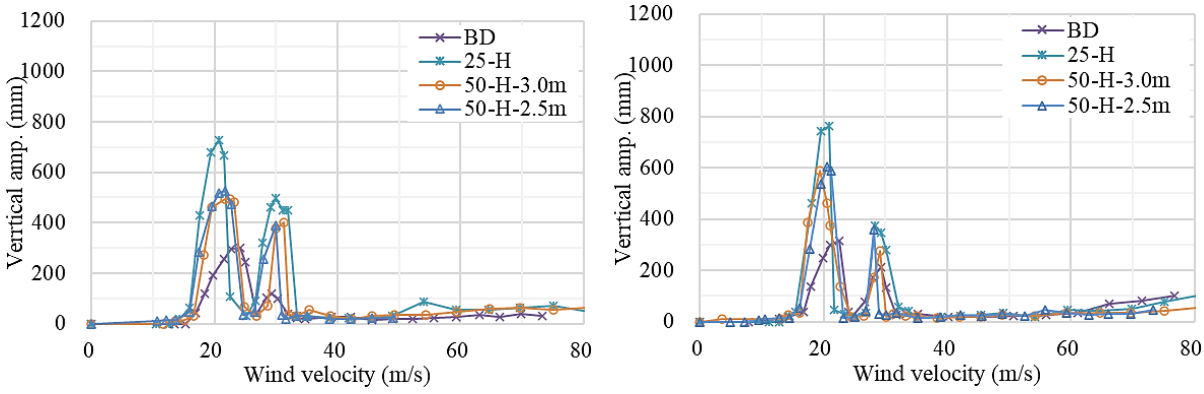

(a) $\alpha = 0°$ (b) $\alpha = +3°$

Figure 5.3Vertical aerodynamic response of the girder with basic parameter wind barriers

5.3.2 Effect of countermeasures

The countermeasures (50-H-DS and 50-H+F) that effectively stabilized the vertical VIV in the thick girder with a side ratio of 3.44, yet demonstrated limited effectiveness in the thin girder with a side ratio of 4.98 as detailed in the previous Chapter 4, have shown a similar influence on the bluff girder with a side ratio of 5.00, as illustrated in Figure 5.4. These countermeasures slightly outperform the standard wind barrier (50-H-3.0m) in reducing the VIV amplitude, decreasing it by approximately 1.2 times at $\alpha = 0°$ and further reducing it by 1.4 times at $\alpha = +3°$, though these reduced amplitudes are still higher than those amplitudes of the bare deck (BD).

The proposed triangular member wind barrier (50-T) has proven to be an effective countermeasure for stabilizing vertical VIV by achieving a comparable amplitude reduction

with that of the bare deck (BD) with a reduced amplitude of about 55% of the standard wind barrier with a rectangular bar member (50-H-3.0) at α = 0° (Figure 5.4 (a)). More notably, it lowers the amplitude to about 30% and 50% of the standard wind barrier and the bare deck at α = +3° with a relative onset wind velocity to the bare deck resulting in no reduction in this wind velocity compared to other wind barriers that might affect the traffic regulation during the strong crosswinds (Figure 5.4 (b)).

Additionally, the countermeasures (50-H-DS and 50-H+F) are effective in reducing the amplitude of rolling vibrations, which is the second mode of vibration, compared to the standard barrier for both angles of attack. Significantly, the triangular member wind barrier completely suppresses this vibration at α = +3°, as highlighted in Figure 5.4 (b).

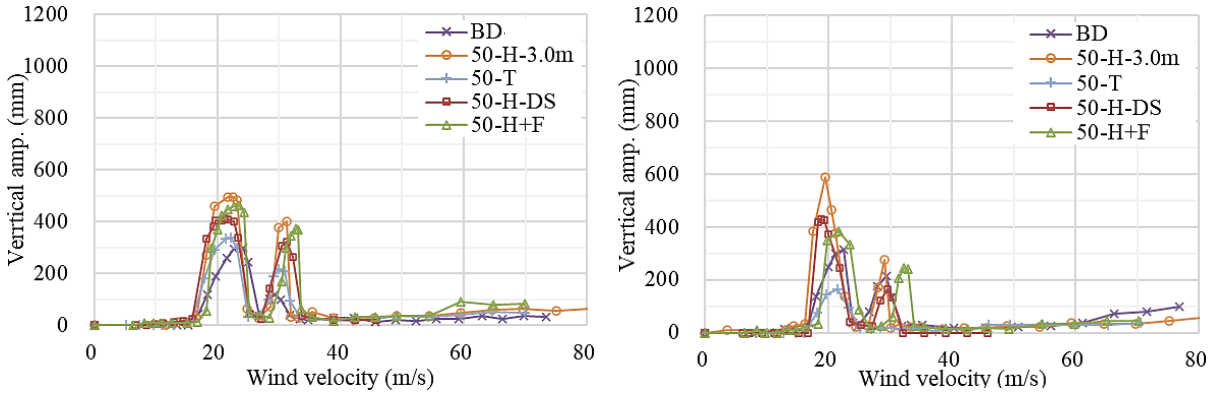

(a) α = 0° (b) α = +3°

Figure 5.4 Vertical aerodynamic response of the girder with countermeasures

The vertical VIV response of the bluff girder with a side ratio of 5.00 in this section and the thin girder with a side ratio of 4.98 in Section 4 affected by wind barriers, has demonstrated that this rectangular bluff girder can effectively serve as a fundamental bluff body for studying the mechanisms of vertical VIV relating to wind barriers.

Figure 5.5 concludes the peak vertical VIV amplitudes for the bluff girder (BD) and its fairing attachment (BD+FR) across various cases at an angle of attack of 0°. The x-axis categorizes the case names alongside a table detailing the peak amplitudes, while the y-axis quantifies these amplitudes. The findings underscore the significant role of flow interactions with the girder configuration and wind barriers in either stabilizing or destabilizing vertical VIV in specific cases.

In scenarios where the fairing is attached (BD+FR), this modification exhibits a limited capacity to stabilize vertical VIV. Notably, the installation of a wind barrier with 25% porosity (25-H) markedly exacerbates the vibrational amplitude, increasing it more than 3 times relative to the bare deck, indicating a more substantial impact compared to scenarios without fairing (BD). Conversely, the implementation of standard and triangular member wind barriers (50-H-3.0m and 50-T, respectively) enhances performance in stabilizing vertical VIV for this configuration, outperforming the no-fairing scenario. These barriers significantly reduce the amplitude by factors of 1.8 and 1.6, respectively, when compared to the bare deck (BD+FR).

However, other countermeasures, such as reduced height (50-H-2.5m), different spacing (50-H-DS), and combination with a flap (50-H+F), demonstrate only limited effectiveness in stabilizing vertical VIV, akin to results observed with the girder without the fairing. Therefore, the better VIV stabilization performance by fairing for certain cases of rectangular and triangular wind barriers with a 50% porosity ratio (50-H and 50-T, respectively) is discussed in Section 5.5.

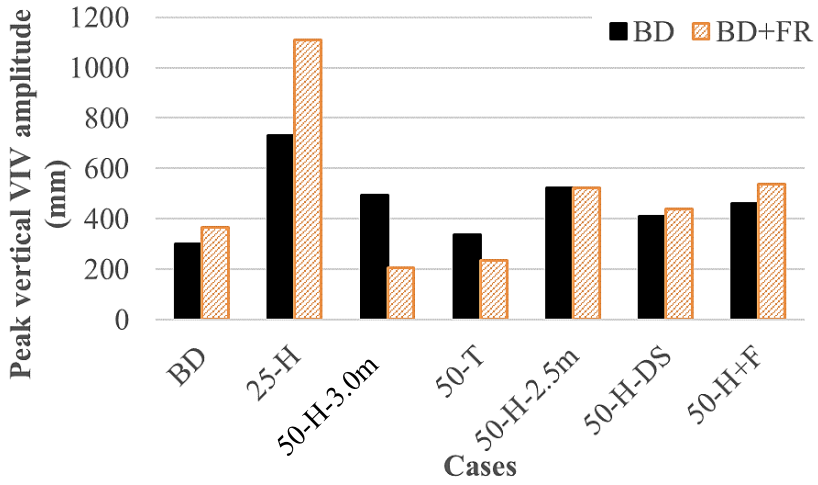

Figure 5.5 Peak vertical VIV amplitude of bluff girder (BD) and its fairing attachment (BD+FR)

5.4 Interplay between pressure distribution and mean wind flow field corresponding to VIV amplitude

This section comprehensively investigates the mechanisms of vertical VIV of the bluff girder relating to wind barriers, focusing on the interplay between the pressure distribution and the mean wind flow field around the girder. The insights aim to aid in the development of guidelines for wind barrier design, ensuring these structures not only mitigate adverse wind effects on vehicle driving safety but also enhance the overall aerodynamic performance of bridges.

Section 5.4.1 provides a foundational understanding of the mechanism of vertical VIV of the bluff girder without wind barriers. Following this, Section 5.3.2 delves into how wind barriers with varying parameters—such as 25% and 50% porosity ratios (25-H and 50-H-3.0), and a newly proposed triangular bar member wind barrier (50-T) that successfully reduces vibrational amplitude, as discussed in Section 5.2.2—affect the mechanism. Additionally, this section also clarifies the mechanism of the countermeasures and reduced high wind barrier (50-H-2.5m) on the bluff girder, including a wind barrier with different spacing (50-H-DS) that reduced the vibrational amplitude and a combination with a flap (+F) that successfully stabilized such vibrations in the thick girder with a side ratio of 3.44, but failed to stabilize vibration in the thin girder with a side ratio of 4.98 and the girder in this study with a side ratio of 5.00.

The figures of pressure distribution provide the detail of the pressure coefficients around the girder. The x-axis represents the relative distance at each side of the girder, normalized by its depth (*D*). The specific sides include the upstream (UP), top (T), downstream (DO), and bottom (BO) sides as shown in Figure 5.6. Concurrently, the flow field figures illustrate the mean wind flow streamlines alongside velocity contours on both the top and bottom sides of the girder, the approaching wind velocity of 2,000 mm/s was used to normalize the wind velocity. The x-axis for these flow field figures is also normalized by the girder's depth (*D*), consistent with the scaling used in the pressure distribution diagrams to facilitate a straightforward comparison.

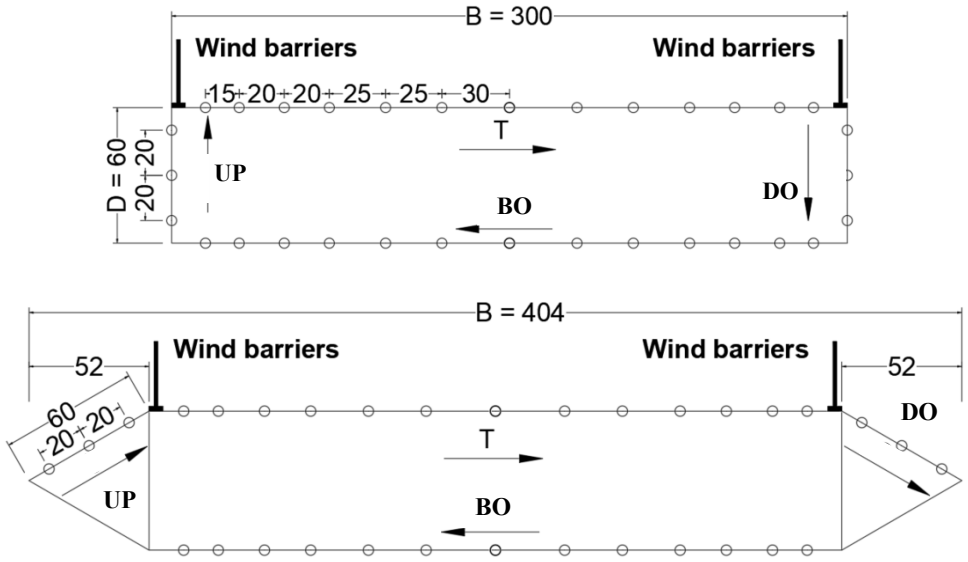

Figure 5.6 Description of pressure distribution

5.4.1 Interplay between pressure distribution and mean wind flow field of the girder without wind barriers

Figure 5.7(a) reveals that the upstream (U) side of the girder experiences high positive mean pressure values at the leading edge, indicative of high stagnation pressure. This high pressure represents the point of initial airflow impact and corresponds to the flow separation at the leading edge of the girder as observed in Figure 5.8(a). Subsequently, this value drops sharply and becomes negative as the flow separates and transitions over the top (T) and bottom (BO) sides of the girder. This separation initiates a strong separated shear layer that reattaches at a normalized distance of approximately 3.0, as in Figure 5.8(a), the point where the mean pressure coefficients begin to recover, gradually increasing as they approach the trailing edge, as shown in Figure 5.7(a). Notably, beyond this reattachment point, there is a significant large fluctuating pressure, as demonstrated in Figure 5.7(b).

The areas of low mean pressure coefficient correspond to regions of pronounced flow separation, as evidenced by the change in streamline direction and flow deceleration seen in Figure 5.8(a). Additionally, the motion of the separated shear layer at the trailing edge zone where the flow reattaches corresponding to the high-pressure fluctuation at this zone implies a critical contributor to vertical VIV that might impart oscillatory forces on the structure, possibly due to the vortex shedding that occurs at these points of flow separation and reattachment.

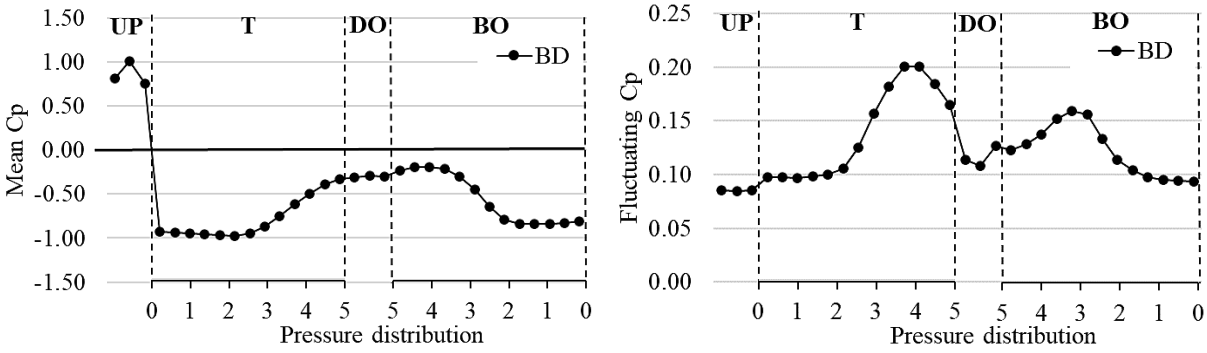

(a) Mean pressure coefficient (b) Fluctuating pressure coefficient

Figure 5.7 Mean and fluctuating pressure coefficient distribution of the bluff girder (BD)

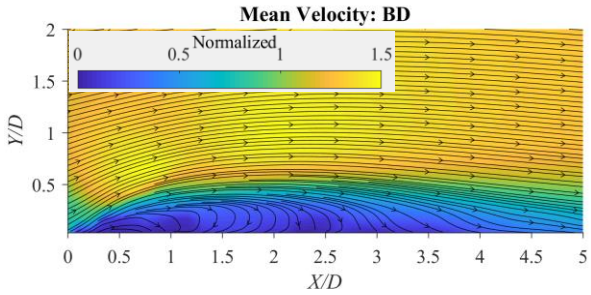

Figure 5.8 Mean flow field of the bluff girder (BD)

5.4.2 Interplay between pressure distribution and mean wind flow field of the girder with wind barriers

This section delves into the VIV mechanism of the girder affected by wind barriers. The rectangular bar member wind barriers (25-H and 50-H-3.0m) destabilized such vibration meanwhile the reduced height (50-H-2.5m) showed almost a consistent trend with the 3.0 m height. Although the countermeasures (50-H-DS and 50-H+F) reduced the vibration amplitude compared to the normal wind barrier (50-H-3.0m) it is still higher than the bare deck. Importantly, the triangular wind barrier (50-T) successfully reduced the amplitude, the details of the aerodynamic response are discussed in Section 5.3 and shown in Figure 5.5.

The introduction of wind barriers significantly alters the flow characteristics on the top side (T) of the girder by shifting the separation point from the edge of the girder to the top of the wind barriers (Figures 5.11 (a) to 5.13 (a)). For rectangular wind barriers with porosity ratios of 25% (25-H) and 50% (50-H-3.0m), the primary effect is the promotion of shear layer separation, leading to a detached flow type (as shown in Figures 5.11 (a) and 5.12 (a)). In the case of the 25-H barrier, this shift in the shear layer from its original *Y/D* position of approximately 0.5 to between 0.6 and 1.2 results in quicker pressure recovery and slightly increased pressure fluctuations near the leading edge of the girder.

Moreover, this transformation in the flow pattern diminishes reattachment at the trailing edge of the girder, reducing pressure fluctuations in this region to be smaller than those observed in the bare deck (Figure 5.9 (b)).

In contrast, the triangular wind barrier (50-T), which effectively reduces VIV amplitude, benefits from its more streamlined shape compared to the rectangular bar members. The 50-T allows smoother flow passage with minimal disturbance, leading to flow acceleration and the elimination of the recirculation zone observed in other cases. This results in a more homogeneous flow field, as evidenced by the direction of the mean streamline (Figure 5.13 (a)) resulting in the most rapid mean pressure recovery and the lowest pressure fluctuations in the trailing-edge zone compared to all other cases (Figure 5.9). This reduction in pressure fluctuation is likely a key factor in the successful suppression of VIV amplitude in the 50-T configuration caused by less energy of wind flow feeding to the vibration of the girder.

Wind barriers not only influence the flow over the top side of the girder but also have a significant impact on the bottom side. The mean pressure distribution on the upstream side (UP) of the girder is notably altered by the presence of wind barriers as shown in Figure 5.9 (a). Specifically, the pressure near the bottom part of the girder is reduced by more than 1.16 times, while the pressure near the upper part increases by more than 1.13 times compared to the bare deck. These effects are particularly pronounced with the 25-H barrier, which has the lowest porosity ratio behaving almost like a solid wall.

The changes in pressure distribution on the upstream side suggest a shift in the stagnation point, which might be attributed to the modification of the effective depth of the girder caused by the installation of the wind barriers. This shift in the stagnation point directly influences the flow behavior on the bottom side (BO) of the girder.

On the bottom side (BO) as shown in Figures 5.11 (b) and 5.12 (b), the presence of the wind barriers promotes the shear layer separation, causing it to detach more aggressively. The shear layer, which is originally positioned around $Y/D = 0.5$ in the bare deck case, is shifted to a higher position due to the influence of the barriers. Additionally, the recirculation zone on this side might be intensified leading to a significant reduction in mean pressure (Figure 5.9 (a))—by more than twice that of the bare deck with a notable increase in pressure fluctuations (Figure 5.9 (b)) at the trailing edge, which might be a critical factor in amplifying VIV.

The increased fluctuating pressure on the bottom side is a key contributor to the elevated VIV amplitude observed when wind barriers are present. The intensified recirculation and enhanced shear layer separation create conditions that feed more energy into the vibration, exacerbating the VIV response of the girder.

In contrast, the triangular wind barrier (50-T) limits the mean pressure reduction on the bottom side compared to the rectangular wind barriers as shown in Figure 5.9 (a). Moreover, this wind barrier maintains pressure fluctuations at levels comparable to those of the bare deck (Figure 5.9 (b)). This minimal disturbance to the flow on the bottom side, combined with the homogenized flow on the top side, plays a crucial role in limiting the overall vibration. The more streamlined flow associated with the 50-T barrier possibly reduces the energy available to sustain VIV, thereby contributing to the lower VIV amplitude observed with this configuration.

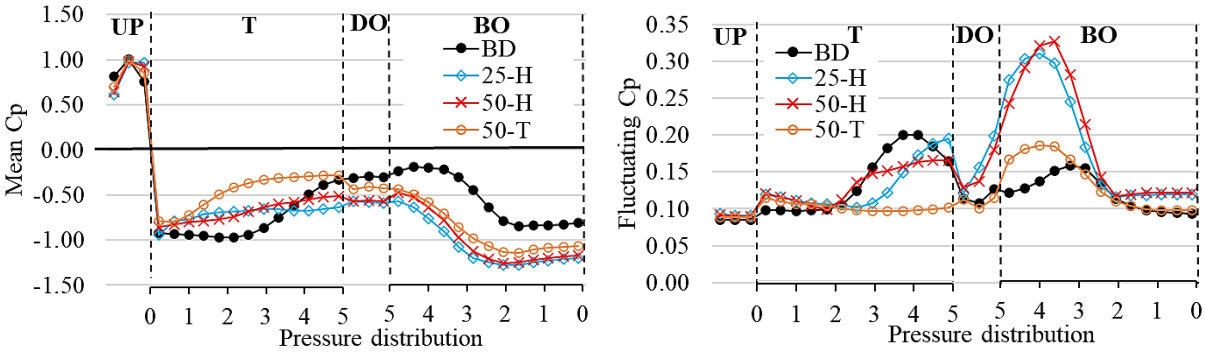

(a) Mean pressure coefficient (b) Fluctuating pressure coefficient

Figure 5.9 Mean and fluctuating pressure coefficient distribution of the bluff girder (BD) with wind barriers

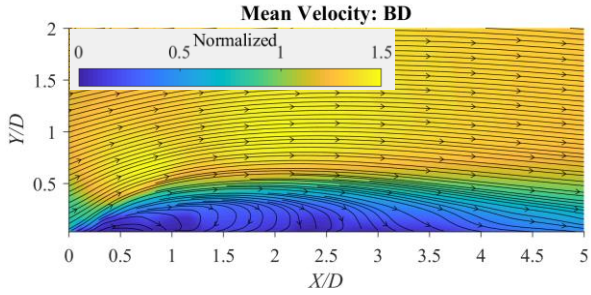

Figure 5.10 Mean flow field of the girder (BD)

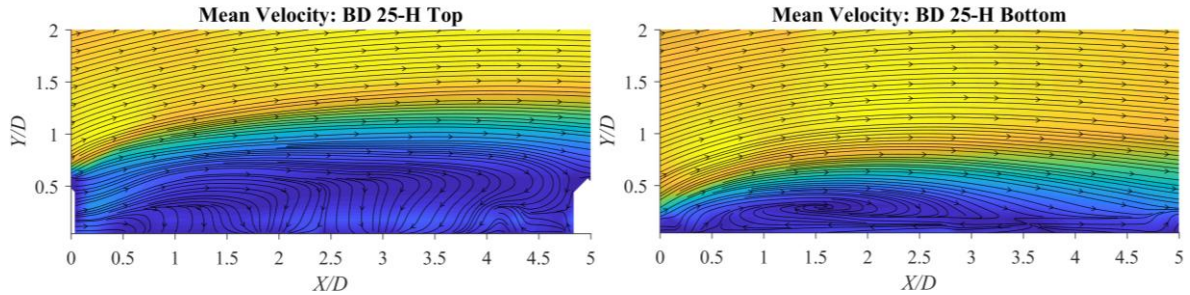

(a) Top side (b) Bottom side

Figure 5.11 Mean wind flow field of the bluff girder (BD) with 25-H

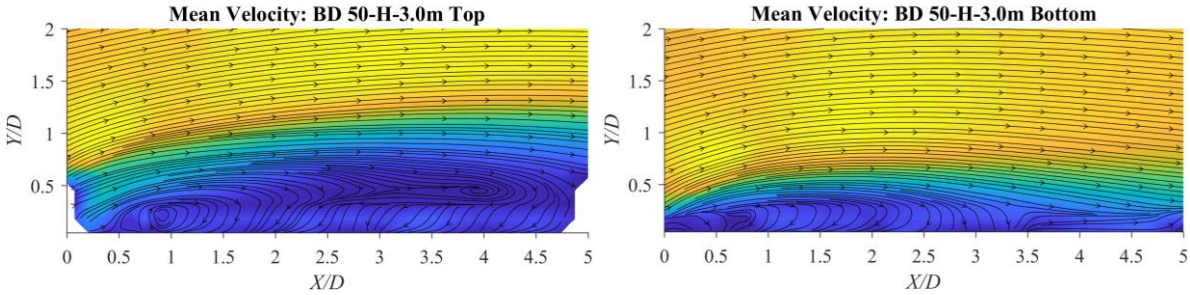

(a) Top side (b) Bottom side

Figure 5.12 Mean wind flow field of the bluff girder (BD) with 50-H-3.0m

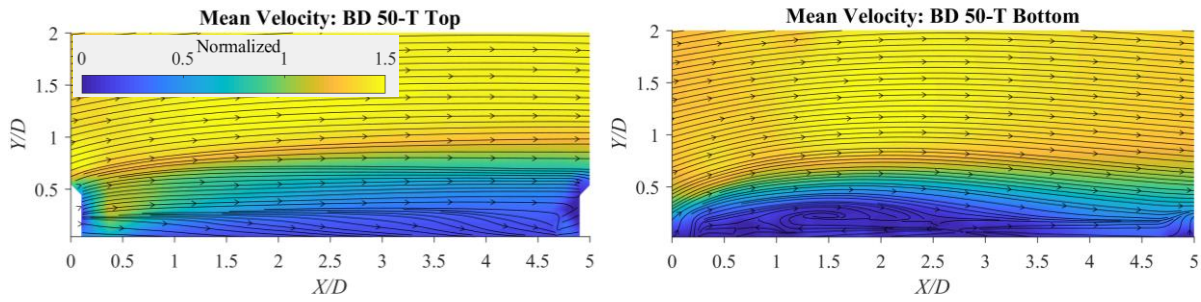

(a) Top side (b) Bottom side

Figure 5.13 Mean wind flow field of the bluff girder (BD) with 50-T

The 2.5 m high wind barrier (50-H-2.5m) maintains a consistent VIV amplitude with the 3.0 m high barrier (50-H-3.0m) due to the almost identical mean flow field and pressure distribution between the two cases, with only minor differences observed. On the top side (T), while the reduced height wind barrier slightly diminishes its promotion of shear layer separation compared to the 3.0 m barrier, the overall flow patterns remain nearly the same. However, as shown in Figure 5.15(a), the flow recirculation near the girder's surface is more pronounced and stronger in the 2.5 m case. This results in a larger mean pressure reduction and greater pressure fluctuations, particularly in the trailing-edge zone, though still comparable to those observed with the 3.0 m barrier. These increased pressures on the top side compensate for the reduced mean pressure and fluctuations at the leading-edge zone on the bottom side (BO) which might be attributed to the shifting of the flow reattachment further toward the leading edge in the 2.5 m case (Figure 5.15(b)), leading to a consistent VIV amplitude despite the slightly altered flow dynamics.

In the case of countermeasures that reduce the vibration amplitude by 1.20 times for the different spacing wind barrier (50-H-DS) and by 1.07 times for the wind barrier combined with a flap (50-H+F), compared to the standard 3.0 m wind barrier (50-H-3.0m), the aerodynamic modifications on both the top and bottom sides of the girder play a critical role.

On the top side (T), as seen in Figures 5.16(a) and 5.17(a), the different spacing wind barrier (50-H-DS) has a less pronounced effect on promoting shear layer separation, while the combination with a flap (50-H+F) shows a more aggressive promotion of shear layer separation compared to the normal wind barrier. Despite the variations in shear layer separation, both countermeasures lead to distinct flow recirculation patterns near the girder surface, characterized by accelerated flow at the leading edge and a reduced height of flow recirculation to approximately $Y/D = 0.5$. This contrasts with the normal wind barrier, where recirculation occurs below $Y/D = 0.7$. These changes result in the most rapid mean pressure recovery and the smallest pressure fluctuations among the cases, as illustrated in Figure 5.14.

On the bottom side (BO), the 50-H-DS barrier shows relatively weaker shear layer separation and less intense recirculation (Figure 5.16(b)) compared to the normal wind barrier and its combination with a flap (50-H-3.0m and 50-H+F, as shown in Figures 5.12(b) and 5.17(b), respectively). This leads to smaller pressure fluctuations on the bottom side, although they remain higher than in the bare deck, as seen in Figure 5.14(b).

The overall aerodynamic effect is a balance between rapid mean pressure recovery with minimal pressure fluctuations on the top side and significant pressure reduction with reduced pressure fluctuation compared to the normal wind barriers (50-H-3.0m and 2.5m) but still higher than the bare deck on the bottom side. This balance contributes to the observed reduction in vibration amplitude, although it remains higher than that of the bare deck.

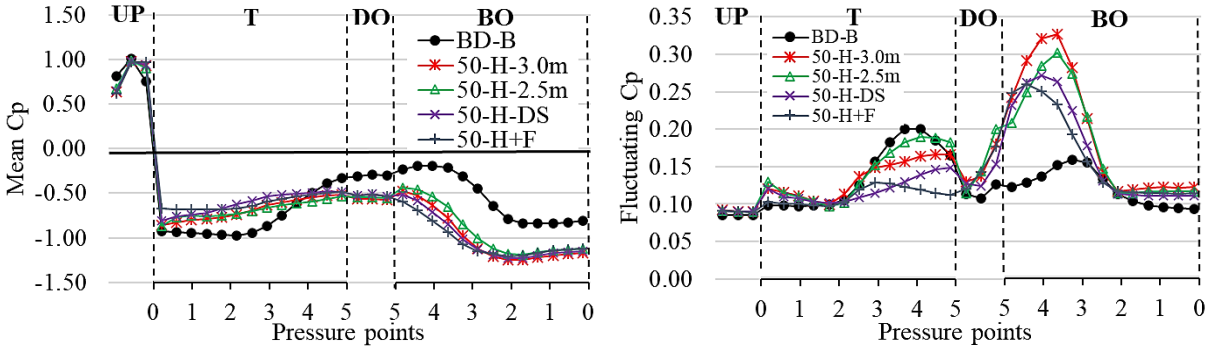

(a) Mean pressure coefficient (b) Fluctuating pressure coefficient

Figure 5.14 Mean and fluctuating pressure coefficient distribution of the bluff girder (BD) with countermeasures

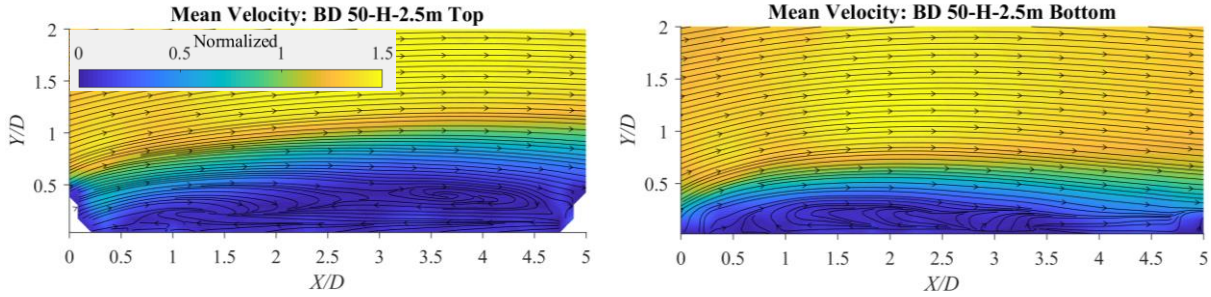

(a) Top side (b) Bottom side

Figure 5.15 Mean wind flow field of the bluff girder (BD) with 50-H-2.5m

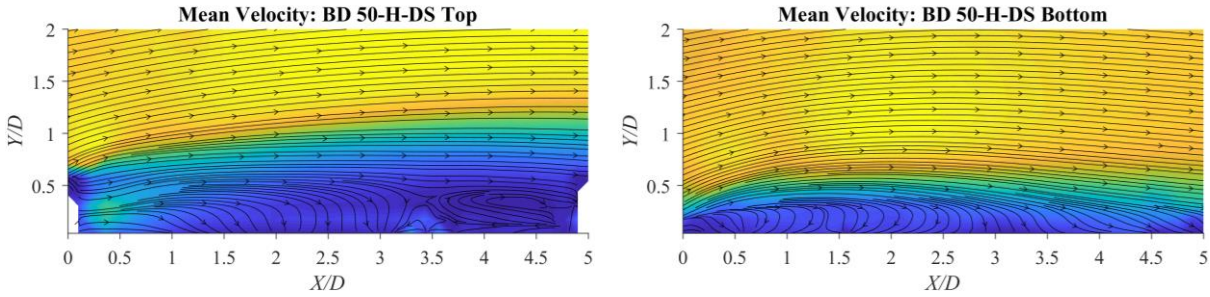

(a) Top side (b) Bottom side

Figure 5.16 Mean wind flow field of the bluff girder (BD) with 50-H-DS

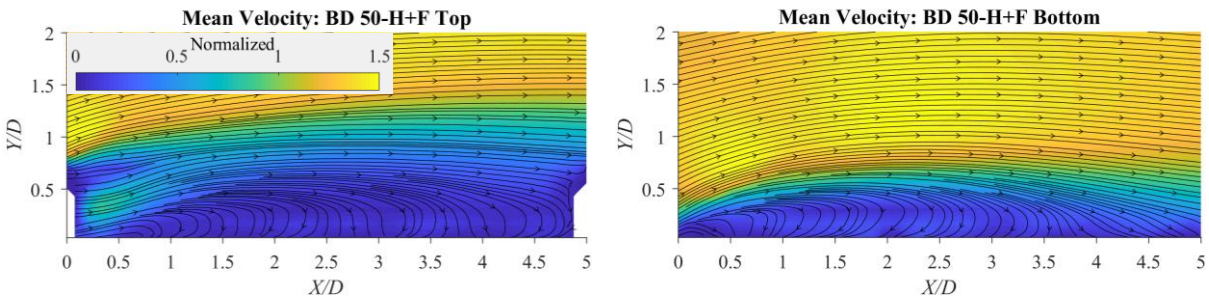

(a) Top side (b) Bottom side

Figure 5.17 Mean wind flow field of the bluff girder (BD) with 50-H+F

5.5 Spanwise correlation coefficient of sectional fluctuating lift force

In the previous Section 5.4, the focus was on the mean flow field and pressure distributions of a section in the streamwise direction and their implications for stabilizing and destabilizing VIV. This section shifts the focus to the spanwise direction by examining the correlation coefficients of the sectional fluctuating lift force between various sections of the girder as shown in Figure 5.18. Specifically, it analyzes the correlation between sections 1 and 2, 1 and 3, and 1 and 4, with normalized spanwise distances of $\Delta z/D$ equal to 0.5, 1.5, and 3.5, respectively. These correlations offer insights into the coherence of aerodynamic forces and the flow structure along the span of the girder, which is crucial for understanding the overall VIV behavior.

A higher correlation coefficient indicates that the flow structures are more uniform and more synchronized along the span, which in turn amplifies the fluctuating lift forces exerting energy into the vibration resulting in increased VIV amplitude, as observed in cases with rectangular wind barriers such as 25-H, 50-H-3.0m, and 50-H-2.5m. Particularly, the 25-H which has the largest vibration amplitude shows the highest correlation coefficient of more than 0.74 while the 50% porosity wind barriers (50-H-3.0m and 50-H-2.5m) show a relatively smaller correlation corresponding to the reduced vibration amplitude compared to the 25-H. Besides, an identical trend of the correlation between these two different high wind barriers agrees well with their consistent vibration amplitude as shown in Figure 5.5.

On the other hand, the introduction of countermeasures such as the different spacing wind barrier (50-H-DS) and the wind barrier combined with a flap (50-H+F) reduces the spanwise correlation to some extent lower than the normal wind barrier (50-H-3.0m) but still higher than the bare deck (BD) and the triangular wind barrier (50-T). These countermeasures disrupt the uniformity of the flow along the span, leading to a less synchronized flow structure. This reduction in correlation is associated with a decrease in VIV amplitude, though the amplitude remains higher than that observed for the bare deck. The countermeasures effectively scatter the flow structures along the span, which weakens the coherence of the lift forces and consequently reduces the vibration amplitude.

Finally, smaller correlation coefficients, as seen in the bare deck (BD) and triangular wind barrier (50-T) cases, indicate a more scattered and less synchronized flow structure along the

span resulting in smaller VIV amplitudes, as the fluctuating lift forces are less coherent and less capable of sustaining significant vibrations.

In summary, the spanwise correlation of sectional fluctuating lift forces provides valuable insights into the VIV behavior of the girder. Well-formed and synchronized flow structures along the span are associated with higher VIV amplitudes, while scattered and less synchronized structures lead to reduced vibrations, as proved by the increased spanwise correlation of 1.42 times by the 50-H -3.0m and only 1.14 times by 50-T compared to the bare deck case.

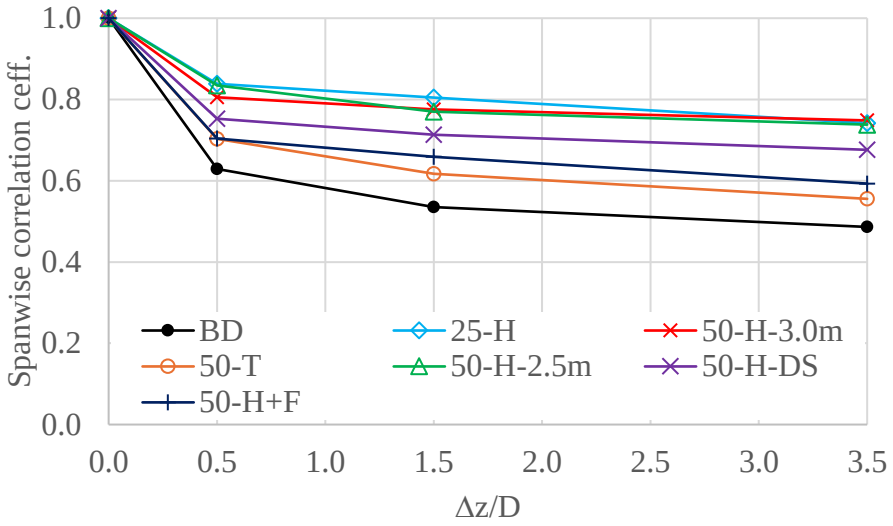

Figure 5.18 Spanwise correlation coefficient of the bluff girder (BD) with wind barriers

5.6 Effect of fairing attachment

This section comprehensively details the effect of fairing attachment on the mean flow field and pressure distribution of the girder without and with wind barriers corresponding to VIV response. Particularly, to focus on how the fairing attachment shows better VIV stabilization for some wind barrier cases of 50% porosity (50-H-3.0m and 50-T).

5.6.1 Effect of fairing attachment without wind barrier

Figure 5.20 shows that fairing shifts the flow reattachment point significantly forward from the trailing-edge zone of the girder (around $X/D = 3.5$) to the leading-edge zone (around $X/D = 0.5$). This upstream shift in reattachment eliminates the main recirculation zone resulting in a more homogeneous flow along the girder's cross-section after the reattachment.

This shift has several aerodynamic consequences. The most immediate is the rapid recovery of mean pressure in the leading-edge zone, where the flow reattaches. This area also experiences high-pressure fluctuations due to the turbulent nature of the reattaching flow. Conversely, the trailing-edge zone shows a marked decrease in pressure fluctuations when the fairing is present. This is because the flow, once reattached, remains stable, reducing the intensity of wake turbulence and, consequently, the pressure variations in the trailing-edge zone. These effects can be contrasted with the case without a fairing (BD), as shown in Figure 5.19.

The flow separation on the edge of the fairing and its subsequent reattachment in the leading-edge zone of the girder, characterized by quick pressure recovery and significant fluctuations, suggests the formation of a leading-edge vortex type which may contribute to the VIV in this scenario. The leading-edge vortex type induced by the fairing could play a crucial role in the dynamic response of the structure, potentially influencing both the amplitude and frequency of the VIV, depending on the strength and stability of this vortex.

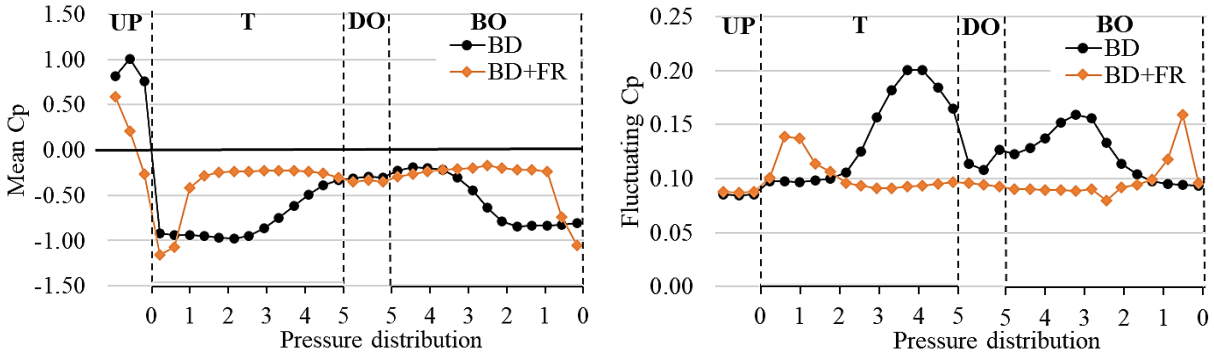

Figure 5.19 Mean and fluctuating pressure coefficient distribution of the bluff girder without fairing (BD) and with fairing (BD+FR)

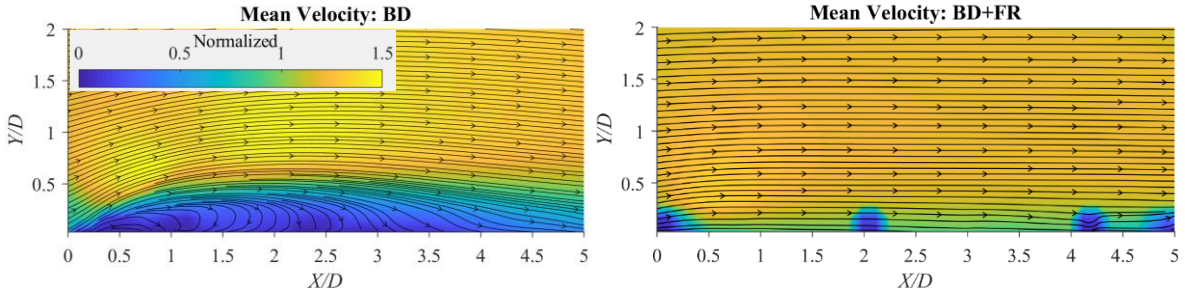

Figure 5.20 Mean wind flow field of the bluff girder without fairing (BD) and with fairing (BD+FR)

5.6.2 Effect of fairing attachment with wind barriers

In the presence of wind barriers and a fairing attachment, the aerodynamic behavior of the girder is significantly altered. The fairing effectively controls flow separation on the upstream (UP) side of the girder, promoting smoother flow. However, the wind barriers induce shear layer separation on the top (T) side of the girder as shown in Figures 5.22 (a) to 5.24 (a). This separation causes a transition in the flow from a leading-edge vortex type to a detached flow type. This results in diminishing flow reattachment at the leading edge, leading to increased mean pressure and reduced pressure fluctuations in this region, as illustrated in Figure 5.21.

For the 25% porosity wind barrier (25-H), which notably destabilizes the vibration, the dynamics are more pronounced. Due to its low porosity, this barrier behaves more like a solid wall rather than a porous one, effectively blocking the flow. This blockage significantly enhances shear layer separation on the top side (T), as depicted in Figure 5.22 (a). Although

the flow appears smooth at the leading-edge zone, recirculation occurs at the trailing edge, likely due to the blockage effect. This strong promotion of shear layer separation, leading to recirculation at the trailing edge, results in a significant reduction in mean pressure and an increase in pressure fluctuations in this region compared to other cases (Figure 5.21). Additionally, the 25% porosity wind barrier has a pronounced effect on the girder's bottom side (BO), where it greatly reduces mean pressure and amplifies pressure fluctuations. The combined effect of this wind barrier on both the top and bottom sides of the girder potentially amplifies the observed VIV amplitude.

In contrast, the 50% porosity wind barriers (50-H-3.0m and 50-T), which effectively stabilize the vibration, demonstrate different aerodynamic characteristics. As shown in Figures 5.23(a) and 5.24(a), these barriers accelerate the wind flow on the top side (T) of the girder, resulting in a more homogeneous flow that eliminates recirculation at the leading edge. This results in higher mean pressure and lower pressure fluctuations in this zone (Figure 5.21) compared to the bare deck. Unlike the 25-H barrier, these 50% porosity barriers do not exhibit recirculation at the trailing-edge zone on the top side of the girder, which leads to a smaller mean pressure reduction and lower pressure fluctuations compared to the 25-H. On the bottom side (BO), the differences in the wind flow field between the cases are less pronounced, as observed in Figures 5.22(b) to 5.24(b). However, these 50% porosity wind barriers show a limited impact on mean pressure reduction and pressure fluctuation amplification. The homogeneous flow on the top side, which increases mean pressure and reduces pressure fluctuations at the leading edge, combined with the minimal impact on mean pressure reduction and pressure fluctuation on the bottom side, likely contribute to the stabilization of VIV.

The fairing itself plays a crucial role in mitigating flow separation on the upstream side (UP) of the girder, allowing the wind to pass through the barriers more easily. This reduces the promotion of shear layer separation on the bottom side, significantly lowering pressure fluctuations in specific zones. The fairing also minimizes the gap between mean pressure reduction and pressure fluctuation amplification compared to cases without a fairing, where most wind barriers significantly amplify mean pressure reduction and pressure fluctuations on the bottom side of the girder. The smaller gaps in mean pressure reduction and pressure fluctuation amplification when some wind barriers are used with a fairing, compared to the no-fairing scenario, are key to achieving better VIV stabilization in this context.

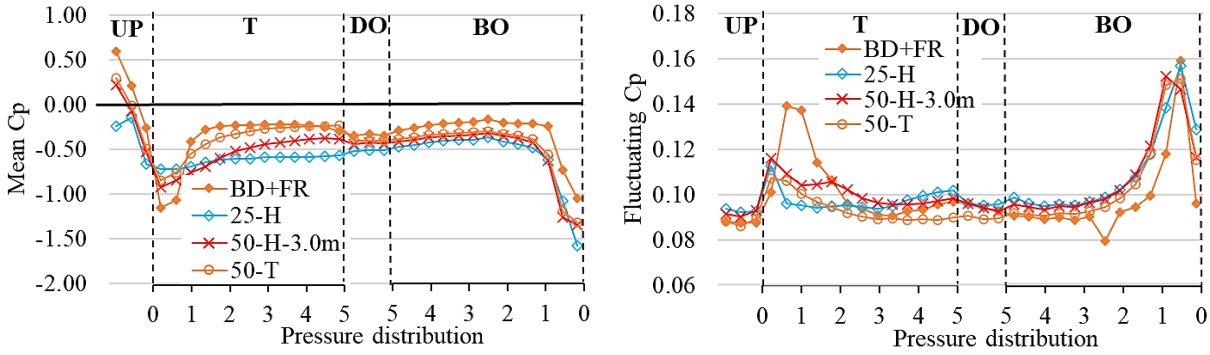

(a) Mean pressure coefficient (b) Fluctuating pressure coefficient

Figure 5.21 Mean and fluctuating pressure coefficient distribution of the bluff girder with fairing (BD+FR) and wind barriers

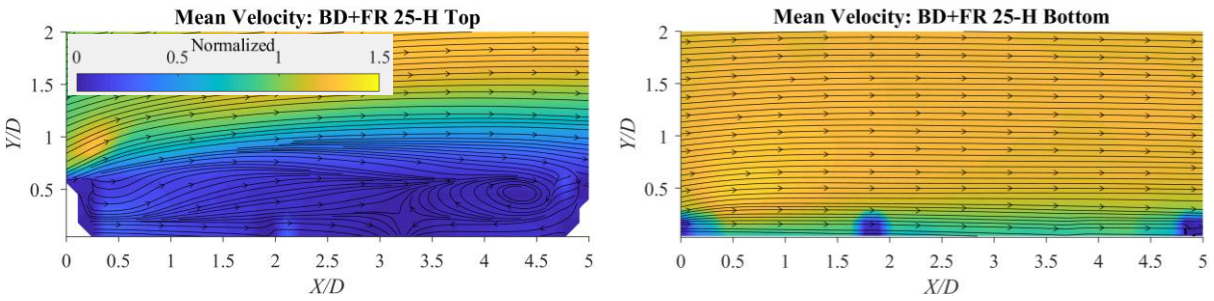

(a) Top side (b) Bottom side

Figure 5.22 Mean wind flow field of the bluff girder with fairing (BD+FR) with 25-H

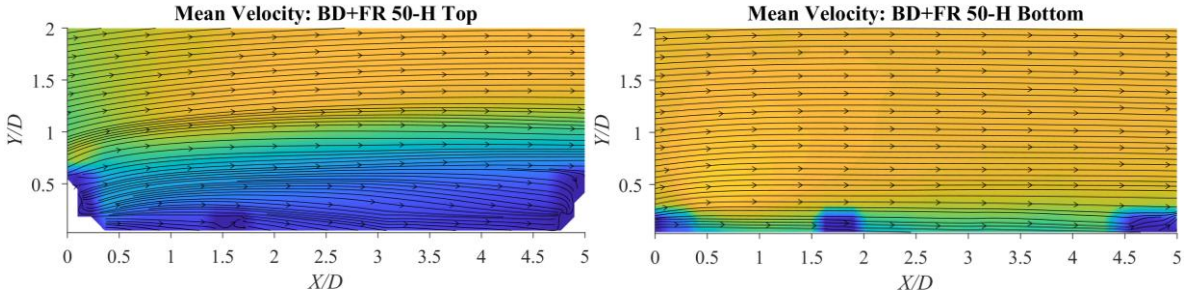

(a) Top side (b) Bottom side

Figure 5.23 Mean wind flow field of the bluff girder with fairing (BD+FR) with 50-H-3.0m

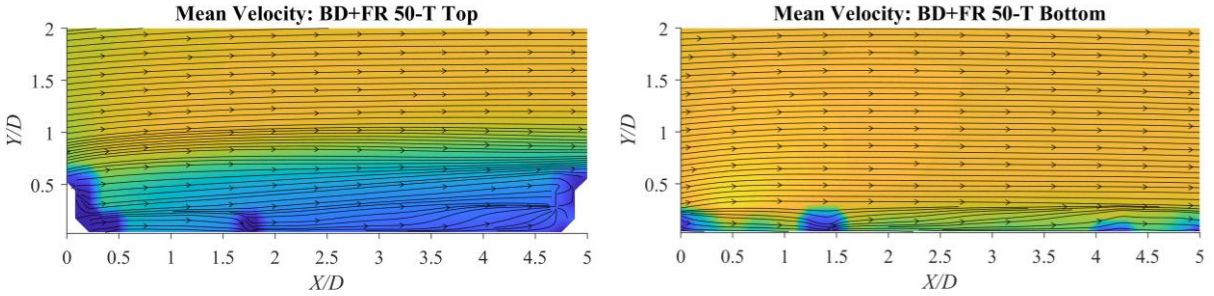

(a) Top side (b) Bottom side

Figure 5.24 Mean wind flow field of the bluff girder with fairing (BD+FR) with 50-T

5.7 Concluding remarks

This section elucidates the mechanisms by which wind barriers influence the vertical vortex-induced vibration (VIV) of a rectangular bluff box girder with a side ratio of 5.00 and its attachment with a fairing for some cases to serve as a stabilizing countermeasure. Parameters such as porosity ratios, heights, shapes of bar members, and countermeasures are considered. The vertical vibrational response of the girders was examined using a one-degree-of-freedom

free vibration test. The mechanisms of VIV were elucidated through a flow visualization using Particle Image Velocimetry (PIV) analysis and a pressure distribution measurement of the stationary sectional model. The main findings are as follows:

1) The bluff girder with a side ratio of 5.00 in this section exhibited a similar vertical VIV trend to the bluff girder with a side ratio of 4.98 in Chapter 4. This confirms its suitability as a fundamental bluff body for clarifying the mechanism of vertical VIV of the target bridge for this study.
2) The new proposed triangular bar member wind barrier (50-T) effectively reduced the vertical VIV amplitude in the girder for both with and without fairing cases.
3) In the case of the girder without wind barriers and fairing considered as a bare deck, the main recirculation zone resulted in a small mean pressure. Its reattachment at a relative distance of about $X/Y = 3.5$ results in mean pressure recovery with high-pressure fluctuation at this zone which might potentially contribute to vertical VIV. In the presence of the fairing, a relatively weaker separated shear layer was observed at the leading edge and reattached near this zone resulting in a large negative mean pressure and high-pressure fluctuation which might be responsible for vertical VIV.
4) In the presence of the rectangular wind barriers for the girder without fairing, the flow separation on the top side shifted from the edge of the girder to the top of the wind barriers, transforming the flow from reattached type to detached type. This transformation recovered the mean pressure at the leading edge and reduced the pressure fluctuation on the trailing-edge zone of the girder. Additionally, wind barriers affected the mean pressure on the upstream side of the girder indicating the shifting of the stagnation point which might be attributed to the increased effective depth of the girder. This change results in the promotion of the shear layer separation and the intensification of the recirculation zone on the bottom side of the girder resulting in significant mean pressure reduction and high-pressure fluctuation that possibly contributes to destabilized vertical VIV.
5) The proposed triangular bar wind barrier (50-T) whose bar members are more aerodynamical compared to the rectangular one accelerated flow on the top side of the girder resulting in a homogenous flow that eliminated the recirculation zone, leading to the most rapid mean pressure recovery and the smallest pressure fluctuation compared to other cases. Additionally, this wind barrier had less impact on the promotion of the shear layer separation on the bottom side which resulted in reduced mean and fluctuating pressure gap between the bare deck and other wind barriers. These aerodynamic improvements contribute potentially to VIV stabilization.
6) In the case of the fairing attachment with wind barriers, wind barriers altered the flow on the top side from a leading-edge vortex type to a detached type resulting in increased mean pressure and decreased pressure fluctuation at the leading edge due to the elimination of the flow reattachment. Importantly, flow separation controlled by fairing on the upstream side of the girder resulted in flow acceleration on the top side for the 50% porosity wind barriers. Consequently, the flow on the top side is homogeneous leading to lower pressure fluctuation compared to the bare deck while the mean pressure reduction and the pressure fluctuation amplification on the bottom side were minimized compared to the 25% porosity wind barrier. This flow control on the upstream side by fairing which reduced the gap of mean pressure reduction and pressure fluctuation amplification on the bottom side as compared to without fairing case was attributed to better performance in VIV stabilization.

7) The spanwise correlation coefficient of sectional fluctuating lift force which suggested the flow structure along the spanwise direction of the girder showed that it was increased by rectangular bar member wind barriers indicating the well-formed and more synchronized flow structure along the span possibly contributing to the amplified VIV. Meanwhile, the triangular wind barrier and the bare deck showed the smallest correlation compared to other cases implying a more scattered and less synchronized flow structure which corresponds to stabilized VIV.

In conclusion, wind barriers not only disrupted the flow on the top side of the girder where they were installed but also significantly altered the flow on the bottom side and the flow structure along the spanwise of the girder. This resulted in changes to the mean and fluctuating pressure distribution around the girder, contributing to the stabilization or destabilization of vertical VIV.

CHAPTER 6
Conclusions

6.1 Conclusions

This research experimentally investigated the impact of various wind barriers on the aerodynamic performance of bluff box girders, focusing on two primary objectives. The first objective was to evaluate the effect of wind barriers with different parameters encompassing hole schemes, porosity ratios, heights, and countermeasures for stabilizing vertical Vortex-Induced Vibrations (VIV) of two bluff box girders. These girders, designed with side ratios of 3.44 (thick girder) and 4.98 (thin girder), are representative of the future extendable section of the Trans-Tokyo Bridge. Wind tunnel tests were conducted including an aerodynamic force measurement, a two-degree-of-freedom free vibration test, and a wind velocity measurement, aiming to ensure the stability of the bridge and the safety of vehicles traveling on it. The results indicated that the aerodynamic performance and wind flow field of the bridge together with the stabilization and destabilization of vertical VIV are significantly influenced by the configuration of both the bridge girder and the wind barriers.

The second objective was to elucidate the mechanisms of the vertical VIV of a rectangular bluff box girder with a side ratio of 5.00 affected by wind barriers, as well as the girder attachment with fairings on both sides for vertical VIV stabilization. To achieve this objective, a series of wind tunnel tests, including a one-degree-of-freedom free vibration test, a pressure measurement, and a flow visualization using Particle Image Velocimetry (PIV) analysis, were conducted.

Based on the two objectives, the conclusions are divided into two sections. The first section consists of the first objective as the following:

1) A larger side ratio girder (thin girder) exhibited relatively larger mean and maximum wind speeds compared to a smaller side ratio girder (thick girder), suggesting that implementing wind barriers selectively in susceptible areas, such as the center span of bridges with varying girder depths, is both cost- and time-effective with minimal impact on the overall aerodynamic performance of the bridges.
2) Most wind barriers significantly reduced mean and maximum wind speeds and turbulence intensity over driving areas, especially reducing strong wind speeds in windward lanes by 2 to 4 times, thereby enhancing vehicle driving safety. Although countermeasures marginally increased wind speeds near the surface of the girders, they notably benefited large vehicles prone to strong crosswinds.
3) Since wind barriers reduced the wind speed above the girder. Consequently, for the thick girder as compared to the bare deck (no wind barriers installed), they significantly increased the drag coefficient due to the increased windward area and decreased the lift coefficient while the moment coefficient was largely unaffected. Under quasi-steady conditions, no galloping was observed with wind barriers.

4) Wind barriers showed minimal impact on the structural characteristic parameters of both girders, indicating that changes in aerodynamic responses in both vertical and torsional modes were primarily due to alterations in wind flow caused by the wind barriers.
5) Most wind barriers significantly improved the stabilization of torsional VIV compared to the bare deck, although some of them increased the vertical VIV amplitude and reduced the critical wind velocity for torsional flutter.
6) The orientation of wind barrier hole schemes of horizontal and vertical direction had a negligible effect on the aerodynamic response of the thick girder. Installing wind barriers above the handrail instead of beside it emerged as a practical and cost-effective strategy, particularly for bridge girders with limited space.
7) In the thick girder, proposed countermeasures showed better performance in reducing vertical VIV amplitude compared to standard wind barriers, particularly with stabilization effects observed in wind barriers combined with flaps. However, these countermeasures yielded consistent vertical VIV results in the thin girder.
8) The stabilization and destabilization of vertical VIV possibly correlated to the turbulence intensity near the surface of the girder in which the increased turbulence intensity contributed to the stabilization.
9) The porosity ratio is a crucial parameter affecting both the aerodynamic response of the bridge and the wind speed reduction for vehicle driving safety. In the thick girder, increasing the porosity ratio from 25% to 50% reduced vertical VIV amplitude from approximately 800 mm to 300 mm, and in the thin girder from 600 mm to 200 mm, alighting with the vertical VIV amplitude of the bare deck. Increasing porosity also raised the critical wind velocity for torsional flutter but remained lower than the bare decks. Reduced porosity ratio significantly decreased wind speeds above the bridge.

Overall, the aerodynamic performance of the bridge significantly depended on the configuration of its girder and wind barriers. Although wind barriers generally reduced wind speeds for driving safety enhancement, they often increased the VIV amplitude in vertical mode while stabilizing such vibration in torsional vibration mode. Additionally, Wind barriers decreased the critical wind velocity for torsional flutter compared to the base deck cases. The balance between the aerodynamic performance of the bridges and the shielding effectiveness of wind barriers must be carefully considered.

The specific design of different configurations of wind barriers for various bridges can result in both stabilization and destabilization of aerodynamic performance. Hence, how these configurations of wind barriers relate to the mechanism of vertical VIV of a rectangular bluff box girder with a side ratio of 5.00, including its attachment with fairing and new proposed triangular bar member wind barrier, are concluded as follows:

1) The introduction of rectangular wind barriers on the girder without fairing caused a shift in flow separation on the top side of the girder from the leading edge to the top of the barriers, transforming the flow type from reattached to detached. This alteration modified the recirculation zone under the separated shear layer, resulting in mean pressure recovery at the leading-edge zone and reduced pressure fluctuation at the trailing-edge zone. However, the wind barriers significantly altered the mean pressure on the upstream side of the girder resulting in the promotion of the shear layer separation and the amplification of the recirculation zone on the bottom side of the girder, leading to strong pressure reduction and

high fluctuation compared to the bare deck, which in turn possibly compensated for amplified vertical VIV.

2) For no fairing attachment, the 25% porosity wind barrier (25-H) exhibited a more pronounced effect of promoting the shear layer separation on both the top and bottom sides of the girder with and without fairing attachment, significantly leading to mean pressure reduction on the bottom side and high-pressure fluctuation on both sides of the girder which might contribute to the largest vibrational amplitude of vertical VIV. This strong effect might be attributed to the low porosity of the barrier, which behaved similarly to a solid wall, instead of a porous one. This possibly affected the flow development on the upstream side of the girder and then affected the flow on both sides. In contrast, a higher porosity ratio (larger open area) allowed more airflow through it which accelerated the flow leading to less effect on the promotions of the separated shear layer at both sides of the girder as compared to 25-H led to a mitigated vertical VIV.
3) In the case of the countermeasures (50-H-DS and 50-H+F) that reduced the VIV amplitude in no fairing case to smaller than the normal wind barrier (50-H-3.0m) but still higher than the bare deck, they increased the mean pressure and decreased the pressure fluctuation on the top side of the girder compared to the normal barrier and the bare deck. On the other hand, although they reduced the pressure fluctuation at the leading-edge zone on the bottom side of the girder to lower than the normal wind barrier, it is still significantly higher than the bare deck. These pressure distributions well agree with their vibrational response.
4) For the triangular bar member wind barrier, installed on the girder without fairing, that successfully stabilized the vertical VIV. Due to its streamlined bar member shape, this wind barrier accelerated wind flow on the top side of the girder resulting in a homogenous flow that eliminated flow recirculation leading to the quickest mean pressure recovery and the smallest pressure fluctuation on this side compared to all other cases. Interestingly, this barrier had a minimal impact on promoting the shear layer separation and intensifying the recirculation zone at the bottom side, thereby reducing the mean and fluctuating pressure gaps between wind barriers and the bare deck on this bottom side.
5) An increase in the spanwise correlation coefficient of sectional fluctuating lift force indicated a well-formed and more synchronized flow structure along the span of the girder, which potentially corresponded to amplified VIV amplitude. Meanwhile, a decrease in the correlation implied a more scattered and less synchronized flow structure which led to reduced VIV amplitude.
6) In the case of wind barriers installed on the girder with faring, they transformed the flow on the top side of the girder to a detached type resulting in a smaller pressure reduction and pressure fluctuation at the leading-edge zone compared to the bare deck, but they significantly increased the mean pressure reduction and pressures fluctuation at the trailing-edge zone on this side. However, when compared to the girder without fairing, the effect of wind barriers on fairing attachment for promoting shear layer separation and intensifying flow recirculation on the bottom side was relatively limited leading to smaller gaps of mean pressure reduction and fluctuating pressure amplification, contributing to better performance in stabilizing vertical VIV.

The findings of the second objective imply that wind barriers not only significantly influence the flow field on both the top and bottom sides but also on the flow structure along the spanwise direction of the girder, leading to changes in both mean and fluctuating pressures on both sides as well as the spanwise correlation coefficient which potentially contribute to the

stabilizing and destabilizing of vertical VIV. Effective design of wind barriers for bluff girders with reattachment flow type, with a side ratio of 5.00 in the case of this study, should focus on diminishing recirculation flow on the top side and limiting the effect of the wind barriers on the promotion of the shear layer separation and the intensification of flow recirculation on the bottom side of the girder together with disturbing the coherent structure of the flow along the girder, which are critical for stabilizing the amplitude of vertical VIV.

In conclusion, the wind barriers effectively reduced wind speed in the driving zone, enhancing driving safety. However, different configurations of bridge girders and wind barriers significantly affected the stabilization or destabilization of the aerodynamic performance of bridges. This study first detailed the effects of various wind barrier parameters on the aerodynamic performance of a bluff box girder with two side ratios providing useful information for wind barrier parameter design for bluff girders. It then provided insights into the mechanism of vertical VIV of a bluff girder related to wind barriers, serving as a guideline for designing wind barriers for this type of girder with a successful countermeasure for stabilizing vertical VIV.

6.2 Future topics

The impact of wind barriers on the aerodynamic performance of a bluff box girder with two side ratios demonstrated their effectiveness in reducing wind speed, though they also led to both stabilization and destabilization of aerodynamic responses. While the mechanisms behind the stabilization and destabilization of vertical Vortex-Induced Vibrations (VIV) were elucidated, some questions remain:

1) Detailed flow visualization around the wind barriers can provide insights into how specific parameters, particularly the shapes of bar members, influence the mechanisms of vertical VIV. However, due to scaling limitations, wind tunnel experiments may face challenges that computational fluid dynamics (CFD) simulations could address more effectively.
2) The pressure measurements and flow visualizations conducted on stationary sectional models highlight the need for tests under vibrating conditions. These tests could offer a deeper understanding of the VIV mechanisms and the dynamic interaction between the flow and bridge girders with wind barriers.
3) Investigating the effects of wind barrier parameters, such as round shapes and elongated rectangular shapes with different aspect ratios of bar members, can significantly enhance the aerodynamic performance of bridges and the driving safety of vehicles. This is especially important for bluff box girders with varying side ratios that result in different flow regimes.

Appendix 1

Flow patterns above the bluff box girders and their alteration by wind barriers

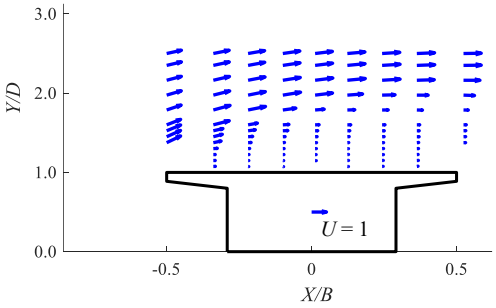

(a) Thick girder (BD of 3.44)

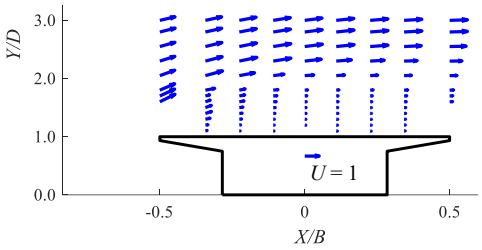

(b) Thin girder (BD of 4.98)

Figure A1.1 Wind velocity vector distribution with 25-H

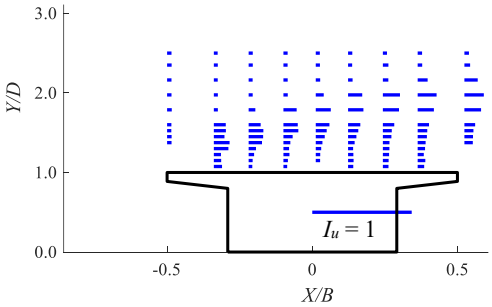

(a) Thick girder (BD of 3.44)

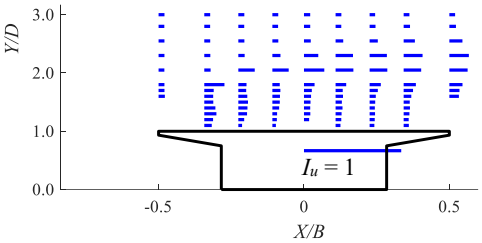

(b) Thin girder (BD of 4.98)

Figure A1.2 Turbulence intensity distribution with 25-H

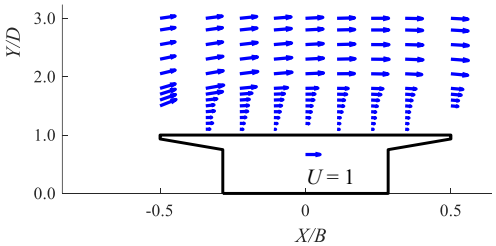

(a) Wind velocity vector

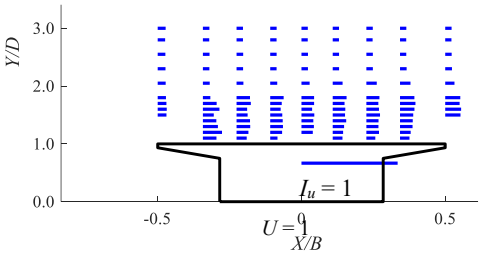

(b) Turbulence intensity

Figure A1.3 Wind flow field distribution of thin girder (BD of 4.98) with 50-H-2.5m

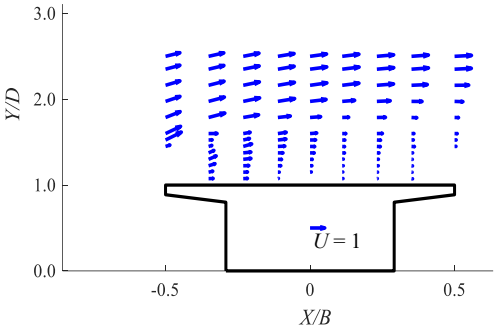

(a) Thick girder (BD of 3.44)

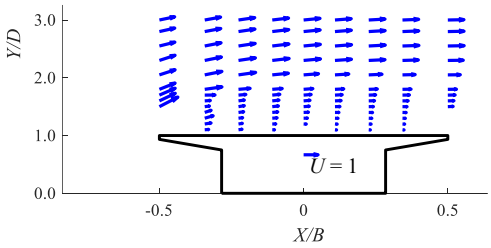

(b) Thin girder (BD of 4.98)

Figure A1.4 Wind velocity vector distribution with 50-H-DS

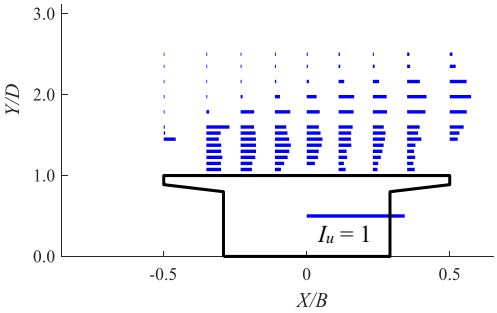

(a) Thick girder (BD of 3.44)

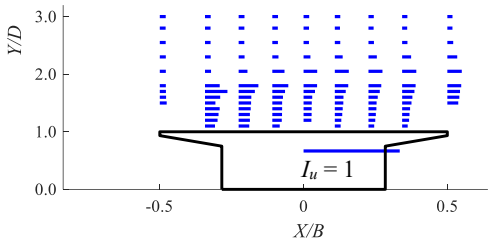

(b) Thin girder (BD of 4.98)

Figure A1.5 Turbulence intensity distribution with 50-H-DS

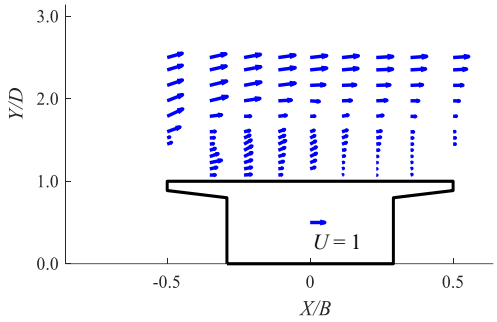

(a) Thick girder (BD of 3.44)

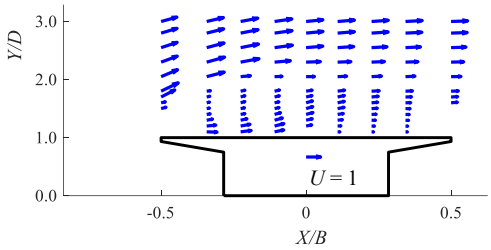

(b) Thin girder (BD of 4.98)

Figure A1.6 Wind velocity vector distribution with 50-H-DS+F

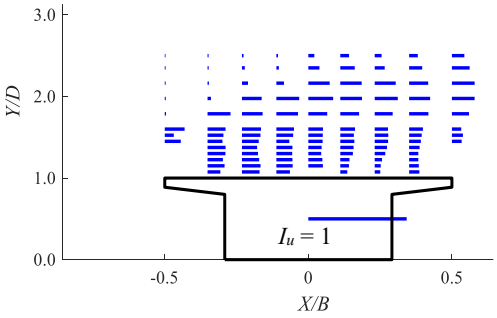

(a) Thick girder (BD of 3.44)

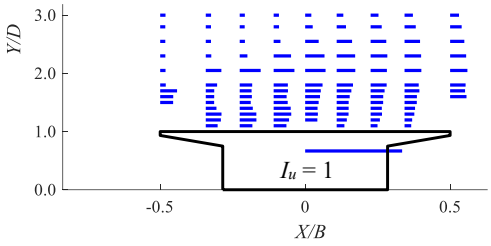

(b) Thin girder (BD of 4.98)

Figure A1.7 Turbulence intensity distribution with 50-H-DS+F

Appendix 2

Vertical aerodynamic response of the girder (*B/D* = 5.00) with fairing attachment and wind barriers

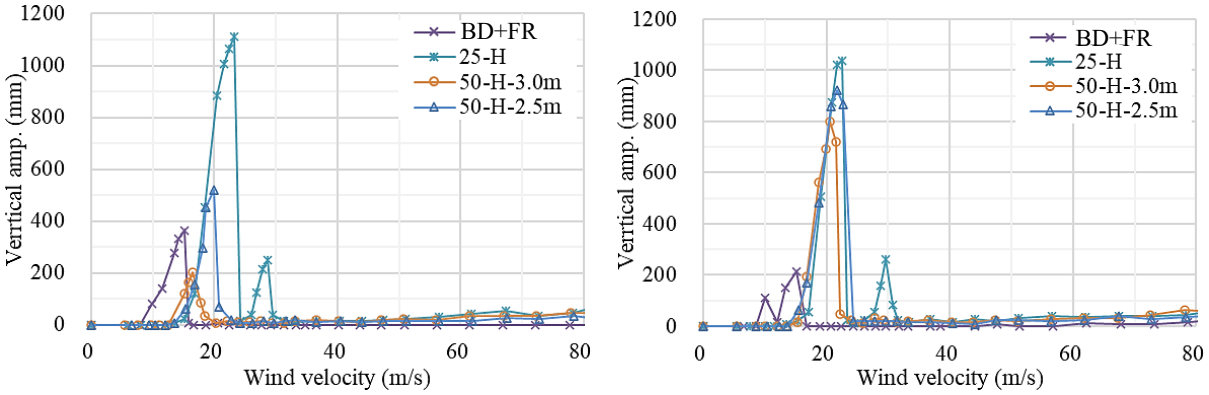

(a) α = 0° (b) α = +3°

Figure A2.1 Vertical aerodynamic response of the girder with fairing attachment (BD+FR) and basic parameter wind barriers

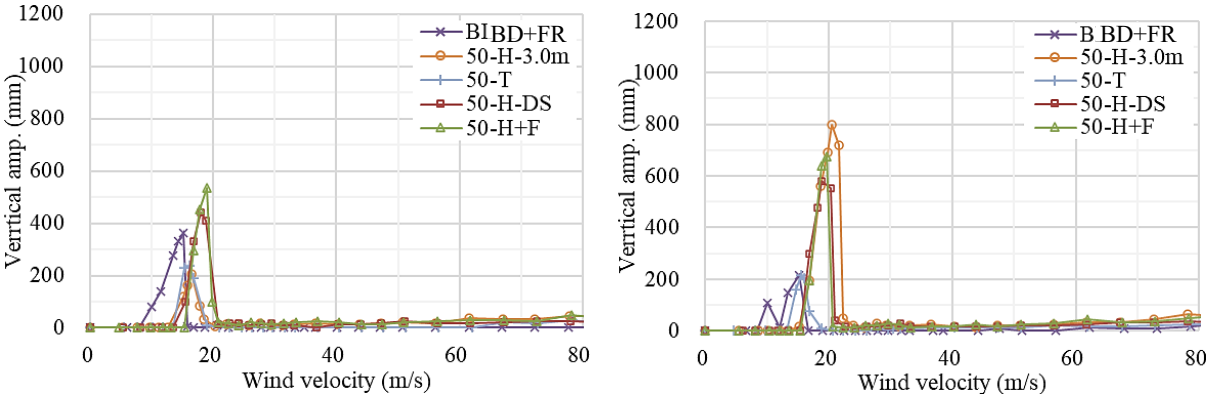

(a) α = 0° (b) α = +3°

Figure A2.2 Vertical aerodynamic response of streamlined girder with countermeasures

Appendix 3

Pressure distribution of the girder (*B/D* = 5.00) with fairing attachment and wind barriers

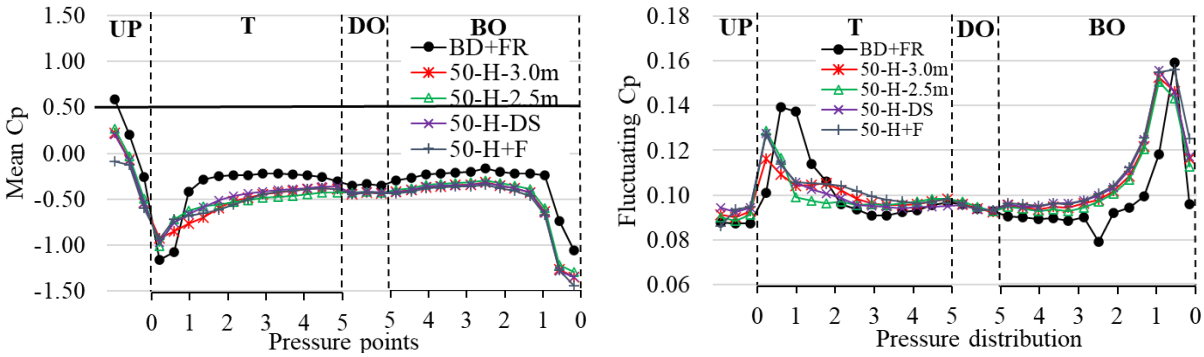

Figure A3.1 Pressure distribution of the girder with fairing attachment and wind barriers

Appendix 4

Wind flow structure around the girder (*B/D* = 5.00) via Proper Orthogonal Decomposition (POD) analysis

A4.1 Bare deck case (BD)

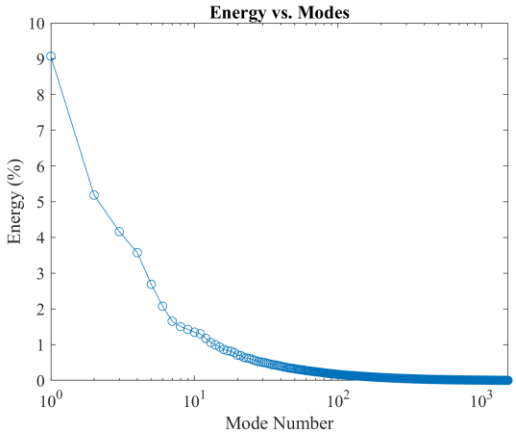

Figure A4.1 Energy of each mode

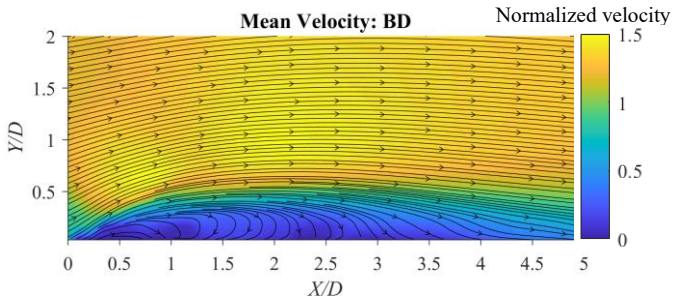

Figure A4.2 Mean wind velocity

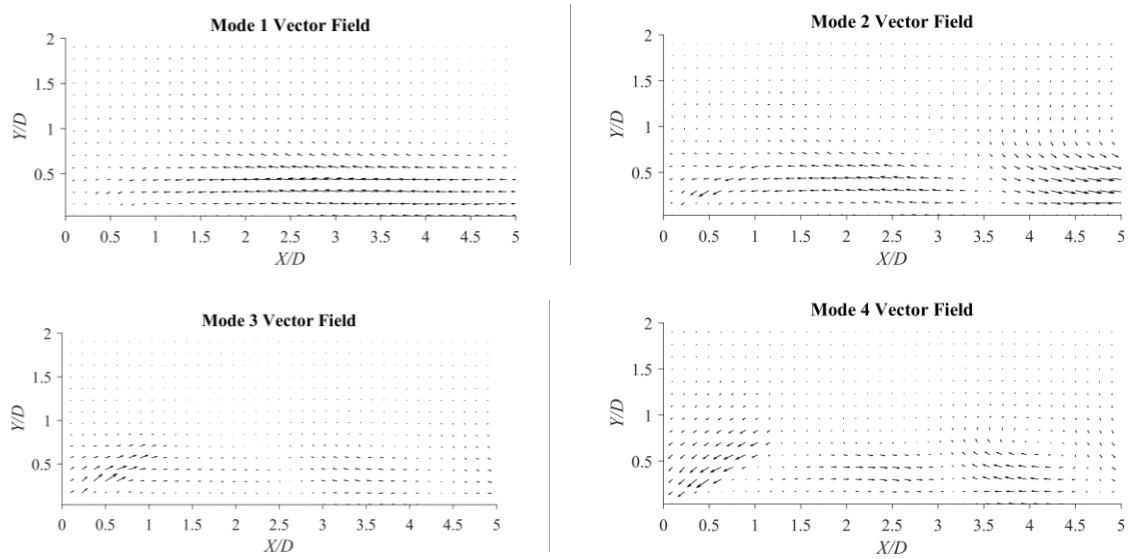

Figure A4.3 Vector field of modes 1 to 4

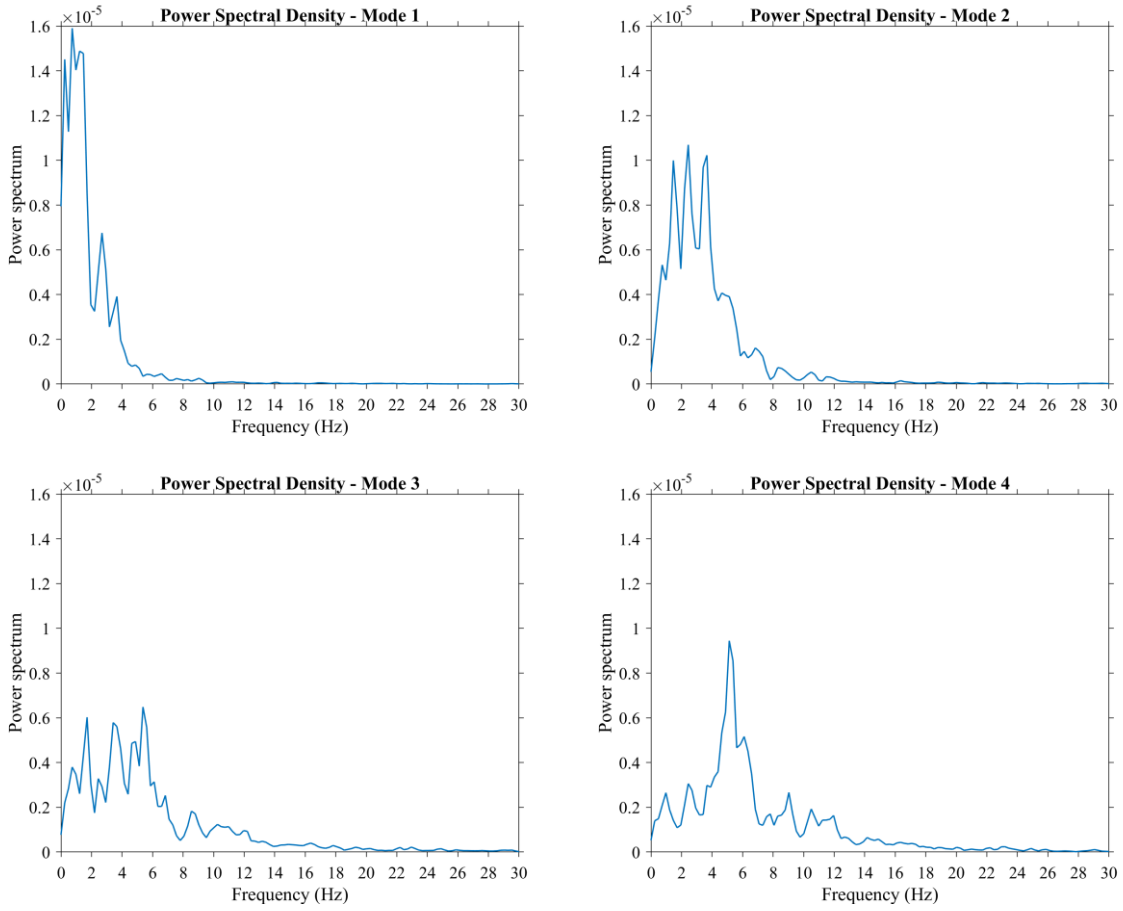

Figure A4.4 PSD of temporal coefficient of modes 1 to 4

A4.2 25-H wind barrier (Top side)

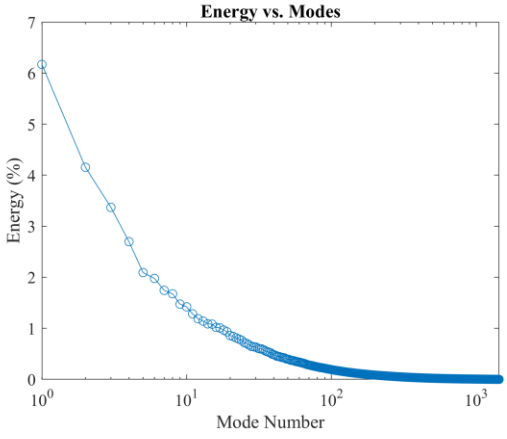

Figure A4.5 Energy of each mode

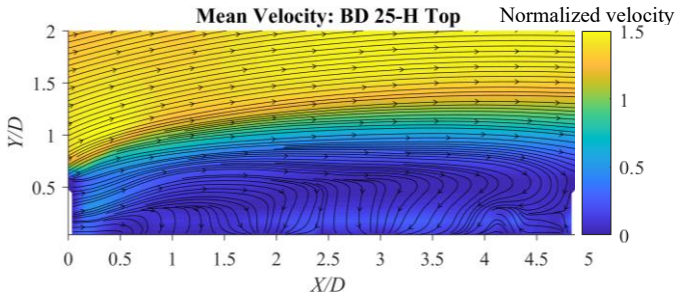

Figure A4.6 Mean wind velocity (Top side)

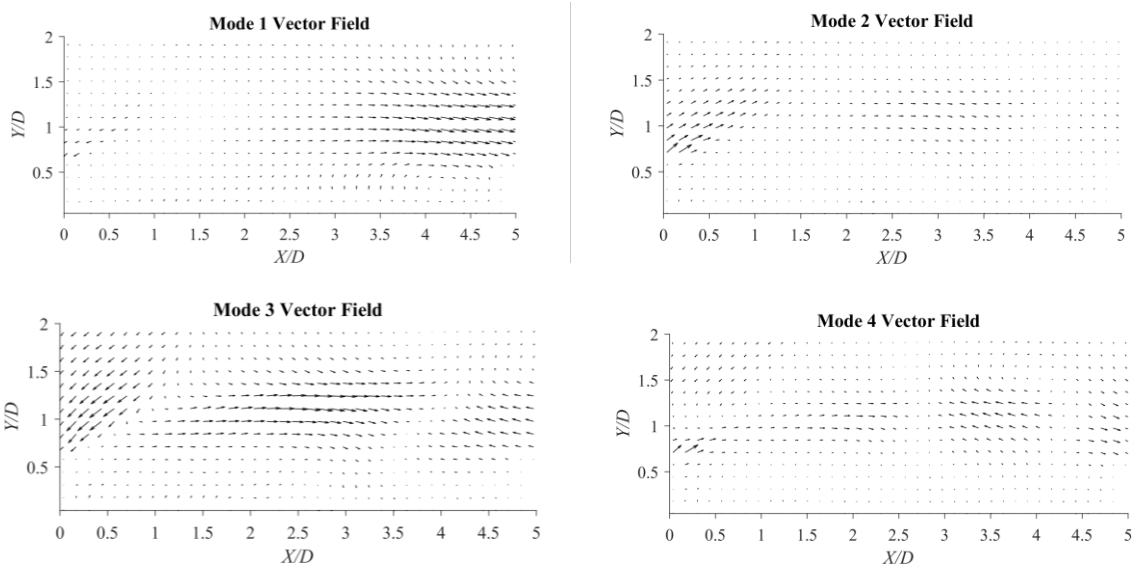

Figure A4.7 Vector field of modes 1 to 4 (Top side)

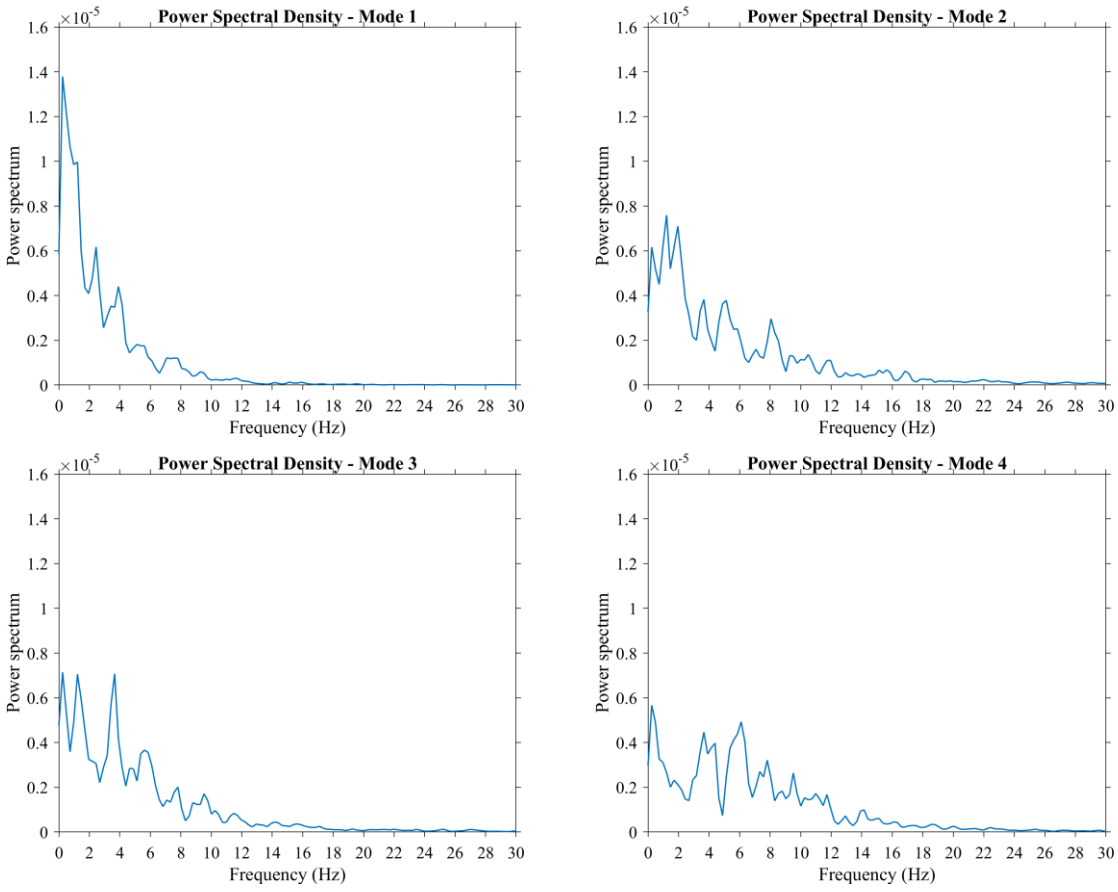

Figure A4.8 PSD of temporal coefficient of modes 1 to 4 (Top side)

A4.3 50-H-3.0m wind barrier (Top side)

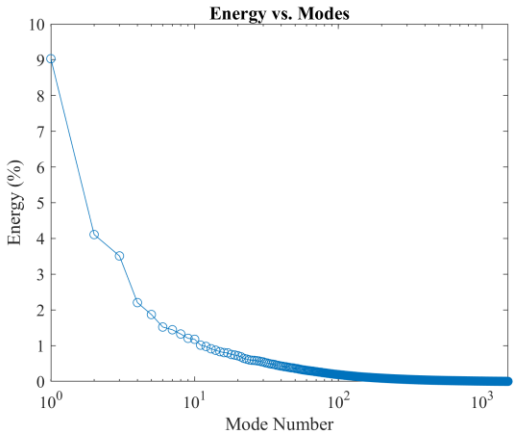

Figure A4.9 Energy of each mode

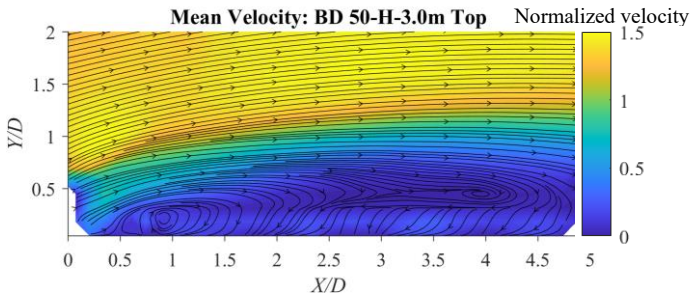

Figure A4.10 Mean wind velocity (Top side)

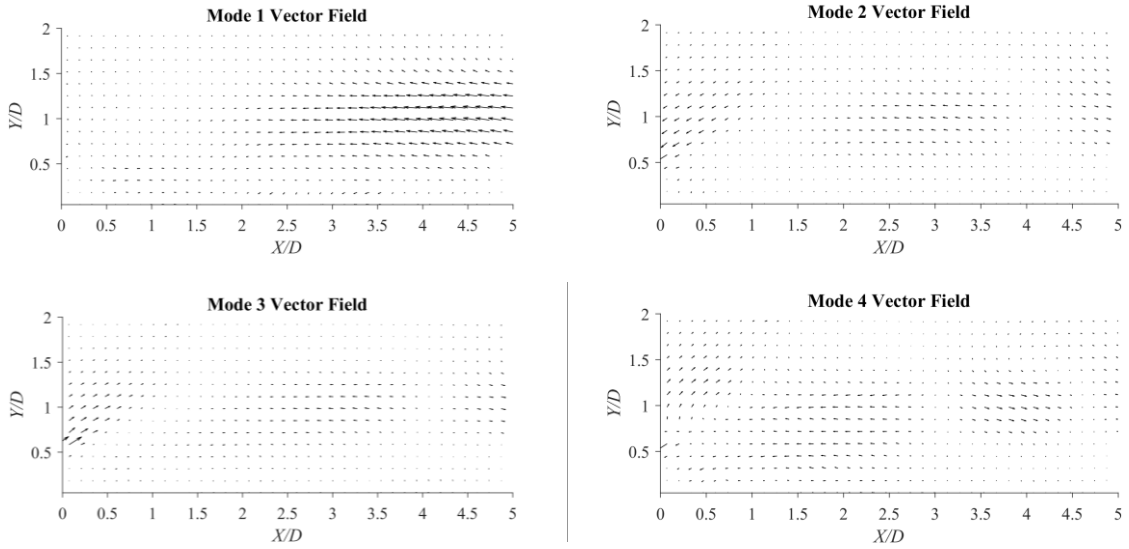

Figure A4.11 Vector field of modes 1 to 4 (Top side)

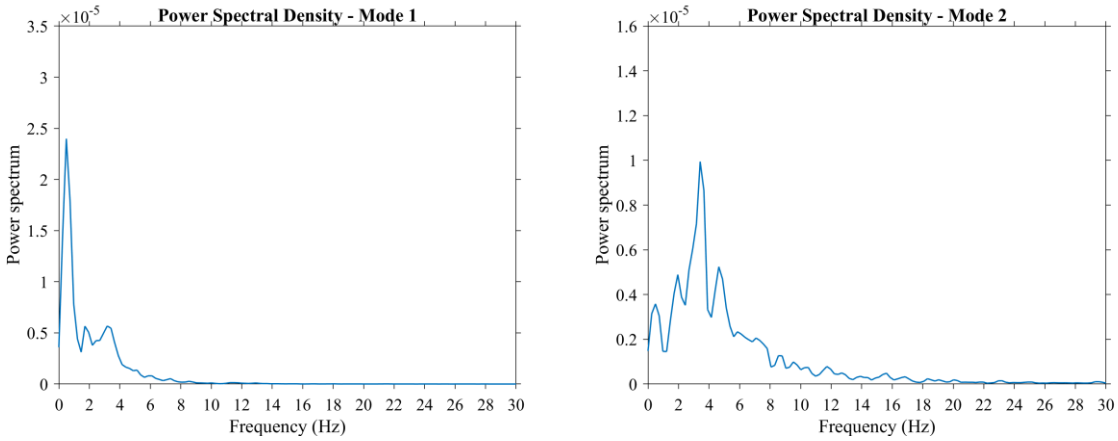

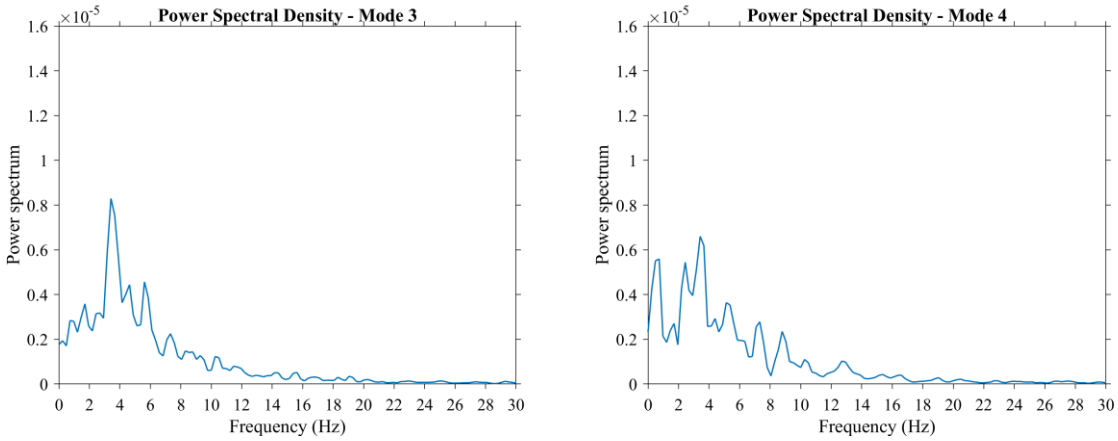

Figure A4.12 PSD of temporal coefficient of modes 1 to 4 (Top side)

A4.4 50-T wind barrier (Top side)

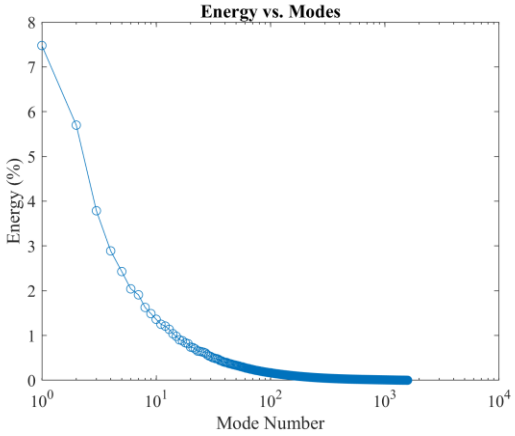

Figure A4.13 Energy of each mode

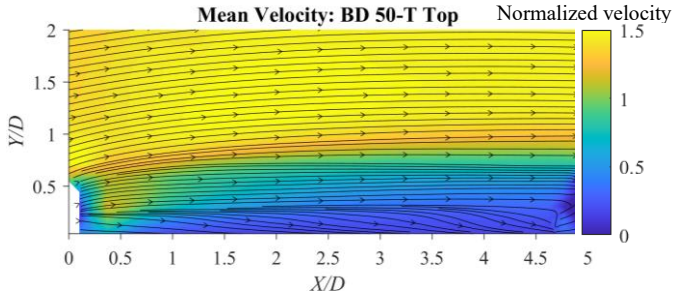

Figure A4.14 Mean wind velocity (Top side)

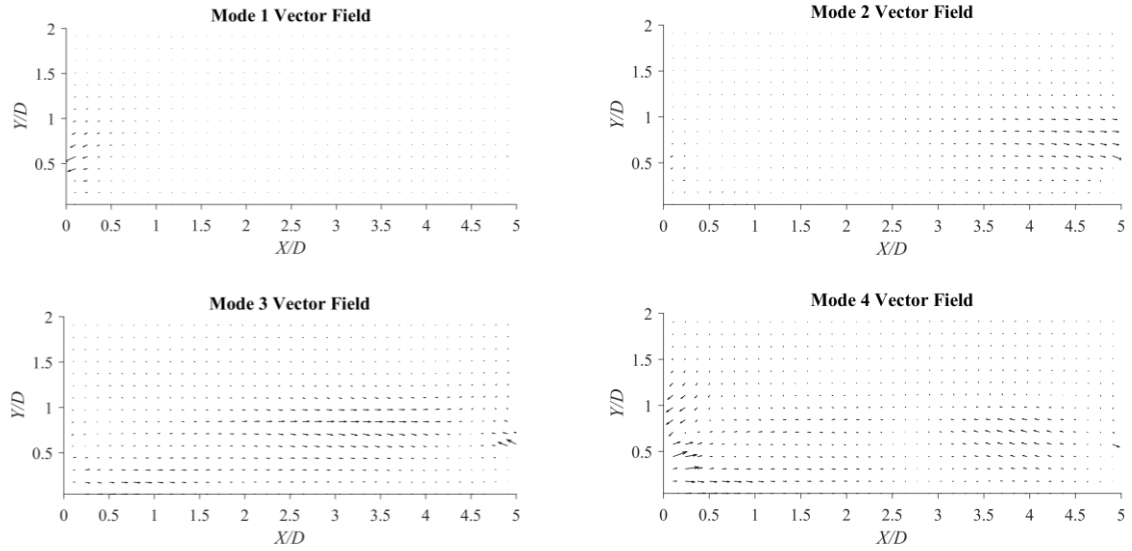

Figure A4.15 Vector field of modes 1 to 4 (Top side)

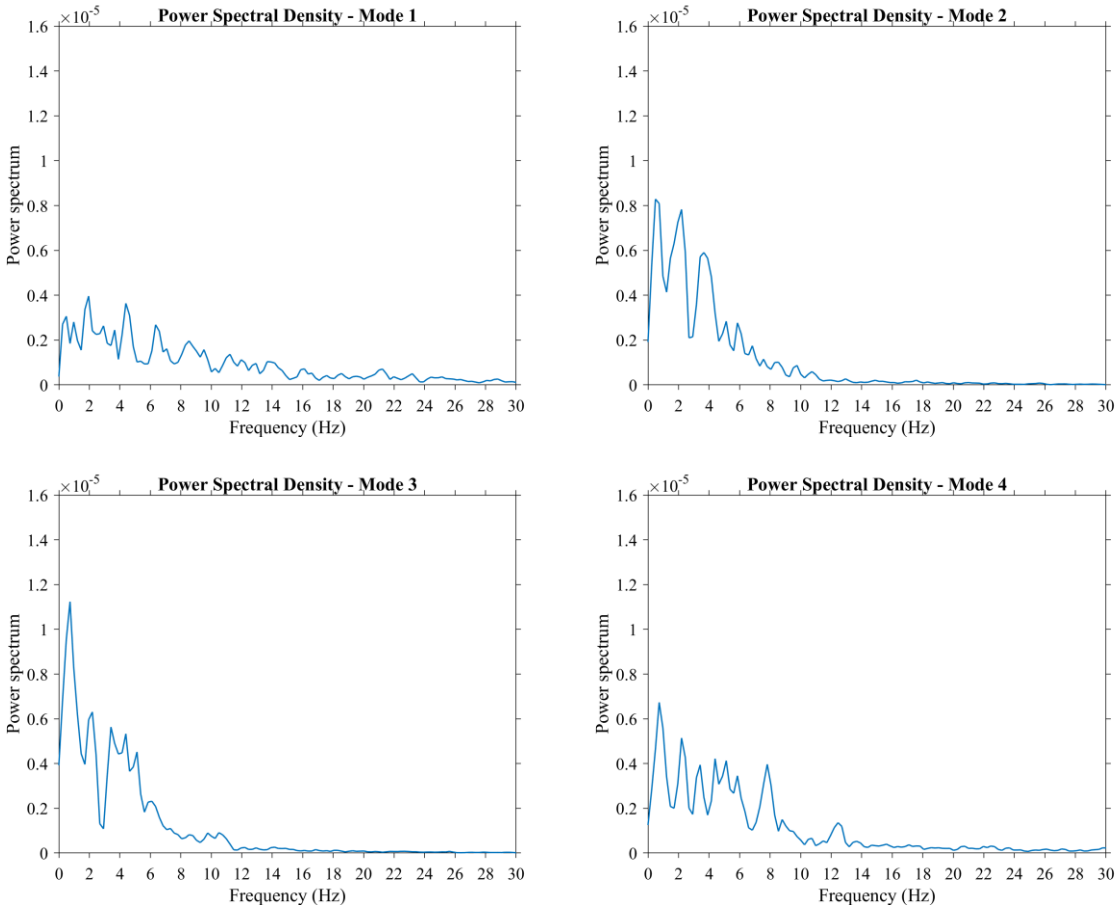

Figure A4.16 PSD of temporal coefficient of modes 1 to 4 (Top side)

A4.5 50-H-2.5m wind barrier (Top side)

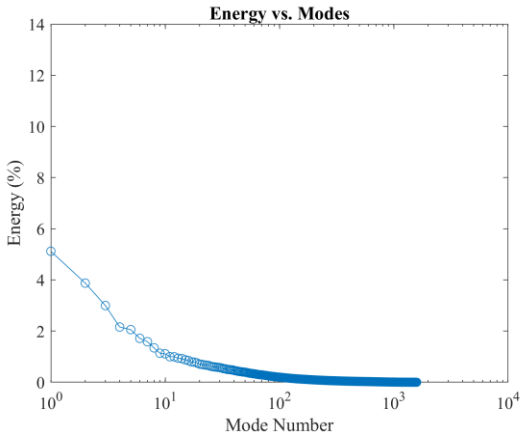

Figure A4.17 Energy of each mode

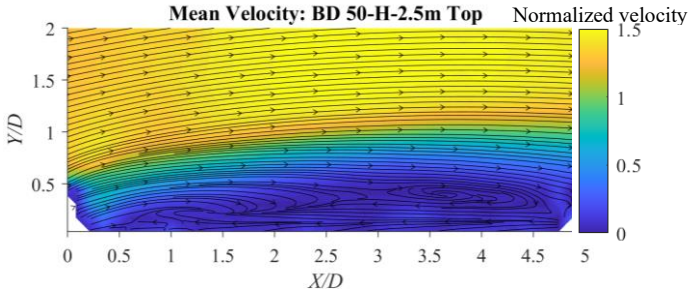

Figure A4.18 Mean wind velocity (Top side)

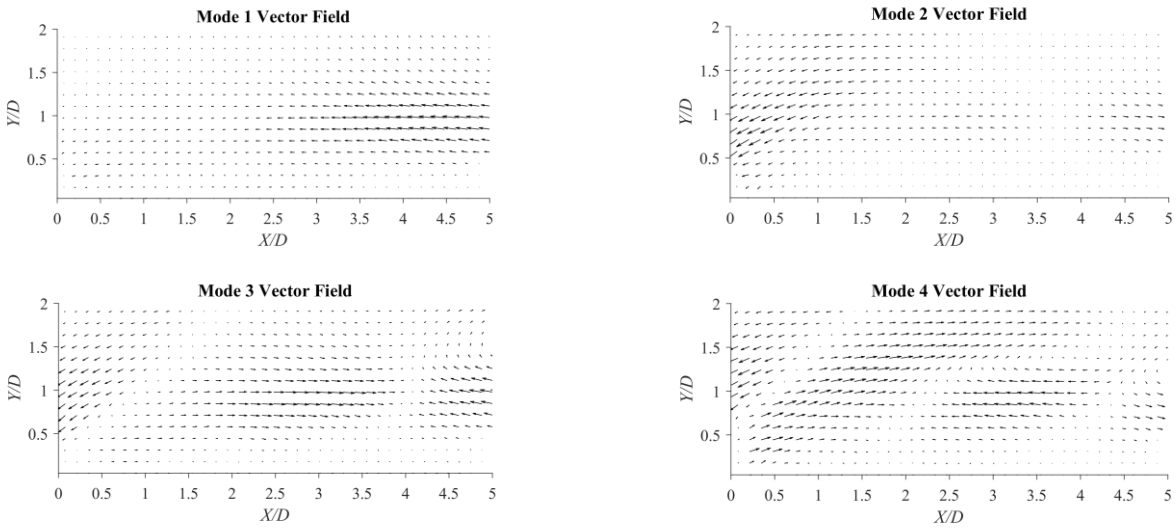

Figure A4.19 Vector field of modes 1 to 4 (Top side)

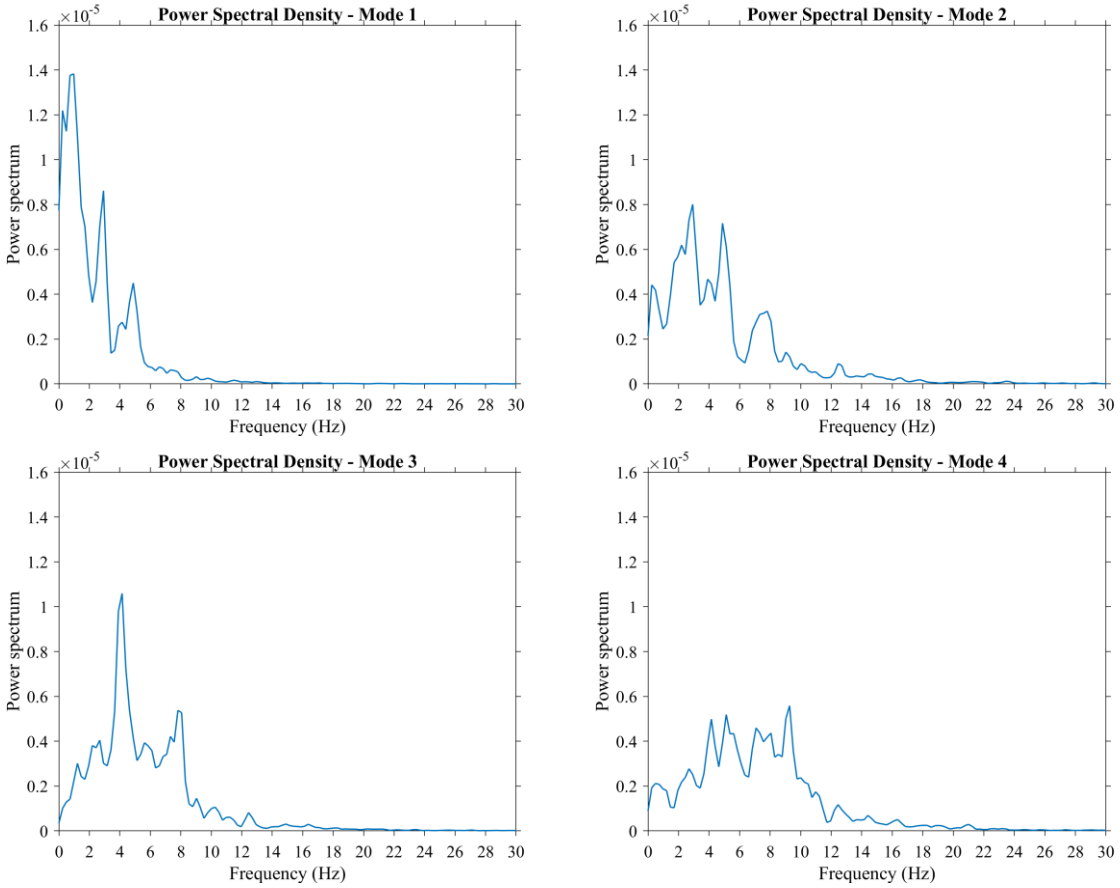

Figure A4.20 PSD of temporal coefficient of modes 1 to 4 (Top side)

A4.6 50-H-DS wind barrier (Top side)

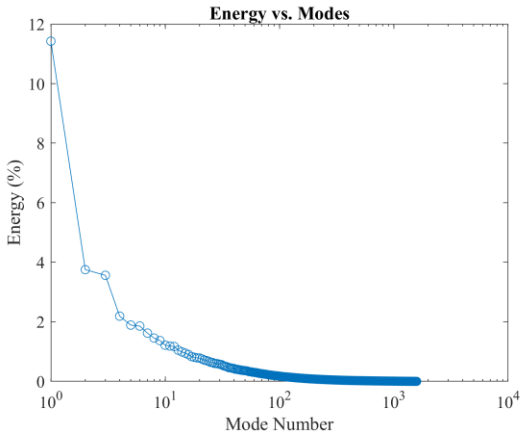

Figure A4.21 Energy of each mode

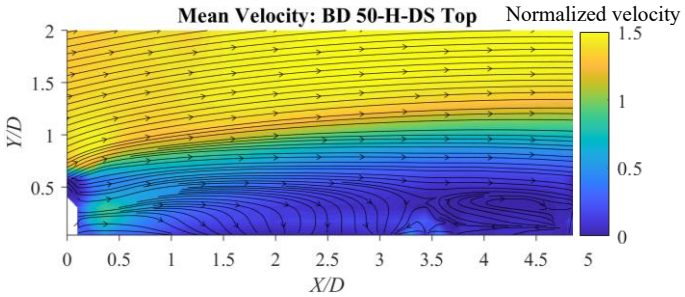

Figure A4.22 Mean wind velocity (Top side)

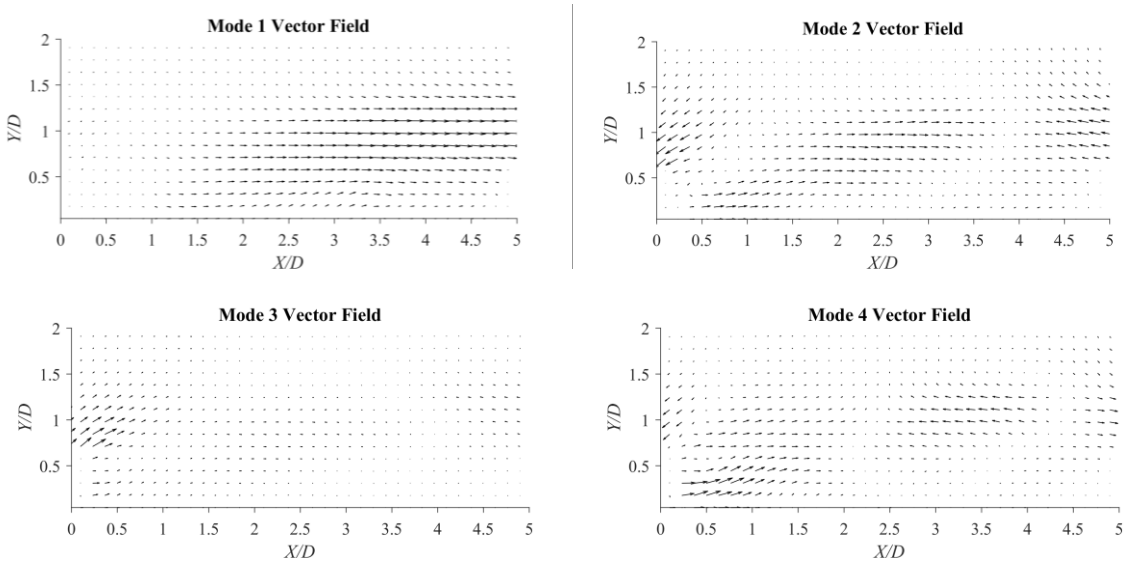

Figure A4.23 Vector field of modes 1 to 4 (Top side)

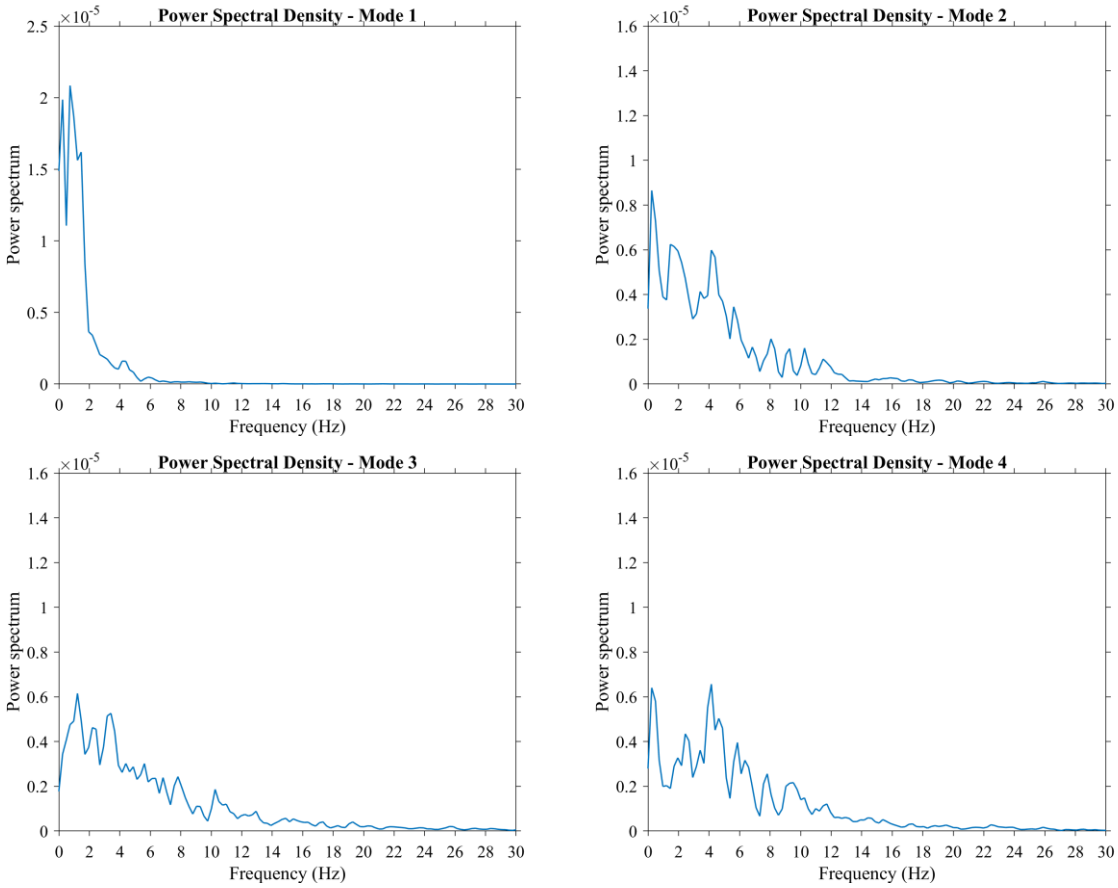

Figure A4.24 PSD of temporal coefficient of modes 1 to 4 (Top side)

A4.7 50-H+F wind barrier (Top side)

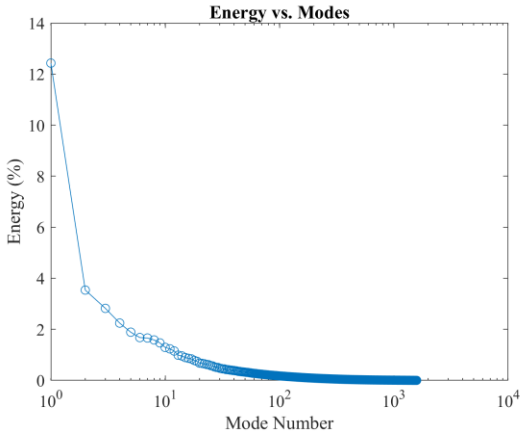

Figure A4.25 Energy of each mode

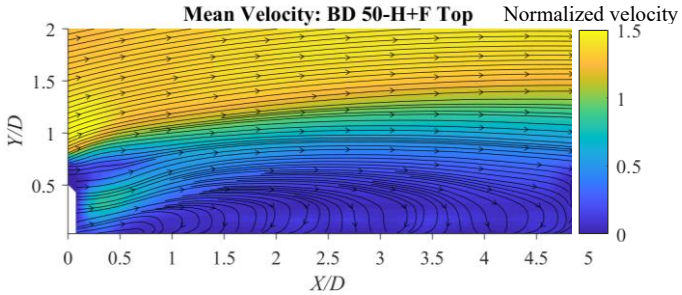

Figure A4.26 Mean wind velocity (Top side)

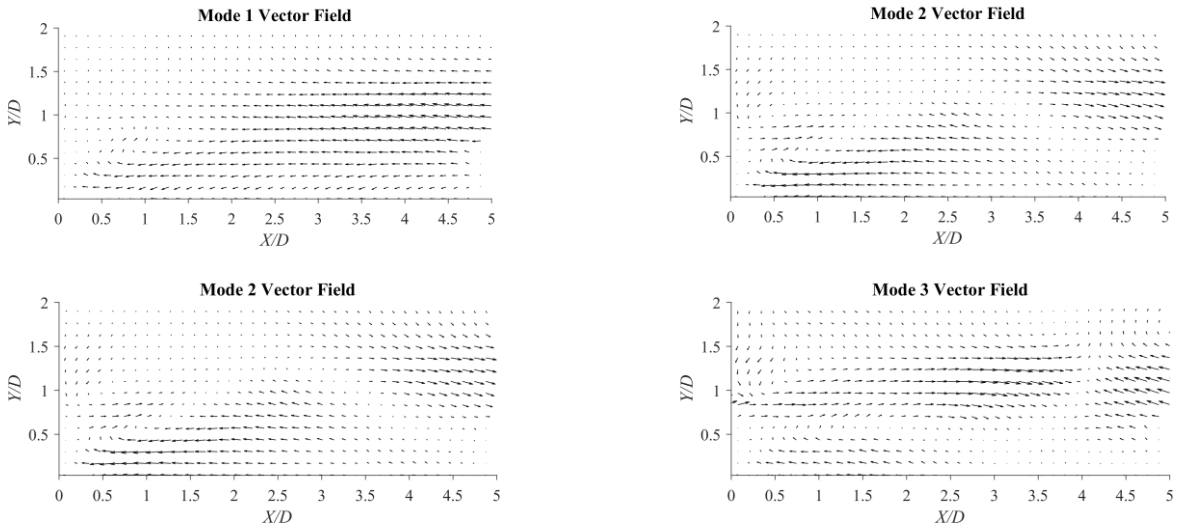

Figure A4.27 Vector field of modes 1 to 4 (Top side)

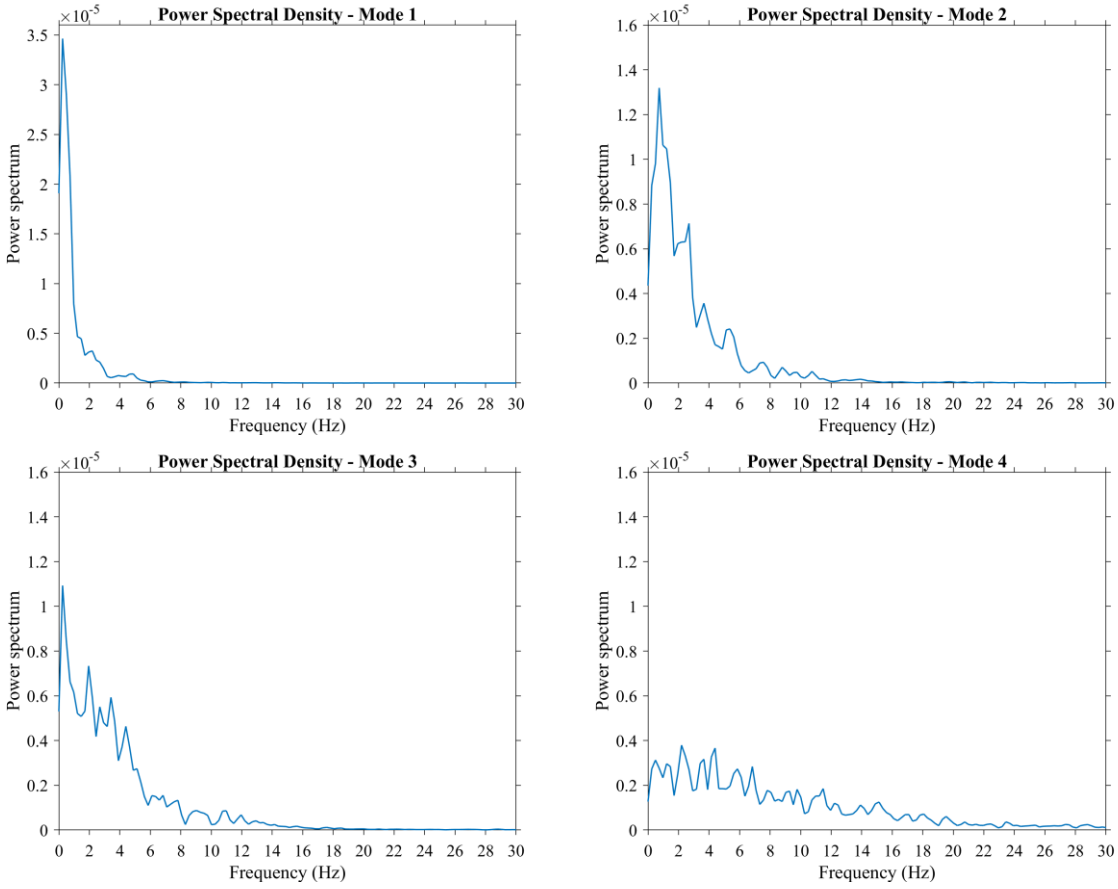

Figure A4.28 PSD of temporal coefficient of modes 1 to 4 (Top side)

A4.8 25-H wind barrier (Bottom side)

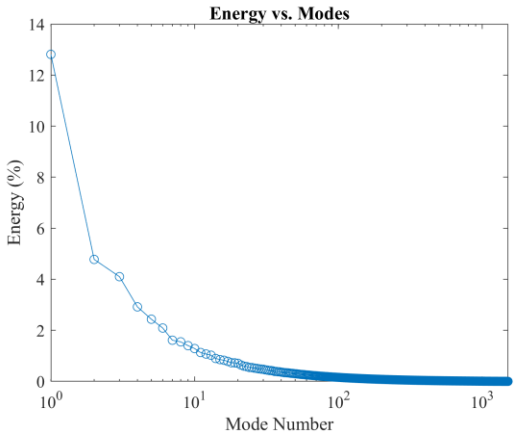

Figure A4.29 Energy of each mode

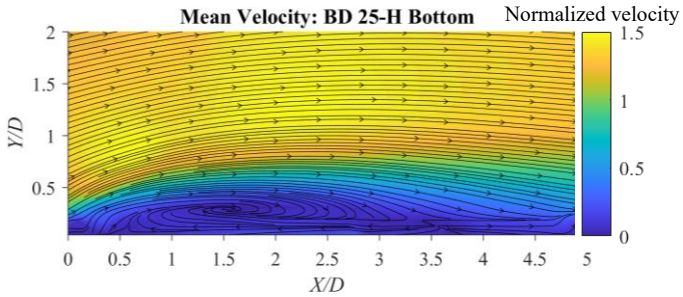

Figure A4.30 Mean wind velocity (Bottom side)

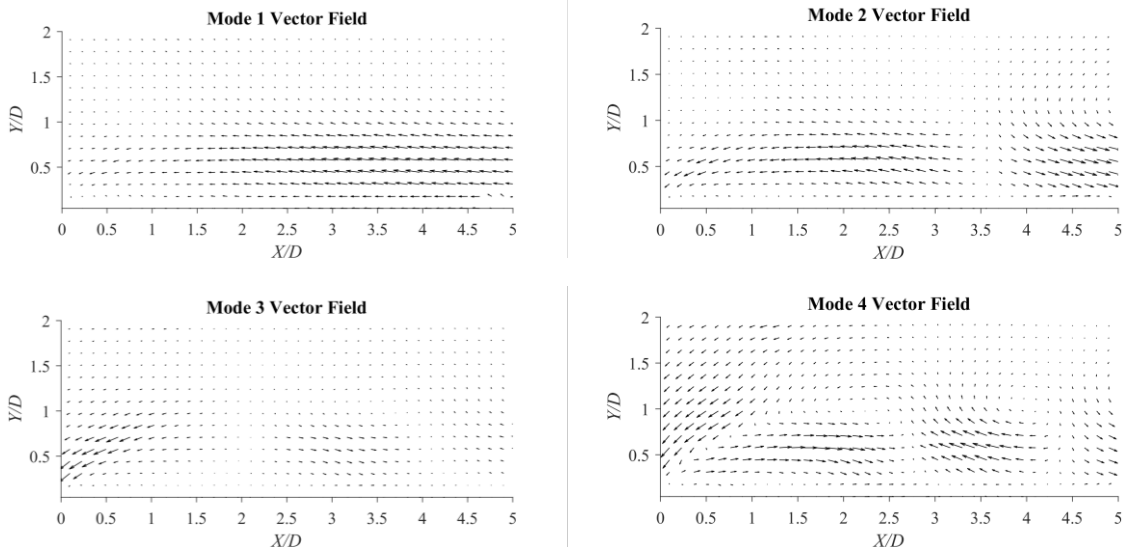

Figure A4.31 Vector field of modes 1 to 4 (Bottom side)

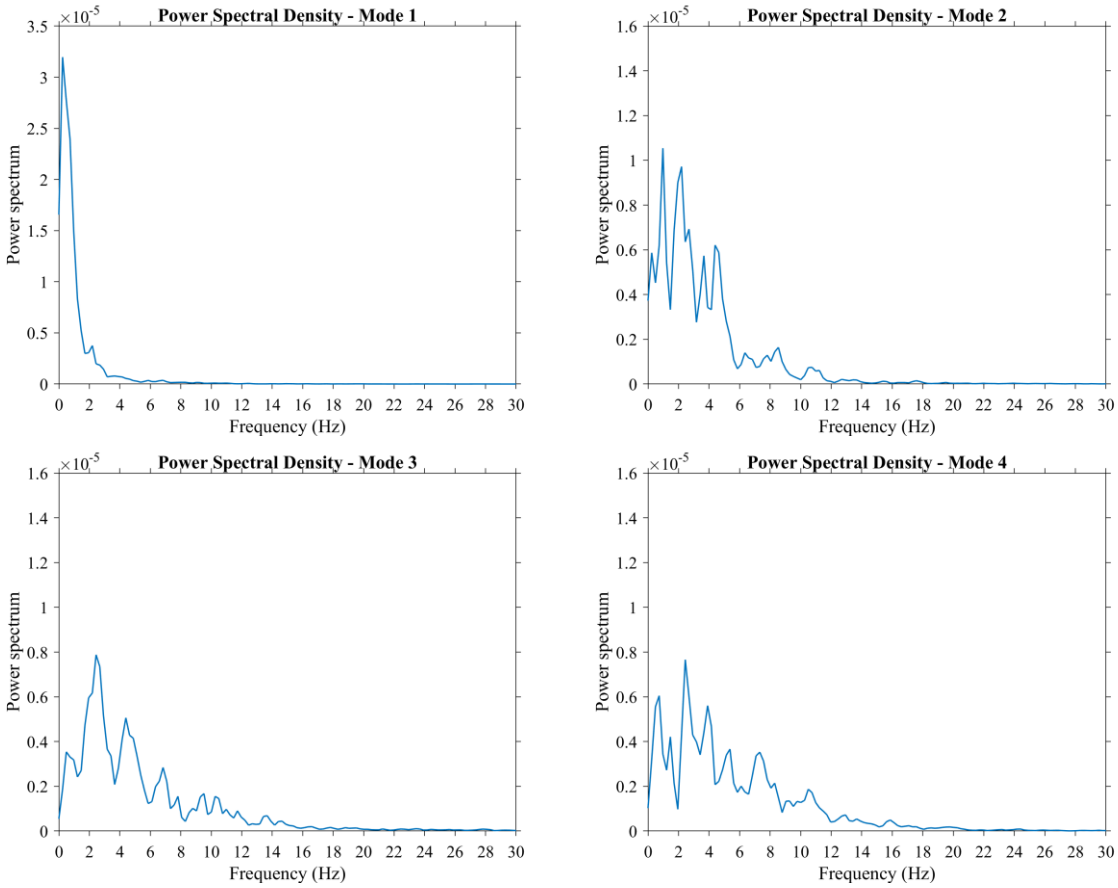

Figure A4.32 PSD of temporal coefficient of modes 1 to 4 (Bottom side)

A4.9 50-H-3.0m wind barrier (Bottom side)

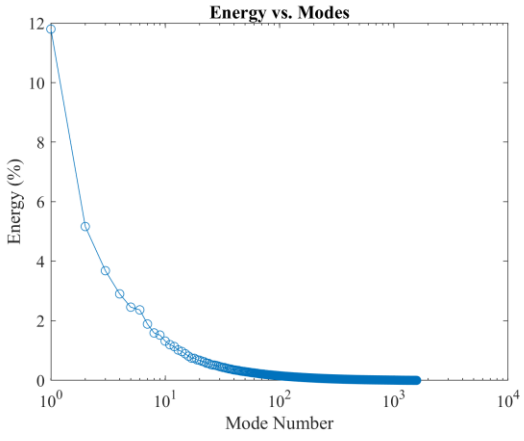

Figure A4.33 Energy of each mode

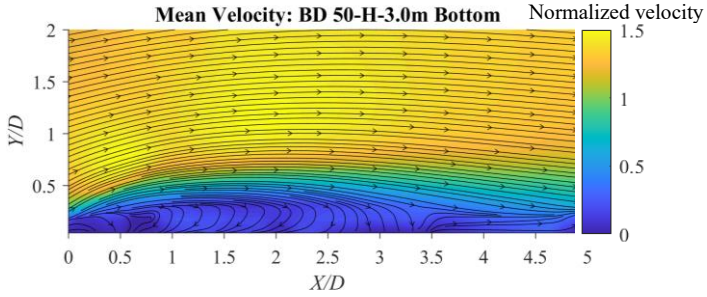

Figure A4.34 Mean wind velocity (Bottom side)

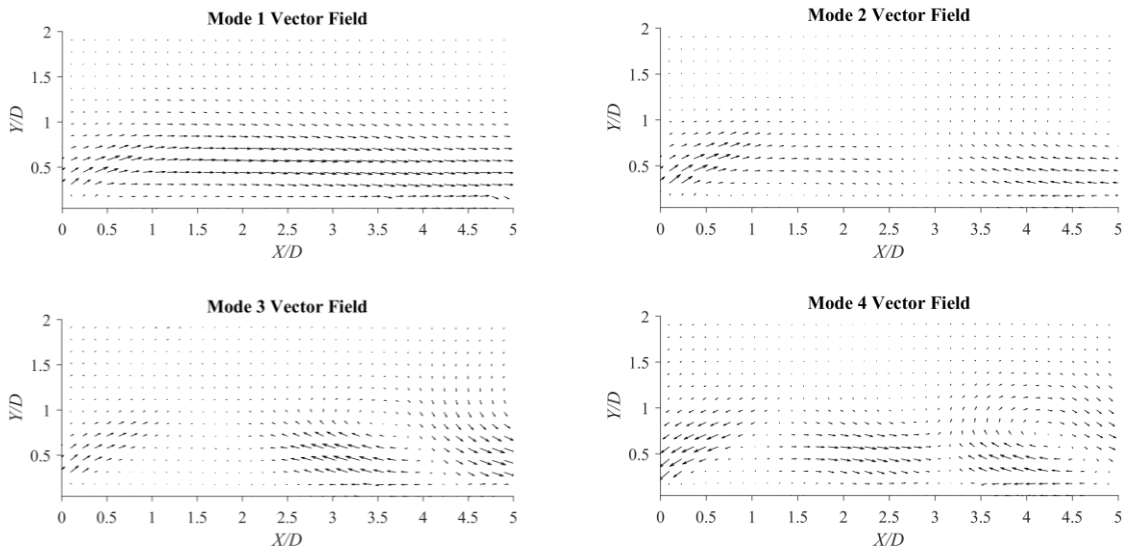

Figure A4.35 Vector field of modes 1 to 4 (Bottom side)

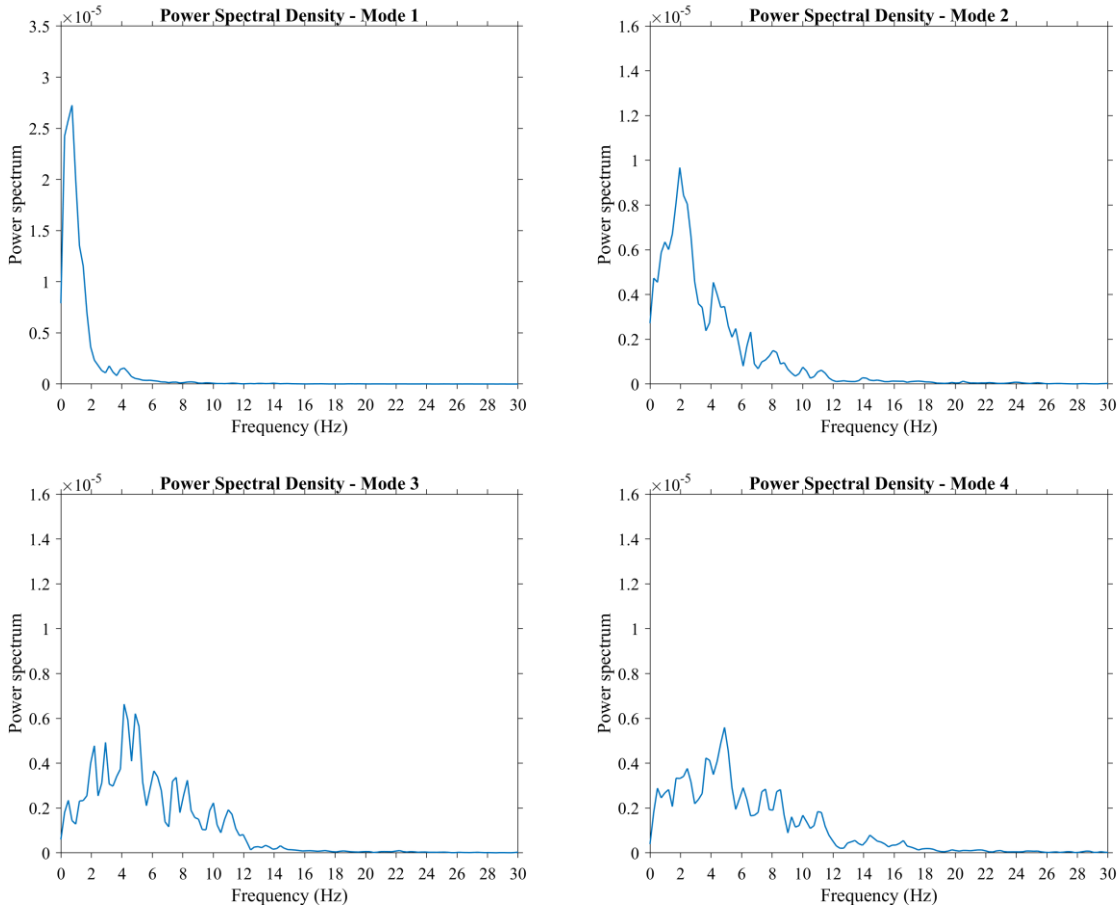

Figure A4.36 PSD of temporal coefficient of modes 1 to 4 (Bottom side)

A4.10 50-T wind barrier (Bottom side)

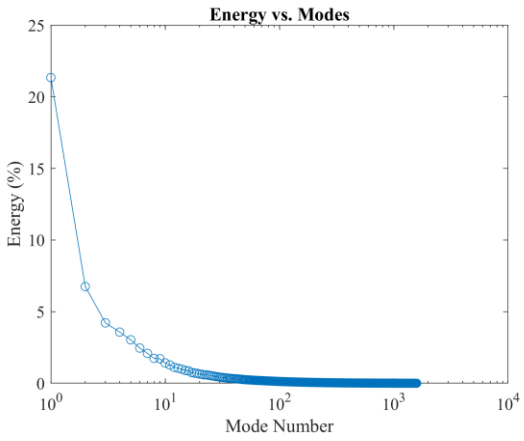

Figure A4.37 Energy of each mode

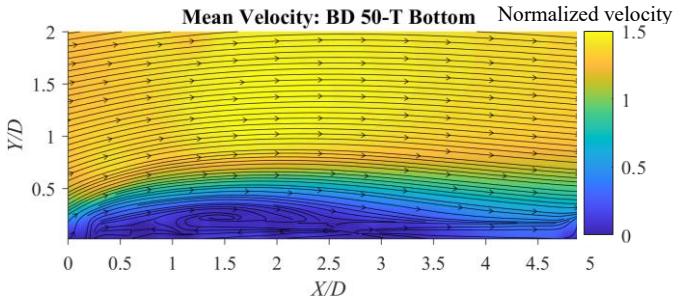

Figure A4.38 Mean wind velocity (Bottom side)

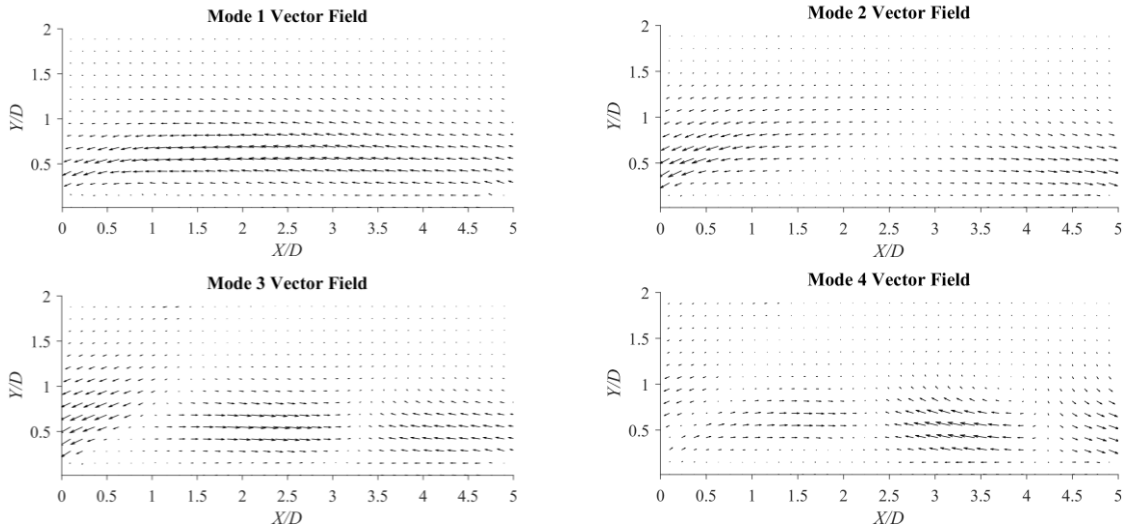

Figure A4.39 Vector field of modes 1 to 4 (Bottom side)

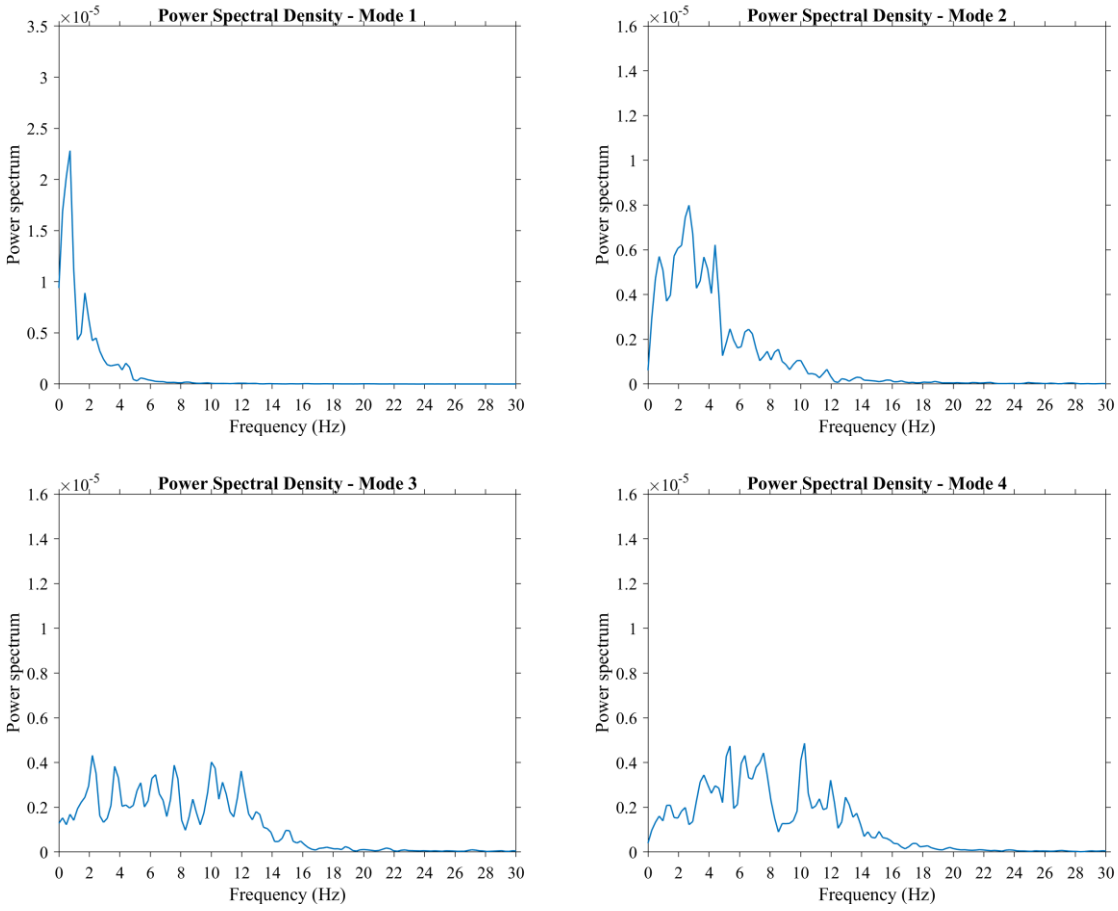

Figure A4.40 PSD of temporal coefficient of modes 1 to 4 (Bottom side)

A4.11 50-H-2.5m wind barrier (Bottom side)

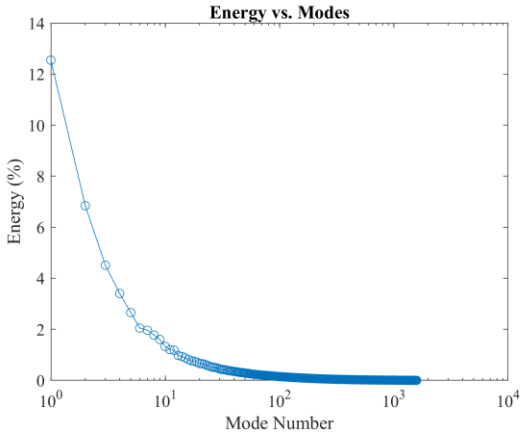

Figure A4.41 Energy of each mode

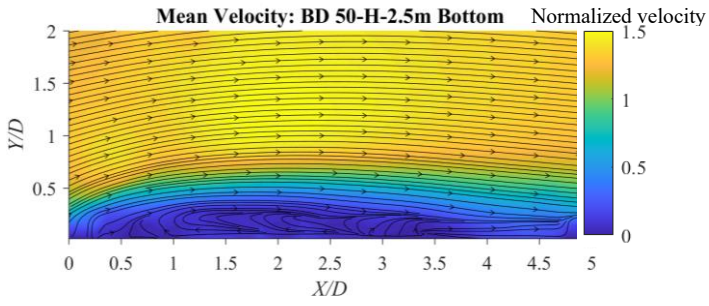

Figure A4.42 Mean wind velocity (Bottom side)

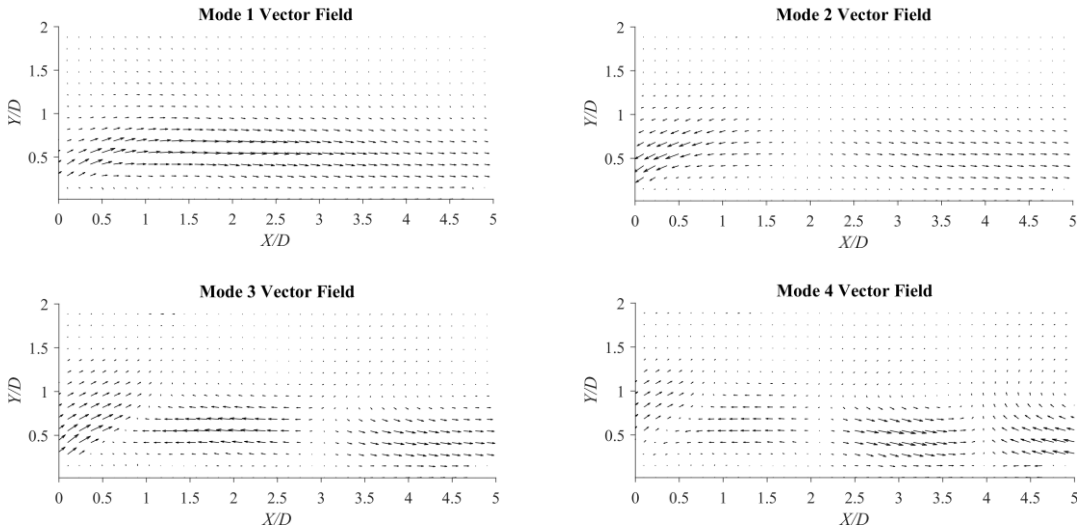

Figure A4.43 Vector field of modes 1 to 4 (Bottom side)

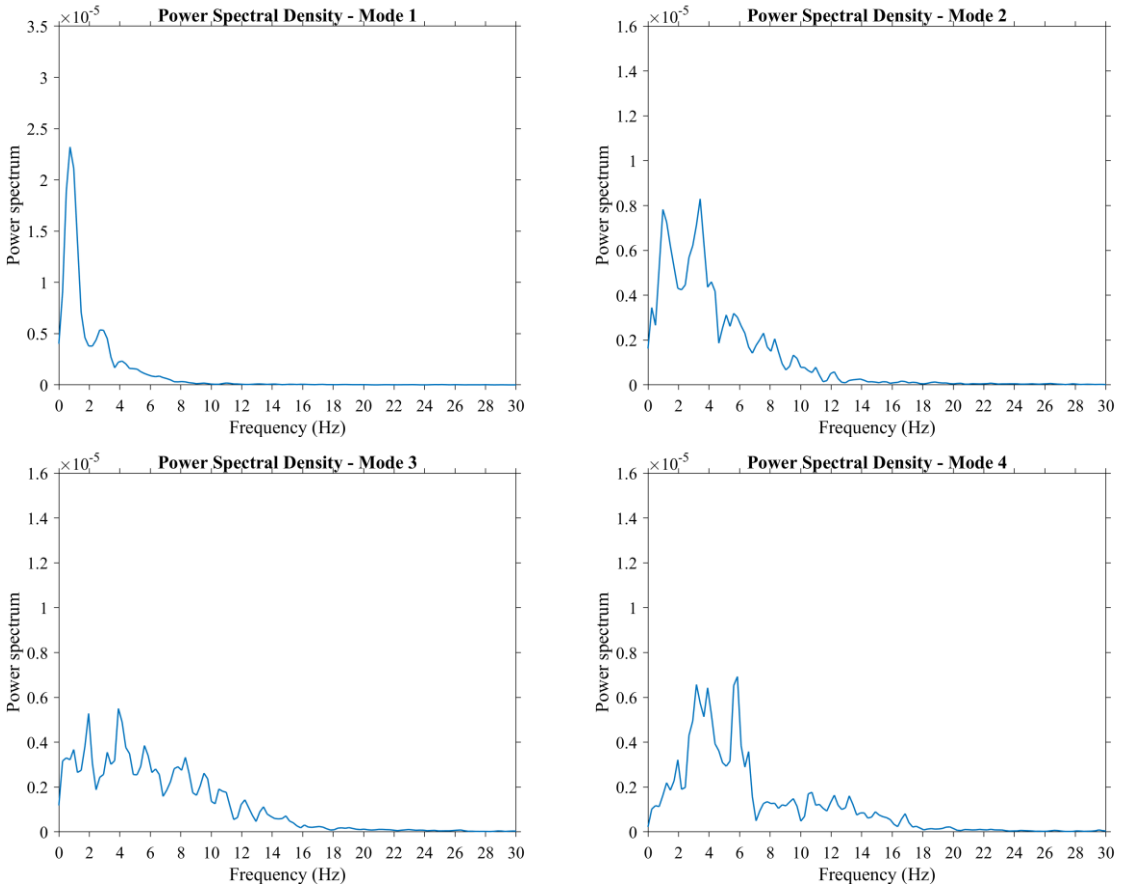

Figure A4.44 PSD of temporal coefficient of modes 1 to 4 (Bottom side)

A4.12 50-H-DS wind barrier (Bottom side)

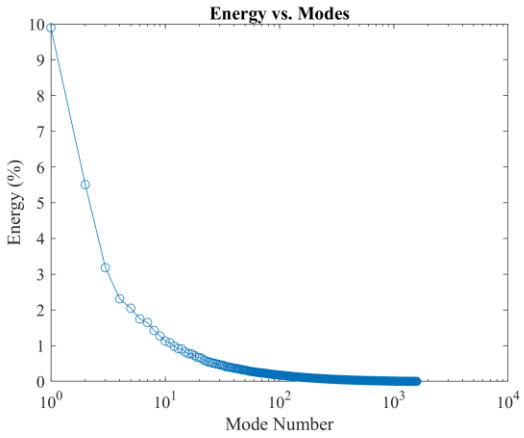

Figure A4.45 Energy of each mode

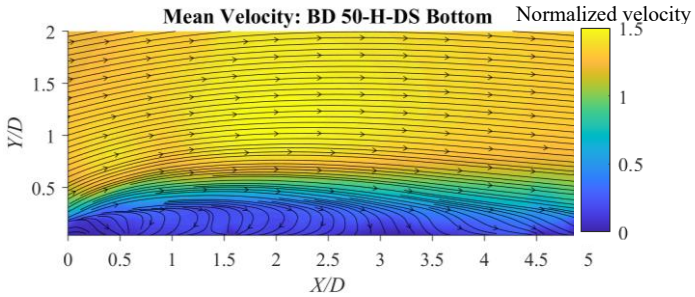

Figure A4.46 Mean wind velocity (Bottom side)

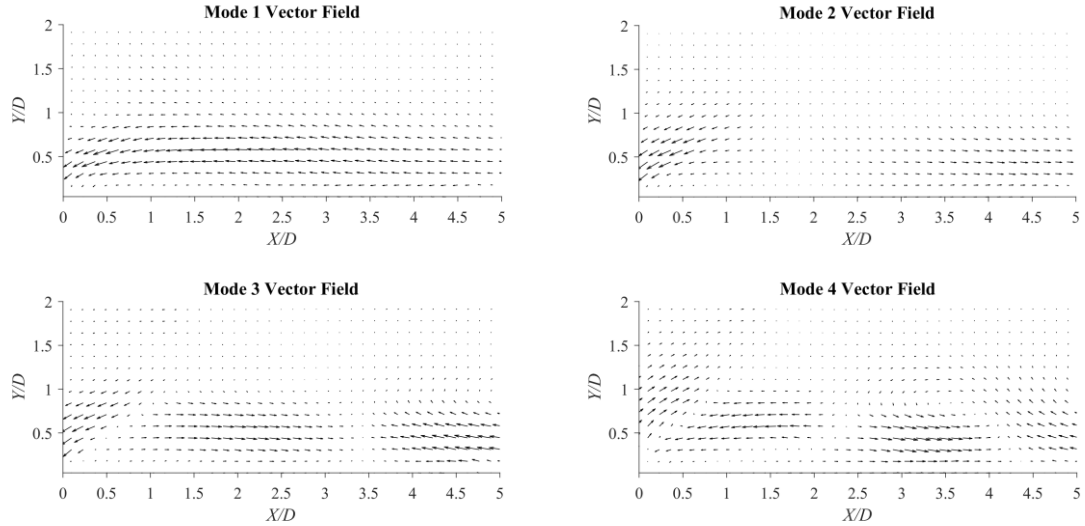

Figure A4.47 Vector field of modes 1 to 4 (Bottom side)

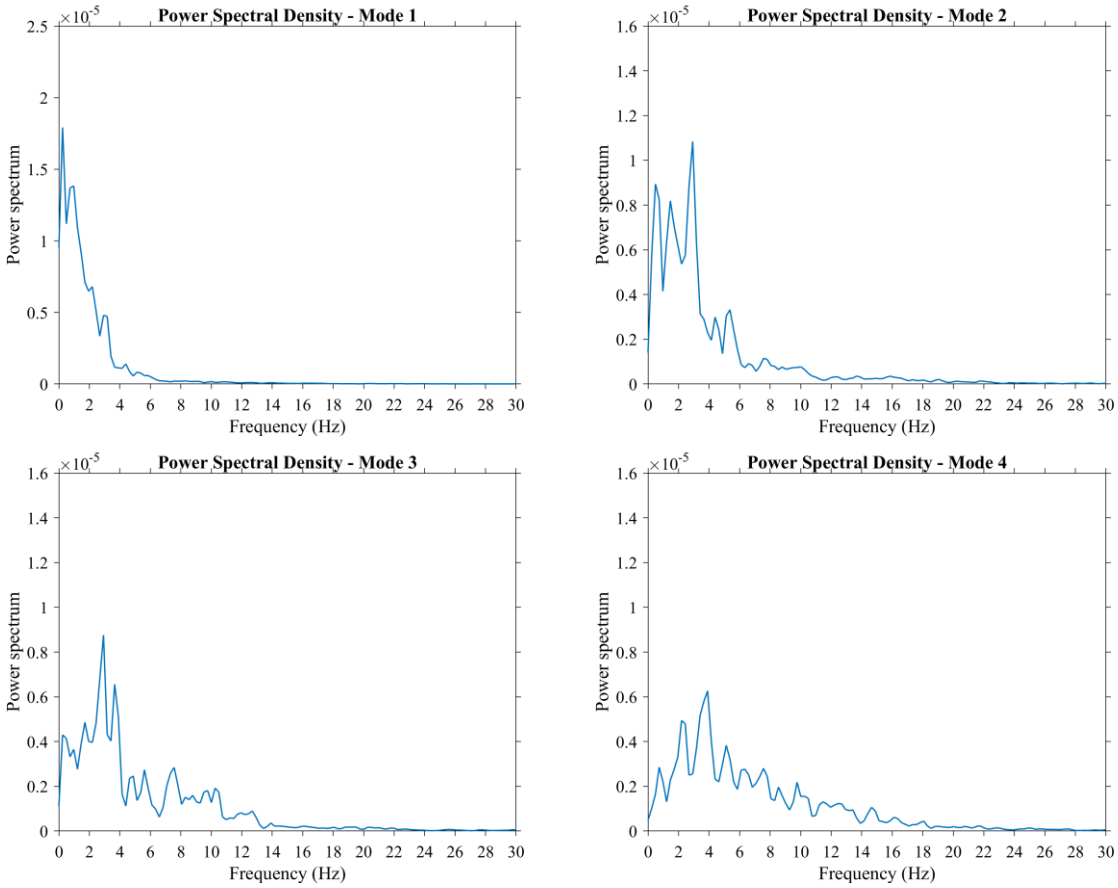

Figure A4.48 PSD of temporal coefficient of modes 1 to 4 (Bottom side)

A4.13 50-H+F wind barrier (Bottom side)

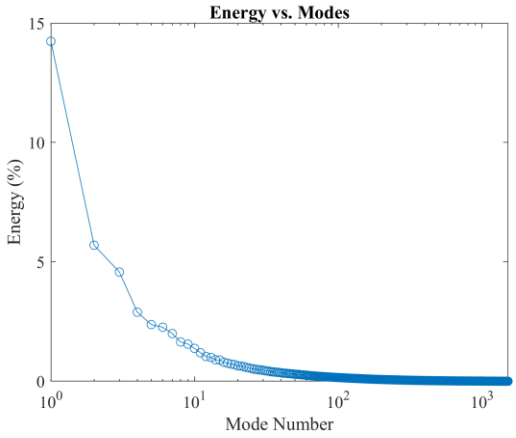

Figure A4.49 Energy of each mode

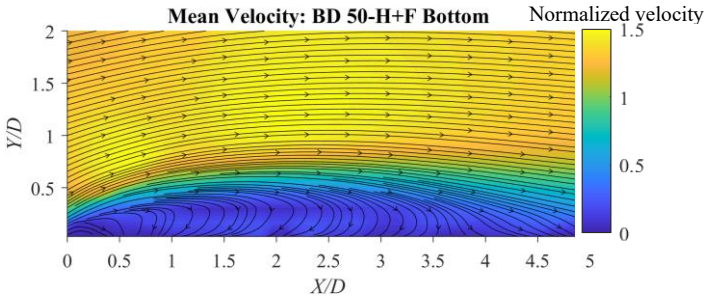

Figure A4.50 Mean wind velocity (Bottom side)

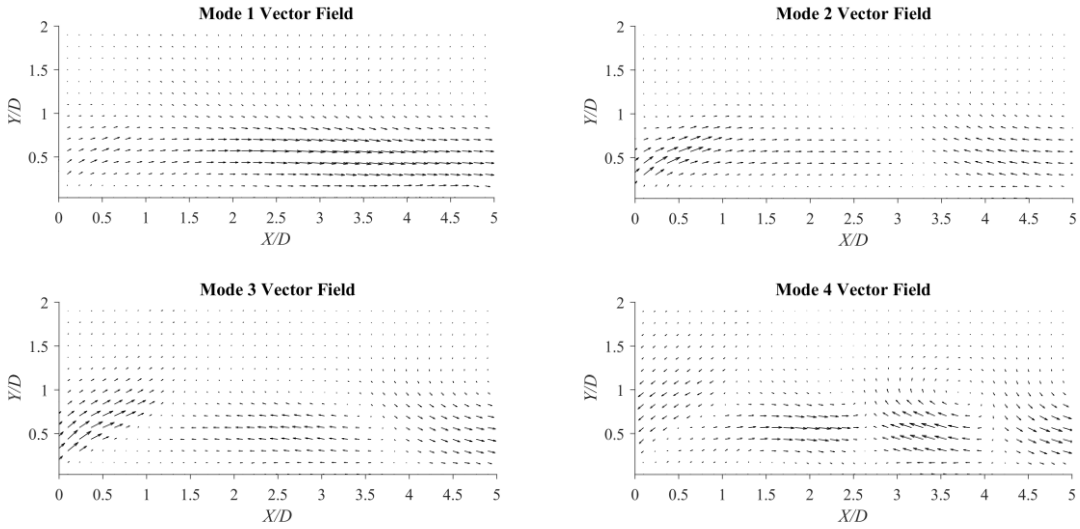

Figure A4.51 Vector field of modes 1 to 4 (Bottom side)

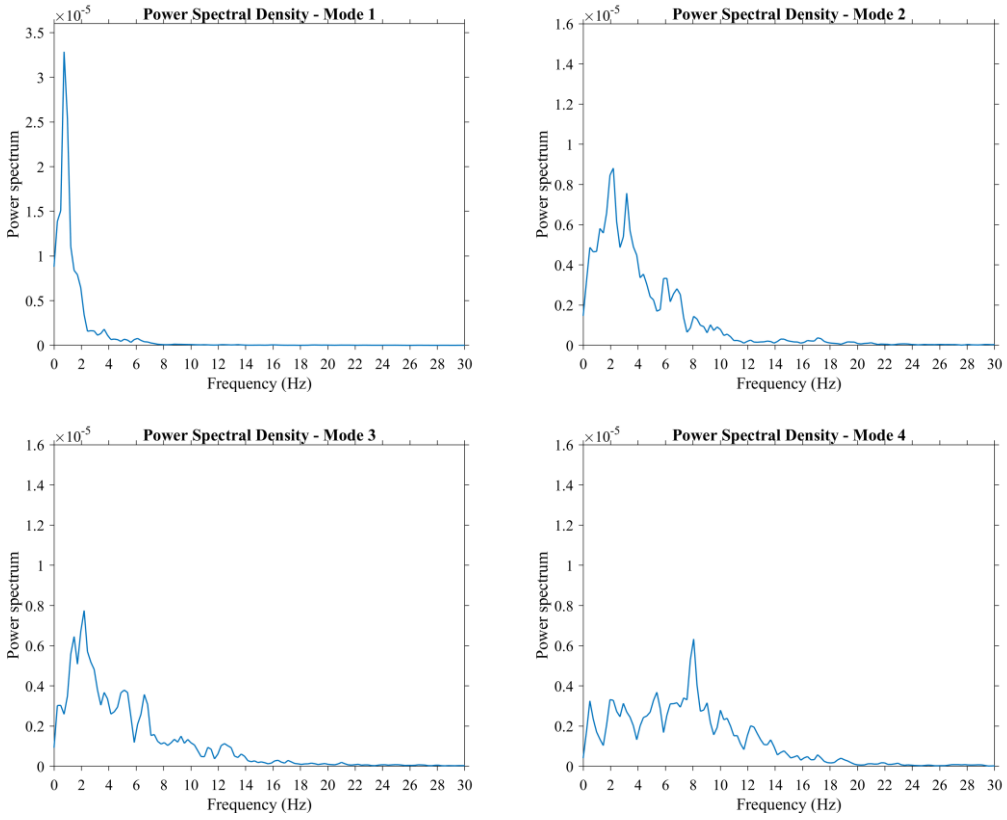

Figure A4.52 PSD of temporal coefficient of modes 1 to 4 (Bottom side)